

**ADVANCED IMAGING TECHNOLOGIES FOR COMBINED BIOMEDICAL
ULTRASOUND AND PHOTOACOUSTIC IMAGING**

by

Jaesok Yu, M.S.E.

Bachelor of Science in Electronic Engineering, Sogang University, South Korea, 2009

Master of Science in Electronic Engineering, Sogang University, South Korea, 2011

Submitted to the Graduate Faculty of

Swanson School of Engineering in partial fulfillment

of the requirements for the degree of

Doctor of Philosophy in Bioengineering

University of Pittsburgh

2018

UNIVERSITY OF PITTSBURGH
SWANSON SCHOOL OF ENGINEERING

This dissertation was presented

by

Jaesok Yu

It was defended on

January 11th, 2018

and approved by

Kang Kim, PhD
Dissertation Director

Associate Professor, Department of Medicine and Bioengineering

George D. Stetten, MD, PhD
Professor, Department of Bioengineering

Flordeliza Villanueva, MD
Professor, Department of Medicine

Sung Kwon Cho, PhD
Professor, Department of Mechanical Engineering & Materials Science

Mingfeng Bai, PhD
Assistant Professor, Vanderbilt University Institute of Imaging Science

Copyright © by Jaesok Yu

2018

ADVANCED IMAGING TECHNOLOGIES FOR COMBINED BIOMEDICAL ULTRASOUND AND PHOTOACOUSTIC IMAGING

Jaesok Yu, Ph.D.

University of Pittsburgh, 2018

Biomedical multimodal imaging approaches aim to improve the accuracy and effectiveness of current diagnosis by providing comprehensive disease information. With sharply increasing demands of functional imaging capability, several ultrasound-based state-of-the-art technologies have been developed to provide functional features of tissue, such as elastography to assess tissue mechanical property, thermal strain imaging to characterize tissue compositional property, and contrast-enhanced ultrasound imaging using microbubbles to assess blood perfusion, in addition to anatomical information provided by traditional grey-scale sonography. To further foster ultrasound imaging, in recent years photoacoustic imaging that detects optical contrast at relatively deep imaging depth has been developed. Photoacoustic imaging is capable providing non-invasive, real-time images of structural information with physiological features, such as oxygen saturation, representing hypoxia or the progression of cancer invasion and metastasis.

In this thesis, the combined ultrasound and photoacoustic imaging approach is innovatively engineered to provide both structural and functional information in high spatio-temporal resolution and contrast. First, the light illumination scheme in photoacoustic imaging is reinvented. With a conventional photoacoustic imaging system, approximately 30% energy of excited light would be lost due to reflection on the skin surface. A new light delivery scheme can collect and re-distribute reflected light to recover such energy loss, leading to improved signal amplitude. Second, optically-triggered phase-transition droplets as a highly efficient photoacoustic contrast agent are developed. Their vaporization and recondensation dynamics are investigated by an innovative

approach of concurrent optical and acoustical measurements for better understanding of the underlying processes, which will eventually guide the design of repeatable phase-transition droplets. We also developed a novel photoacoustic dye with high photostability that allows for long time monitoring. Finally, in addition to photoacoustic imaging, deconvolution-based super-resolution ultrasound imaging technology is developed to realize the spatial resolution beyond the acoustic diffraction limit, which enables to assess microvasculature with the sub-diffraction resolution, maintaining high temporal resolution.

We envision that the developed novel imaging technologies will provide a strong motivation and a key technical foundation to build an ultrasound and photoacoustic multimodal imaging system, which will be useful in pre-clinical and clinical research in the future, and eventually translated into clinics.

TABLE OF CONTENTS

1.0	INTRODUCTION	1
1.1	MULTIMODAL IMAGING TECHNIQUES	1
1.2	PHOTOACOUSTIC MOLECULAR IMAGING.....	4
1.3	SUPER-RESOLUTION ULTRASOUND IMAGING.....	8
1.4	LAYOUT OF THE THESIS	10
2.0	A LIGHT ILLUMINATION ENHANCEMENT DEVICE FOR PHOTOACOUSTIC IMAGING: IN VIVO ANIMAL STUDY	12
2.1	INTRODUCTION.....	13
2.2	MATERIALS AND METHODS	15
2.2.1	Photoacoustic imaging.....	15
2.2.2	The light catcher: a prototype manufacturing.....	15
2.2.3	Experiment setup of PA imaging	17
2.2.4	Photoacoustic contrast agents.....	19
2.2.5	Ex vivo experiment using chicken breast tissues	20
2.2.6	In vivo experiment using mouse tumor model.....	22
2.3	RESULTS AND DISCUSSIONS	23
2.3.1	Ex vivo study: Light delivery enhancement with the light catcher in chicken breast tissues.....	23
2.3.2	In vivo study: PA signal enhancement with the light catcher in mouse tumor model	26
2.4	CONCLUSION	29

2.5	ACKNOWLEDGEMENTS	29
3.0	VAPORIZATION AND RECONDENSATION DYNAMICS OF INDOCYANINE GREEN-LOADED PERFLUOROPENTANE DROPLETS IRRADIATED BY A SHORT PULSE LASER.....	30
3.1	INTRODUCTION.....	31
3.2	MATERIALS AND METHODS	32
3.2.1	Synthesis of PFC droplet.....	32
3.2.2	Experiment setup.....	34
3.3	RESULTS AND DISCUSSIONS	36
3.4	CONCLUSIONS	42
4.0	PHOTOSTABLE, HYDROPHILIC, AND NEAR INFRARED QUATERRYLENE-BASED DYES FOR PHOTOACOUSTIC IMAGING	44
4.1	INTRODUCTION.....	45
4.2	MATERIALS AND METHODS	47
4.2.1	Materials: Synthesis of QR-4PyC4 and QR-G2-COOH.....	47
4.2.2	Cell culture of MDA-MB-231	49
4.2.3	Cytotoxicity evaluation of QR-4PyC4.....	49
4.2.4	Cellular uptake study	50
4.2.5	Photoacoustic imaging and bright-field imaging.....	51
4.3	RESULTS AND DISCUSSIONS	52
4.3.1	Dendrimer characterization	52
4.3.2	Photostability evaluation.....	55
4.3.3	Cellular uptake and viability test.....	55

4.3.4	Photoacoustic imaging of MDA-MB-231 using QR-4PyC4, QR-G2-COOH, and ICG.....	57
4.4	CONCLUSION	60
4.5	ACKNOWLEDGEMENTS	61
5.0	SUPER-RESOLUTION ULTRASOUND IMAGING WITH HIGH TEMPORAL RESOLUTION: IN VIVO FEASIBILITY ON VASA VASORUM IN ATHEROSCLEROSIS RABBIT MODEL.....	62
5.1	INTRODUCTION.....	63
5.2	MATERIALS AND METHODS	66
5.2.1	Deconvolution-based super-resolution US imaging sequence	66
5.2.2	Spatio-Temporal-Interframe-Correlation (STIC) based data re-alignment algorithm.....	69
5.2.3	Rabbit atherosclerotic plaque model	71
5.2.4	Ultrasound imaging protocol.....	72
5.2.5	Histology and Immunofluorescence.....	73
5.3	RESULTS AND DISCUSSIONS.....	74
5.3.1	Deconvolution based super-resolution ultrasound imaging	74
5.3.2	In vivo feasibility of the developed super-resolution technique in imaging vasa vasorum on a rabbit femoral artery	77
5.4	CONCLUSION	80
5.5	ACKNOWLEDGEMENTS	81
6.0	CONCLUSIONS.....	82
	APPENDIX A	84

APPENDIX B	87
APPENDIX C	90
BIBLIOGRAPHY	101

LIST OF TABLES

Table 1. In vivo experiment results: The normalized and averaged PA signal amplitude (a.u.) in the ROI and enhancement ratio when using the light catcher.	28
Table 2. The photophysical properties of ICG, QR-G2-COOH and QR-4PyC4 at 10 μ M PBS solution.	54

LIST OF FIGURES

Figure 1. Cumulative percentage ratio of people diagnosed at each stage. (American cancer society, 2015)	2
Figure 2. Hybrid imaging system based on US imaging technologies and potential applications.	3
Figure 3. Scalability and tradeoff between imaging depth and spatial resolution in different configuration of PA imaging systems [34].....	6
Figure 4. The developed high-frequency ultrasound transducer integrated with the light catcher for PA imaging. (a, b) 3D drawing of the light catcher prototype. All parts were fabricated using 3D printing technology. (a,d) The handheld style housing was made for freehand scanning. (b,c,e) The detailed configurations of the ultrasound transducer and bifurcated optical fiber bundle integrated with the light reflecting mirrors. The angle between the transducer and the optical fiber is 30°. The concave shape light catcher is 12.7 mm in height and 25.4 mm in diameter. The light catcher inner surface was coated with silver. (f) For experimental evaluation of the device under the same geometrical setups of the optical fiber and the ultrasound transducer, two types of insertion with and without the light reflecting mirror were built. UT: Ultrasound transducer; w/ LC: with the light catcher; w/o LC: without the light catcher	16
Figure 5 (a) Experimental setups for ex vivo tissue and in vivo animal study. A commercial research ultrasound scanner was synchronized with a tunable laser system. A short laser pulse of 5 ns long was delivered through a bifurcated optical fiber attached to both sides of the US transducer. The concave reflecting mirror of the light catcher was placed on the target covered with ultrasound gel. (b) Laser fluence was measured at different	

depths (5, 10, and 15 mm) in chicken breast tissues (thickness of each tissue slab: 5 mm) at 689 and 800 nm (c) PA signal was measured from a polyethylene tube (Inner diameter: 580 μm , Outer diameter: 965 μm) filled with a contrast agent that was placed between chicken breast tissues of varying thickness. (d) For in vivo animal study, a contrast agent was locally injected into a subcutaneous tumor (Diameter: 1 cm) on the back of a mouse. 18

Figure 6. Normalized absorption spectrums of the verteporfin solution (a) and the ICG solution at 65 μM (b). In addition to its major absorption peak at the visible light at nearby 430 nm (Blue light), a distinct secondary absorption peak of verteporfin in the NIR at 800 nm. 20

Figure 7. Ex vivo experiment results: Measured laser energy at 689 nm (a) and 800 nm (b) at different depths in chicken breast tissues. Laser energy is measured at 5, 10, and 15 mm depth of chicken breast tissues with (white) and without (black) the light catcher. Each bar represents the mean of laser energy over 50 measurements with an error bar of the standard deviation. w/o LC: without the light catcher; w/ LC: with the light catcher. 24

Figure 8. Ex vivo experiment results: Short-axis PA images from a tube filled with (a) verteporfin taken at 689 nm and (b) ICG taken at 800 nm that was embedded in chicken breast tissue at depth of 15 mm. The left panels are for the case without using the light catcher and the right panels are for the case when using the light catcher. White dotted circles represent a polyethylene tube. (c) PA signal was enhanced by 37.6% for verteporfin at 689 nm and by 32.5% for ICG at 800 nm. 25

Figure 9. In vivo experiment results: Normalized PA images with and without the light catcher. (a) PA image overlaid on ultrasound B-mode image with 40 dB log-compression. The

yellow dashed contour represents the tumor location of the mouse and the top layer of the tumor is skin with hair removed. The white dashed box (Height: 1.2 mm, Width: 2.0 mm) indicates the region of interest (ROI) where the photosensitizer is administered. (b) PA images of ROI when using (Lower row) and without using the light catcher (Upper row) for each mouse ($n = 8$) within a depth of 14.6-15.8 mm. All PA images are normalized by measured laser fluence and shown in same dynamic range. (c) Statistical analysis of in vivo study results (Table 1). Solid circles and triangles represent averaged PA signal amplitudes in ROI with and without the light catcher, respectively. The central line of the boxplot is median, the edges of the box are 25th and 75th percentiles, and two whiskers above and below of the box are the maximum and the minimum of measurements. 27

Figure 10. Schematic of the ICG-loaded PFP droplets (a); Confocal fluorescent microscopy image of a droplet (b) before vaporization (Left panel) and after vaporization (Right panel). 33

Figure 11. Experiment schematic. A high-speed optical microscopy apparatus equipped with a water immersion objective lens (60 \times) was combined with NIR laser for PA excitation. Short pulse laser of 5 ns duration tuned at 800 nm was illuminated onto the target through the objective lens. Acoustic signal from vaporization was captured by a single element focused ultrasound transducer. Green and red arrows represent the light paths of the excitation laser for vaporization and white light for brightfield imaging, respectively. Acoustic and optical systems were aligned on the focal plane of the sample and synchronized through a custom-made FPGA-based timing controller. T/R: Transmitter/Receiver, OSC: oscilloscope. 35

Figure 12. Selected frames of high-speed imaging at 5 million frames per second (a, d) and acoustic signal measurement (Red solid line in (c, f)) and theoretical estimation (Blue solid line in (c, f)) from shell dynamics of a large droplet (Diameter = 4.8 μm , (a-c)) and a small droplet (Diameter = 2.0 μm , (d-f)) with short pulse laser excitation. (5 ns duration, 800 nm wavelength). Laser was excited at 0 μs . Analytic pressure calculation was performed using Eq. 2 with radius-time curves (b, e) measured by high-speed optical imaging.. 37

Figure 13. Repeatability of vaporization-recondensation and stability of droplet. (a) Optical (top panels) and acoustical (bottom panels) observations over 6 laser excitations on the same droplet measuring 2.0 μm in diameter at baseline. The envelopes of PA pressure were measured from multiple ODV processes of the same single droplet and corresponding high-speed images of each vaporization are shown in the top panel. Far left and far right panels depict droplets initially and 1 hour later, respectively. (b) Optical recording of a larger droplet (7.7 μm baseline diameter) over 1 second, imaged at lower frame rate. The vaporized droplet continually expanded after vaporization, and then floated away at 1 second. 39

Figure 14. Laser-induced vaporization of various sized droplets at different ambient temperatures. The snapshots at three different time points of 0.2 μs before laser excitation (left column), 0.6 μs after laser excitation (center column) and 2 μs after laser excitation (right column) during vaporization-recondensation processes below the bulk boiling temperature (20°C, top two rows) of PFP and above boiling temperature (37°C, bottom two rows) are depicted. Note that a laser pulse of 5 ns-long was induced at time 0 s over the circled area in green as shown in the left column. The dotted white circle identifies the droplet of interest located at the center of laser beam. The relatively large droplet

(diameter of 7.9 μm) in a medium with temperature above the bulk boiling temperature of PFP did not recondense after vaporization. 40

Figure 15. Summary of observation and interpretation of experimental results. Each solid circle represents a measurement condition ($n = 3$, data binned with $\pm 0.5 \mu\text{m}$). Recondensation was observed in blue colored droplets, and not observed in red colored droplets. Note each circle was scaled to the initial droplet size. *These droplets grew continually into a large gas bubble at later time. A droplet can be placed in three different states: (1) Vaporized (gas) or superheated state (liquid, light-red region), (2) Quasi-superheated state (liquid, light-blue or light-purple region), (3) liquid state (light-green region). The solid curve represents the size-dependent estimated boiling points of droplets as a reference threshold for vaporization. The dotted curve indicates the initial size of the droplets at each given temperature that can reach to the size on the solid curve at the same temperature after vaporization. Therefore, the droplets below the dotted curve will likely recondense, while those above will likely not recondense after vaporization.... 41

Figure 16. (a) Chemical structure of QR-G2-COOH; (b) The precursor QR-4Py and the synthetic route of QR-4PyC4..... 48

Figure 17 Acoustic-resolution photoacoustic microscopy setup for cell study. UT: Single element focused ultrasound transducer ($f_0 = 30 \text{ MHz}$) 51

Figure 18 Optical characteristic and photoacoustic response of QR-4PyC4, QR-G2-COOH, and ICG dyes. (a) Absorption spectrums of QR-4PyC4 (blue solid line), QR-G2-COOH (black solid line), and ICG (red solid line) in PBS solution at 10 μM concentration. (b) Change of PA signal amplitude at 740 nm of QR-4PyC4 (blue solid line), QR-G2-COOH (black solid line), and ICG (red solid line) over 3,600 short-pulse laser

exposures. Each data point represents an average over 5 measurements and error-bars are shown every 60 points.	53
Figure 19. Fluorescence spectra of ICG, QR-G2-COOH and QR-4PyC4 at 10 μ M.....	54
Figure 20. Cellular uptake percentage of QR-4PyC4, G2-QR-COOH, and ICG dyes.....	56
Figure 21. Cell viability of QR-4PyC4 in MDA-MB-231 cells. Cell medium (Dye concentration at 0 μ M) was used as a negative control, non-toxic, and, Doxorubicin (DOX) was used as a positive control, toxic.	56
Figure 22. (a) Optical microscopy image (10x) and (b) Photoacoustic image of MDA-MB-231 cells with QR-4PyC4 dye overlaid on microscopy image. Cells are marked as green spots. PA signal intensity is directly proportional to cell confluence.	57
Figure 23. Photoacoustic image of MDA-MB-231 cells stained with QR-4PyC4, QR-G2-COOH, and ICG. Images in each column are subsequently acquired.....	58
Figure 24. Averaged PA signal amplitudes of MDA-MB-231 cells stained with QR-4PyC4, QR-G2-COOH, and ICG.....	59
Figure 25. Block diagram for signal processing of super-resolution ultrasound imaging. BF: Delay-and-sum beamformer; QD: Quadrature demodulator; CF: Eigen-based spatio-temporal clutter filter; ED: Envelope detector; DV: Deconvolution with the system PSF; Σ : Integrator with STIC data alignment based on estimated cardiac pulsation.	66
Figure 26. Conceptual demonstration of sub-wavelength localization using deconvolution on synthetic data. (a) PSF of imaging system. FWHM is assumed as 150 μ m. (b) The locations of the two neighboring targets. Two targets are positioned 70 μ m apart. (c) Synthetic signal received from two targets is shown in (b) using the imaging system with PSF shown in (a). Two targets cannot be separated in the image due to their distance	

is shorter than the spatial resolution of imaging system. (d) Deconvolution results of received signal shown in (c) using the system PSF shown in (a). Two targets are distinctly identified. (e) Synthetic signal received from two targets when noise is added is shown in (b) using the same imaging system. (f) Deconvolution results of (e), where two targets are clearly identified with minimal interference due to noise 68

Figure 27. Estimated cardiac pulsation by counting the numbers of flowing microbubbles (blue solid line). After applying low-pass-filtering, the frames with minimum value are chosen as reference frames for synchronization (red solid line) 70

Figure 28. Graphical diagram of STIC data acquisition. Sequentially acquired multiple datasets are synchronized to form single cardiac cycle event based on the cardiac pulsation estimated by the numbers of bubbles. 71

Figure 29. Experiment setup of rabbit imaging. Microbubbles were injected via ear vein access. A hockey stick linear array ultrasound transducer was used for imaging. Transducer holder is used to remove operator-dependent motion in this study 73

Figure 30. Comparison of several imaging modalities. (a) CadenceTR contrast enhanced imaging with microbubbles acquired by commercial ultrasound scanner (Sequoia 512, Siemens), (b) conventional B-mode imaging, (c) temporal MIP vascular imaging, (d) proposed super resolution imaging of ROI. Same raw data is used to reconstruct images (b-d). White rectangle represents balloon injured area that the plaque is expected to be developed. White arrow indicates the same vessel branch that shows correlation of images acquired by two different ultrasound scanners. 75

Figure 31. Spatial resolution of proposed imaging method. (a) One of the finest vessels is chosen (white solid line) in the ROI, (b) Spatial profile of selected vessel. FWHM is estimated by $41\text{ }\mu\text{m}$ ($<\lambda/5$).....	76
Figure 32. Repeatability of proposed method. (a) temporal MIP vascular network imaging using eigen-decomposition method. (b-d) Super-resolution images using sequentially acquired three datasets (2,000 frames per each image) from same region of interest..	77
Figure 33. B-mode image (a, d) and corresponding super-resolution perfusion image overlaid on the B-mode image at diastole (b, e) and systole state (c, f). Top panel images are acquired from the injured side and bottom panel images are acquired from the non-injured side. Significant plaques are shown in the B-mode image on the injured side. Yellow dotted line represents adventitia region and white arrows indicate vasa vasorum in the adventitia	78
Figure 34. Haematoxylin and eosin stained vessel on the injured side (a) and non-injured side (b). Thirty images acquired at $\times 40$ magnification are stitched to reconstruct overall image of the vessel for (a) and (b). Significant plaque development is found in injured side (a). Vasa vasorum on adventitia in selected region was stained by anti-von Willebrand factor. A large number of vasa vasorums are found in adventitia on the injured side (c), but a few vasa vasorums are found in adventitia on the non-injured side (d).....	79
Figure 35. Vaporization threshold temperature according to droplet diameter	87
Figure 36. Theoretical expansion ratio vs droplet diameter	89
Figure 37. Timing diagram for the laser system and the high-speed camera	90
Figure 38. Block diagram of the interface between FPGA, the high-speed camera, and the laser system.	92

Figure 39. Timing diagram of flash-lamp and Q-switch of the laser system	93
Figure 40. Scenarios for capture success and failure	94
Figure 41. Developed timing controller using FPGA board with add-on input/output circuit.....	96

PREFACE

This thesis is dedicated to

all my advisors,

all my colleagues,

all my friends,

and

Love, my family.

Thank you all for your unwavering support.

1.0 INTRODUCTION

1.1 MULTIMODAL IMAGING TECHNIQUES

Cancer is a leading cause of death worldwide that accounts for 8.2 million deaths in 2012 according to the recent published statistics by World Health Organization (WHO) in 2015 [1]. Successful therapeutic strategies to combat cancer require a thorough understanding of the structural, metabolic and functional properties of the disease. Therefore, gathering such multifaceted information via a multi-modal approach is highly sought after to improve staging, treating, and managing cancer as well as to increase the likelihood of early detection of cancer [2]. Figure 1 clearly shows the importance of early detection of cancer for significantly increased survival rate. The critical need of accurate characterization of cancer for early detection using multiple functional features of cancerous tissue has motivated extensive development of various biomedical imaging modalities. Ultrasound (US) imaging, magnetic resonance imaging (MRI), computed tomography (CT), positron emission tomography (PET), and single photon emission computed tomography (SPECT) are established stand-alone imaging modalities to screen or diagnose cancer in the clinic [3]. Some clinical imaging systems have been used with limitations such as safety issues such as ionizing radiation (CT) or use of nuclear medicine (PET/SPECT), or the relatively low temporal and spatial resolution and the financial burden placed on patients and healthcare system (MRI) [3].

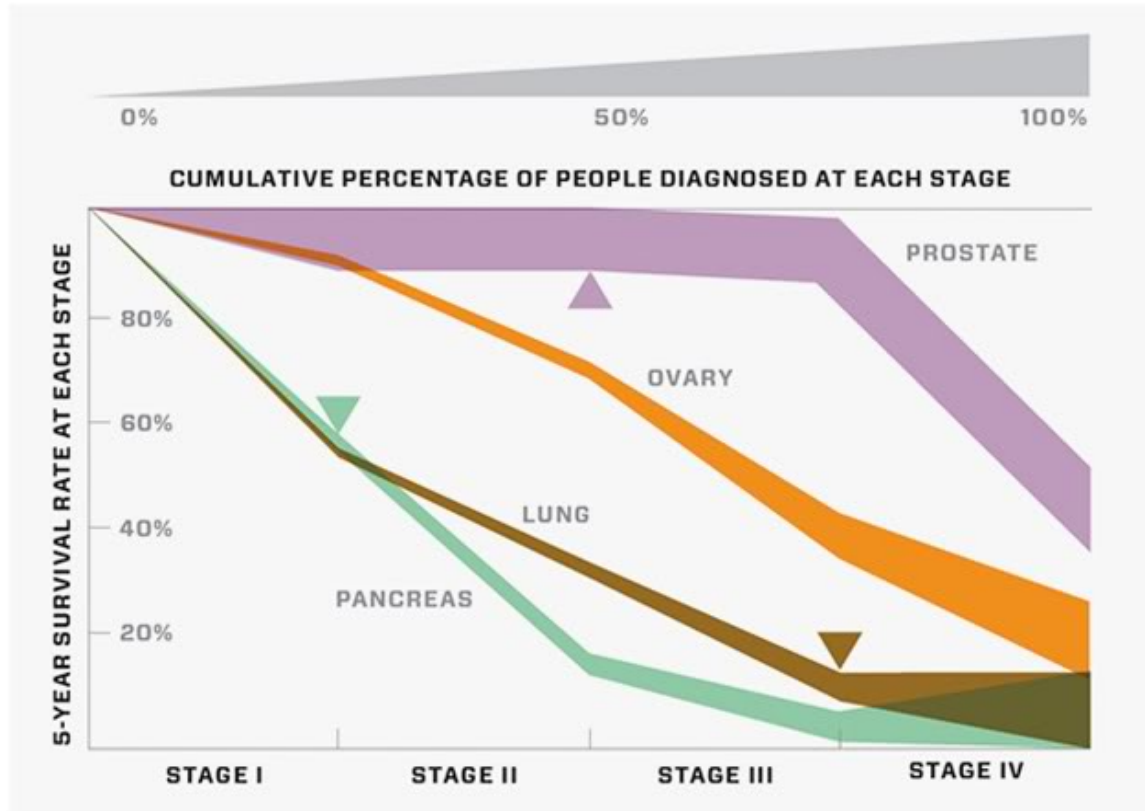


Figure 1. Cumulative percentage ratio of people diagnosed at each stage. (American cancer society, 2015)

Despite its inherent limitations with operator dependency and limited imaging view etc., US imaging is a widely-favored medical imaging technology of patient and physician for its safety (non-ionizing/non-invasive), ease-of-use, the anatomical/functional information provided in real-time, and affordability. Furthermore, accuracy of disease diagnosis can be improved by using multi-modes in a US imaging system, such as the Doppler technique, three-dimensional imaging, contrast-enhanced imaging with gas-filled microbubbles, thermal strain imaging, shear-wave elastography, and photoacoustic (PA) imaging [4]–[15]. Figure 2 illustrates the concept of hybrid US imaging system implemented with four independent but related imaging technologies for improved disease diagnosis that is capable of assessing structural and morphological information via conventional grayscale sonography, mechanical property via elasticity imaging (e.g., softness

of the tissue that correlated with the lipid rich necrotic core in atherosclerotic plaque [16]), compositional property via thermal strain imaging (e.g., fat component of fatty liver [17] or enriched lipid core in atherosclerotic plaque [18]), and biological characteristics via PA imaging of the lesion (e.g., optical contrast from dyed engineered tissue [19]).

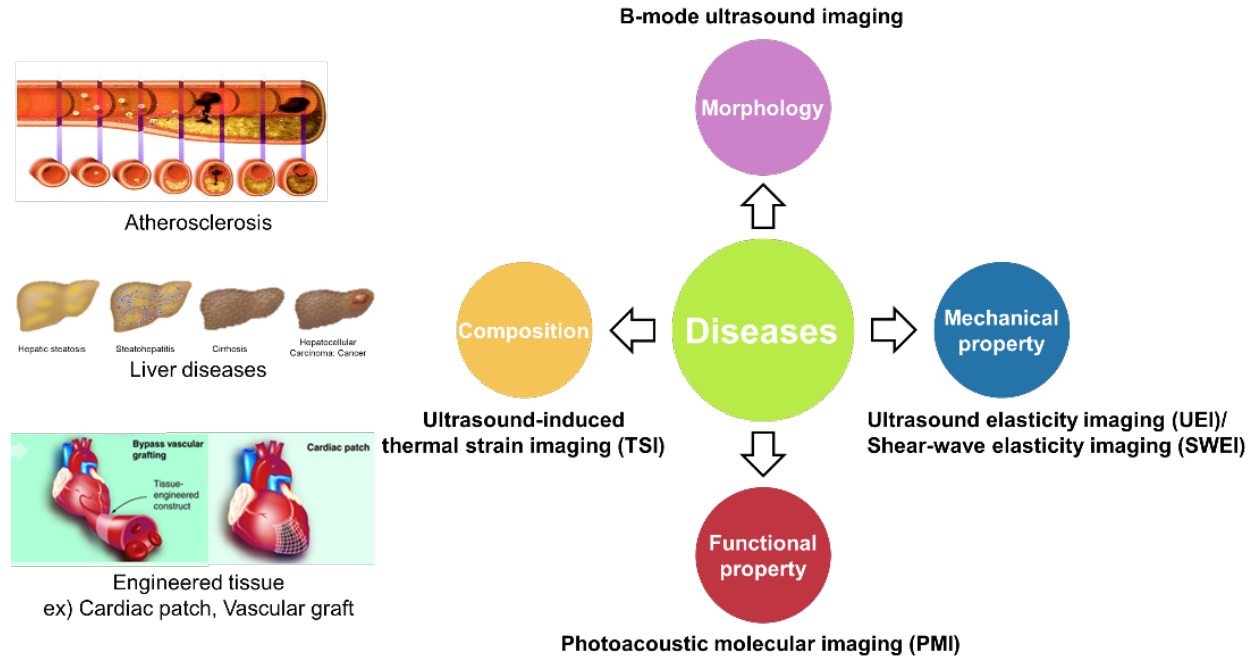


Figure 2. Hybrid imaging system based on US imaging technologies and potential applications.

Among these approaches, laser-induced ultrasonography, also known as photoacoustic (PA) imaging, has been extensively developed in the past decade to provide unique functional imaging based on strong optical contrast at ultrasonic imaging depth and spatial resolution [20]–[26]. Endogenous optical contrasts can provide valuable functional information regarding angiogenesis, hypoxia (deficiency in the amount of oxygen reaching the tissues), invasion and metastasis that are important indicators for cancer diagnosis [27]–[30]. Note that optical contrasts have only been provided by optical imaging techniques such as microscopes, fluorescence, and bioluminescence

at a depth of below a few millimeters or projected information with no depth information [26]. In pre-clinical studies, PA imaging has shown promising results in tumor characterization using multiple types of information, such as location, microvascular network, blood flow and oxygen saturation [21]–[26]. In addition, PA imaging has the potential to be patient-friendly as a safe, non-invasive and non-ionizing imaging modality [20]–[26]. The combination of US and PA imaging systems highlights the synergetic benefits of each modality by providing co-registered structural and functional information using both ultrasonic and optical contrast. The integrated information may lead to an improved diagnosis. In this thesis, each component of a US/PA multi-modal imaging system is innovatively engineered to overcome the limitations of the current configuration of US/PA imaging systems, such as limited imaging depth in PA imaging or limited spatial resolution defined by acoustic diffraction limit in US imaging. The developed imaging technique in this study for US/PA multi-modal imaging system can provide further clear (high signal-to-noise ratio (SNR)) structural (ultrasonic contrast) and functional (ultrasonic/optical contrast) information in high spatial resolution beyond the acoustic diffraction limit. The author envision that the developed novel imaging techniques may provide a strong motivation and a key technical foundation to build a US/PA multi-modal imaging system which will be used in pre-clinical and clinical research, and eventual translation in the future.

1.2 PHOTOACOUSTIC MOLECULAR IMAGING

Combining conventional ultrasound imaging system and nano-second laser technologies, PA imaging is an innovative imaging modality due to its uniqueness in providing optical contrast at a reasonable imaging depth, while traditional optical imaging techniques are limited with either

imaging depth of up to only a few millimeters or poor spatial resolution [31]. Note that endogenous optical contrast is concerned with functional information regarding angiogenesis, hypoxia and invasion that are important features in cancer characterization [27]–[30]. PA imaging is an emerging, non-invasive and non-ionizing medical imaging technology that combines light excitation and US detection. In PA imaging, an acoustic wave is generated from thermo-elastic expansion of tissue that is a mechanical relaxation process of the stress caused by tiny, transient temperature increase from tissue absorption of a nanoseconds short-pulse laser excitation. If the laser light is delivered properly with uniform illumination to a target area, a PA image could be generated with every laser shot. Therefore, the imaging frame rate of PA imaging can be determined by the laser pulse repetition frequency and considered as a real-time operation. In addition, PA imaging can provide strong endogenous and exogenous optical absorption contrasts at a reasonable imaging depth up to 3-4 centimeters in soft tissues [32]. Most notably, multi-spectral PA imaging can provide quantitative functional information such as variations in hemoglobin oxygen saturation (SO_2) in addition to morphological information of an endogenous optical contrast of tissue[21], [22], [24]. Thus, these features of PA imaging enable visualization of hypoxia and necrosis in tumors, thus providing valuable information for tumor staging and treatment planning [33].

Light delivery schemes are the most restrictive of PA imaging techniques. The limited imaging depth of optical imaging technology such as optical coherence tomography is mainly attributed to high scattering of light in the tissue, resulting in decreased coherence along the depth. Tissue-induced light is dispersed under the skin and leads to loss of directivity and decreased echo to detect photons on the outside of the skin for imaging. However, PA imaging is technology based on transforming light energy to other types of energy, such as ultrasound, heat, or photochemical

reactions. Accordingly, imaging capability of PA technology depends on how deep the photons penetrate the tissue, regardless of their coherence. Note that PA imaging preferably uses near-infrared (NIR) light for its transparency in soft tissue to maximize light penetration depth. PA imaging system can be configured differently for different applications with a wide range of imaging depth and spatial resolution, which are often determined by light delivery scheme as well as ultrasound sensor as receiver. Figure 3 shows such scalability of PA imaging technologies with different configurations [34]. To achieve deep imaging depth (to at least several centimeters with spatial resolution of organ level, indicated by PACT), diffused light and a clinical US array transducer are configured to PA imaging. In this setup, imaging depth can be extended up to 3-4 centimeters, but spatial resolution is limited to the acoustic diffraction limit ($\sim 3\text{-}500\text{ }\mu\text{m}$, depending on transducer frequency response) [32], [34].

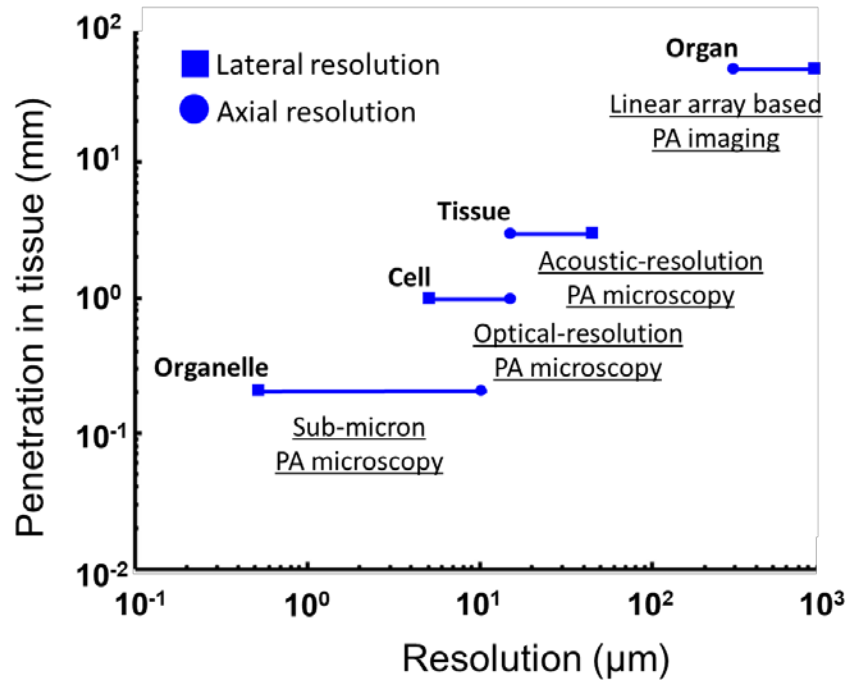


Figure 3. Scalability and tradeoff between imaging depth and spatial resolution in different configuration of PA imaging systems [34].

Under configuration of PA imaging system with a linear array transducer, light energy would be increased to maximize light penetration depth. However, the laser exposure dose for human is strictly regulated by the American National Standard Institute (ANSI) through Standard Z136.1, “Safe Use of Lasers” due to safety issues [35]. Therefore, developing a method to effectively deliver light to a target through tissues within ANSI safety guidelines and more efficient PA contrast agent are highly called for. It is known that a large portion of incident laser energy is lost due to reflection on the skin surface. Such light loss directly leads to a reduction of PA signal, thus limiting imaging depth. To overcome this shortcoming, development of a new light delivery scheme that restore such energy loss at the skin surface to enhance effective laser fluence at imaging target depth is required. In addition, due to restriction of laser energy for human use, a PA mechanism with high energy conversion efficiency from light to ultrasound will provide strong PA signal. Traditional PA contrast that use thermo-elastic expansion of the agent in response to a short-pulse laser is less effective mechanism compared to other PA contrast generation mechanisms such as photochemical, optical breakdown, and vaporization processes [36]–[39]. In recent years, optically-triggered phase transition or vaporization droplets have been introduced as a promising PA contrast agent [40], [41]. Short-pulse laser activated PFC-based droplets, especially when in a medium with a temperature below their boiling point, undergo phase changes of vaporization in response to pulsed-laser irradiation and generate a strong PA signal. Furthermore, the activated gaseous phase can be utilized as an US contrast agent. However, the underlying mechanism of the optically-triggered vaporization process is currently not fully understood due to the complexity and involvement of multiple parameters. To guide optimal design methodology, understanding the dynamics of laser-induced vaporization is necessary.

In addition to innovative PA mechanism to improve PA response, development of novel probes for PA imaging has been extensively studied [39], [40], [42]. There are some important features as an ideal efficient PA exogenous contrast agent; (1) a high absorption with low quantum yield at NIR region to increase penetration depth and signal-to-noise ratio (SNR), because most endogenous contrast such as blood [21], [43] and primary or metastatic melanoma [44] has strong absorption at the visible or infrared (IR) region [45], (2) high photostability which is necessary for a consistent long-term monitoring of biological activity progress under physiological environment *in vivo* [46], [47] and (3) high intracellular uptake or binding affinity, which determines functional or molecular selectivity. Most traditional organic PA contrast agents suffer from photobleaching or low cellular uptake [48], [49]. In addition, low toxicity is an absolute prerequisite condition for practical usefulness just like for any other *in vivo* molecular imaging modality. For example, quantum dots (QD) has been studied as highly resisting to photobleaching with great PA contrast agent [50], but its toxicity prevents QD from being widely spread for *in vivo* imaging study. Therefore, development of photo-stable, but non-toxic PA contrast agents is demanded for future translation.

1.3 SUPER-RESOLUTION ULTRASOUND IMAGING

Super-resolution ultrasound imaging technique, an innovative approach to break the acoustic diffraction limit for unprecedented high-spatial resolution, has promising potential for *in vivo* imaging of microvasculature such as brain vasculature or vasa vasorum that would have not been explored by using conventional ultrasound imaging technologies, which are inherently limited by the acoustic diffraction limit of clinical ultrasound scanner [51], [52]. In addition, this

technique can be easily applied for a broader impact for many other clinically important applications which are associated with abnormal microvasculature development or vascular degeneration/regeneration such as tumor angiogenesis indicating the likelihood of invasion and metastasis in cancer and kidney microvascular rarefaction from acute kidney injury [53]. Super-resolution ultrasound imaging was inspired by the photoactivated localization microscopy (PALM) that awarded the 2014 Nobel Prize in Chemistry [54], [55]. The procedure of the PALM is briefly described here. The key component of the PALM is specially designed photo-activatable dye that can be stochastically activated in response to the light input. Their activation for emission switching depends on an excitation laser applied at low power, so that the small population of the dyes are photoactivated from native emissive state. Some numbers of the activated individual dye without having any neighbor activated dyes in a distance within the optical diffraction limit can be distinguishable in an imaging plane. An individual activated dye is represented by the point spread function (PSF) of the imaging system. Note that the PSF describes the response of a wave-based imaging system to a point source and its size is limited by the diffraction limit. The point source, the photo-activatable dye, is assumed to be located at the apex of the PSF, thus the activated dye location can be exactly identified. Stochastically activated-dye location maps acquired over multiple times, would be integrated to form the super resolution image. In US imaging, circulating microbubbles and a spatiotemporal filtering were utilized to achieve stochastic responses instead of using the photo-activatable dyes [56].

While recently proposed super-resolution ultrasound imaging technology is promising for unprecedented high-spatial resolution beyond the acoustic diffraction limit, requiring a huge number of frames for a super-resolved image reconstruction limits its wide spreading. The most significant reason is attributed to the microbubbles localization technique using 2-dimensional

Gaussian function (point spread function of the imaging system) that discards data points when detected microbubbles are clumped together [57]. Therefore, an alternative approach for effective center localization technique is critically needed for practical usefulness of this technology. As an initial effort to further develop this technique for practical application with decreased data acquisition time, J. Yu et al suggested deconvolution technique for localization of microbubbles that drastically reduced the required number of frames, while maintaining high spatial resolution and suggested post-processing algorithm based on the temporal correlation of independently fluctuating echo from microbubbles to improve temporal resolution [58]–[60]. In addition to these initial effort, super-resolution ultrasound imaging technology would be further tailored for future clinical translation in this thesis.

1.4 LAYOUT OF THE THESIS

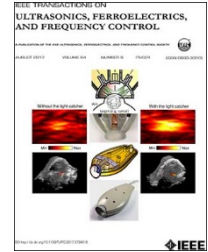
In this thesis, each technical component of US and PA imaging system will be innovatively engineered to provide significantly improved structural and functional information in high spatial resolution and at deep depth.

For further advanced PA imaging, Chapter 2 introduces a new light delivery scheme for enhanced PA imaging depth via compensation of light loss at the skin surface. The enhanced light delivery scheme can improve the signal-noise ratio of PA imaging system, leading to an increased imaging depth and improved image quality, which supports further translatability. Chapter 3 covers development of the optically-triggered phase-transition droplets and acoustical and optical observations of its vaporization and recondensation dynamics depending on ambient temperature and droplet size. These observation-based investigation leads to further understand the underlying

mechanism of the optical droplet vaporization and will eventually guide the design of repeatable phase-transition droplets as a high efficient PA imaging contrast agent. Chapter 4 presents novel near-infrared dyes with substantially high photostability for biomedical molecular photoacoustic imaging. Two strategically designed Quaterylene-structure dyes were synthesized and evaluated for its photostability, cell uptake efficiency, cell viability and capability of photoacoustic imaging using MDA-MB-231 cells. Chapter 5 explores novel signal processing and imaging sequence of US imaging to overcome the physical barrier of the spatial resolution of US imaging with high temporal resolution using novel deconvolution and spatio-temporal-interframe-correlation based acquisition. *In vivo* feasibility of the developed technologies is evaluated in rabbit atherosclerotic plaque model. Finally, Chapter 6 discusses the implications of these work on translational efforts motivated by these studies.

2.0 A LIGHT ILLUMINATION ENHANCEMENT DEVICE FOR PHOTOACOUSTIC IMAGING: *IN VIVO* ANIMAL STUDY

The work presented in this chapter was reprinted, with permission, from J. Yu, J. S. Schuman, J-K. Lee, S-G. Lee J. H. Chang, and K. Kim, “A light illumination enhancement device for photoacoustic imaging: in vivo animal study,” IEEE Transaction on Ultrasonics, Ferroelectrics, and Frequency Control, vol. 64, no. 8, pp. 1205–1211, Aug. 2017. © 2017 IEEE. This work featured on the front cover.



Photoacoustic (PA) imaging detects acoustic signals generated by thermal expansion of light excited tissue or contrast agents. PA signal amplitude and image quality directly depend on the light fluence at the target depth. With conventional PA imaging systems, approximately 30% energy of incident light at the near-infrared region would be lost due to reflection on the skin surface. Such light loss directly leads to a reduction of PA signal and image quality. A new light delivery scheme that collects and re-distributes reflected light energy was recently suggested, which is called the light catcher. In our previous study, proof-of-concept using a finite-element simulation model was shown and a laboratory built prototype of the light catcher was applied on tissue mimicking phantoms. In this study, we present an elaborate prototype of high-frequency PA probe with the light catcher fabricated using 3D printing technology, which is conformal to a subcutaneous tumor in mice. The *in vivo* usefulness of the developed prototype was evaluated in a mouse tumor model. Equipped with the light catcher, PA signal amplitude from the clinical photosensitizer injected into the mouse tumor was enhanced by 33.7%, which is approximately equivalent to the percent light loss due to reflection on the skin.

2.1 INTRODUCTION

Photoacoustic (PA) technology is a promising state-of-the-art medical imaging modality to quantitatively provide a real-time optical contrast at depth by using energy conversion from absorbed light energy to acoustic wave in tissue tissue [23]. In PA imaging, initial local PA pressure and PA image quality are directly affected by laser fluence. In the past years, various efforts have been made to further understand light propagation in the tissue and use them to improve light penetration in tissues with limited success. Kwon et al. suggested simulation model analyzing light propagation in the multiple layers of skin using mathematical models [61]. They concluded that adjusting incident beam power and diameter, physically compressing tissue, or using chemical agents can affect the light penetration depth. With such understanding, Yeo et al. developed a compression-controlled low-level laser probe to increase photon density in soft tissue with the negative mechanical compression control technique [62]. They successfully demonstrated a concentrated beam profile with enhanced laser photon density using their probe. Zhaohui et al. suggested a new light illumination scheme for deep tissue PA imaging and the proof-of-concept was shown through a finite-element simulation [63]. The proposed scheme was based on a fact that light energy is considerably lost by reflection at the skin surface depending on the incident angle. For example, experimental observation revealed that approximately 22-29% of light at 800 nm reflects off human skin with an incident angle of 20° [64]. Moreover, it is known the reflectance of 800 nm light increased by 13% (from 19 to 32%) as skin thickness increases from 0.43 to 1.60 mm [65]. Therefore, only approximately 70% of the near infrared (NIR) light is expected to penetrate into the tissues to excite targets in depth. For the safety of human use, the maximum amount of allowed NIR light fluence exposure in PA imaging should comply with the laser exposure safety guideline of American National Safety Institute (ANSI, Z136.1 – Safe Use of

Lasers). To overcome this shortcoming, a device called the light catcher was developed to restore energy loss at skin surface by collecting and redistributing reflected laser energy onto soft tissue and therefore enhancing the effective laser fluence. The proposed light catcher is a relatively simple concave shape light reflector integrated with an optical fiber bundle that is attached to an ultrasound probe. To collect and redistribute the light bounced off the skin surface, the inner surface of the cavity was coated with silver that highly reflects ($> 90\%$) light at the NIR region [66]. In addition to an increase in light fluence at the skin surface, a more uniform distribution of the laser energy at depth caused by random light reflection between the silver coating surface and skin surface was shown in the experiments using a tissue-mimicking phantom [63]. A conceptually similar technology was applied on a photoacoustic tomography system for brain imaging by Nie et al [67]. This device called the photon recycler that was designed to recycle scattered photon from the skin surface showed enhanced light transmittance *ex vivo* through a human skull. In our previous report by Yu et al., we manufactured an elaborate prototype light catcher for freehand scanning using 3D printing technology and integrated into a custom made high-frequency ultrasound imaging probe [68]. The developed system was tested *in vitro*. In this study, we further investigated and quantitatively evaluated *in vivo* the effectiveness of the developed hand-held light catcher that was designed for small animal tumor study.

2.2 MATERIALS AND METHODS

2.2.1 Photoacoustic imaging

Initial local photoacoustic (PA) pressure rise p_0 by thermal expansion after a short pulse laser excitation can be expressed by Eq.1 with assumptions that the absorbed optical energy is completely converted into heat energy and non-thermal relaxation such as fluorescence is enough small to be negligible [69].

$$p_0 = \Gamma \mu_a F \quad (1)$$

where Γ is the Grüneisen parameter associated with thermodynamic property of tissue, μ_a is an absorption coefficient, and F denotes laser energy fluence [67]. The Grüneisen parameter is given by $\Gamma = \alpha / (\kappa \rho C_p)$, where α is the isobaric volume thermal expansion coefficient, κ is the isothermal compressibility, ρ is density of the medium, and C_p is the specific heat capacity. Therefore, the initial local PA pressure is directly proportional to laser fluence. Given input power of the laser, the light catcher is designed to maximize the laser delivery at depth for higher PA signal amplitude and therefore increased imaging depth.

2.2.2 The light catcher: a prototype manufacturing

A concave shape light catcher (Hollow hemisphere, Height: 12.7 mm, Diameter: 25.4 mm) designed for a typical mouse subcutaneous tumor model was drawn by 3D computer-aided design (CAD) software (Solidworks 2012, Dassault Systèmes SOLIDWORKS Corp, MA, USA). Figure

4 illustrates 3D CAD drawing of the light catcher and the prototype of the light catcher in different views.

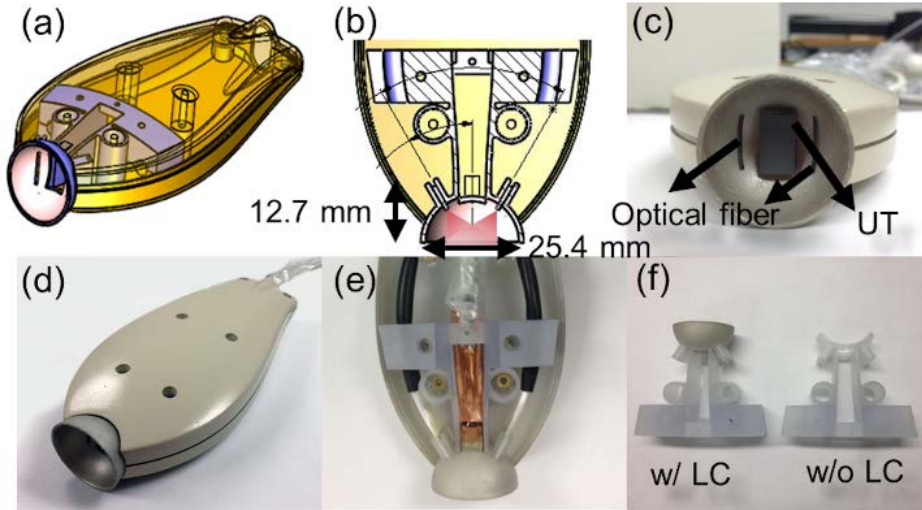


Figure 4. The developed high-frequency ultrasound transducer integrated with the light catcher for PA imaging. (a, b) 3D drawing of the light catcher prototype. All parts were fabricated using 3D printing technology. (a,d) The handheld style housing was made for freehand scanning. (b,c,e) The detailed configurations of the ultrasound transducer and bifurcated optical fiber bundle integrated with the light reflecting mirrors. The angle between the transducer and the optical fiber is 30° . The concave shape light catcher is 12.7 mm in height and 25.4 mm in diameter. The light catcher inner surface was coated with silver. (f) For experimental evaluation of the device under the same geometrical setups of the optical fiber and the ultrasound transducer, two types of insertion with and without the light reflecting mirror were built. UT: Ultrasound transducer; w/ LC: with the light catcher; w/o LC: without the light catcher

All parts shown in Figures 4(c)-(e) were produced by a stereolithography 3D-layering printer (Viper SLA system, 3D systems, Rock Hill, SC, USA) using water-resistant resin materials of high dimensional stability (Somos WaterShed XC11122, DSM, Heerlen, Netherlands). Silver was chosen as a coating material that is highly reflective ($> 95\%$) in the NIR range. The silver coating process was performed at room temperature due to relative low glass transition temperature (T_g , $39-46^\circ\text{C}$) of the 3D-printing material. A pair of custom-made optical fiber bundles (NA: 0.55, Core diameter: $50\ \mu\text{m}$, Fiber bundle width: 1.3 cm, Fiberoptic Systems Inc, Simi Valley, CA, USA) was integrated through two slits made in the concave reflecting mirror as shown in Figure 4(c). The incident angle of each laser beam was designed to be 30° from the major axis of an ultrasound

transducer to maximize the overlap area of two beams at the equator of the cavity. Approximate beam size at the equator of the light catcher (opening) is 2 cm x 1.3 cm. Multiple random reflections between the light catcher inner surface and the skin surface are expected that might result in more uniform light distribution in tissue. To keep the geometrical setups of the optical fiber and the ultrasound transducer unchanged between experiments, a duplicate light catcher insertion without a concave reflecting mirror was fabricated as shown in Figure 4(f).

2.2.3 Experiment setup of PA imaging

Figure 5 illustrates that the PA imaging system consists of a commercial clinical ultrasound scanner equipped with research package (SonixTouch, Analogic corporations, Peabody, MA, USA) to collect raw PA radio frequency (RF) data and an optical parametric oscillator tunable laser pumped by Nd:YAG Q-switched laser (Vibrant HE532I, OPOTek, Carlsbad, CA, USA) as a PA excitation source, with time synchronization between them. The laser wavelength can be tuned within 680-950 nm range. The short laser pulse of 5 ns-long was delivered through the custom made bifurcated optical fiber bundles (Fiberoptic Systems Inc., Simi Valley, CA, USA) attached to both sides of an ultrasound transducer. The laser pulse fluence ($<10 \text{ mJ/cm}^2$ at 689 nm and $<15 \text{ mJ/cm}^2$ at 800 nm) was kept within ANSI safety limit. A custom built 128-element high-frequency linear array transducer centered at 15 MHz with the full-width-half-maximum bandwidth of 65% for small animal imaging with a footprint of 15 mm long and 10 mm wide (iBule photonics, Incheon, South Korea) was connected to the ultrasound imaging system. The ultrasound gel was centrifuged to remove air bubbles before it was carefully applied on the inner surfaces of the light catcher and the subcutaneous tumor. The light catcher then was deliberately placed from one side

of the tumor to avoid trapping bubbles. Any excessive gel was removed upon completion of positioning.

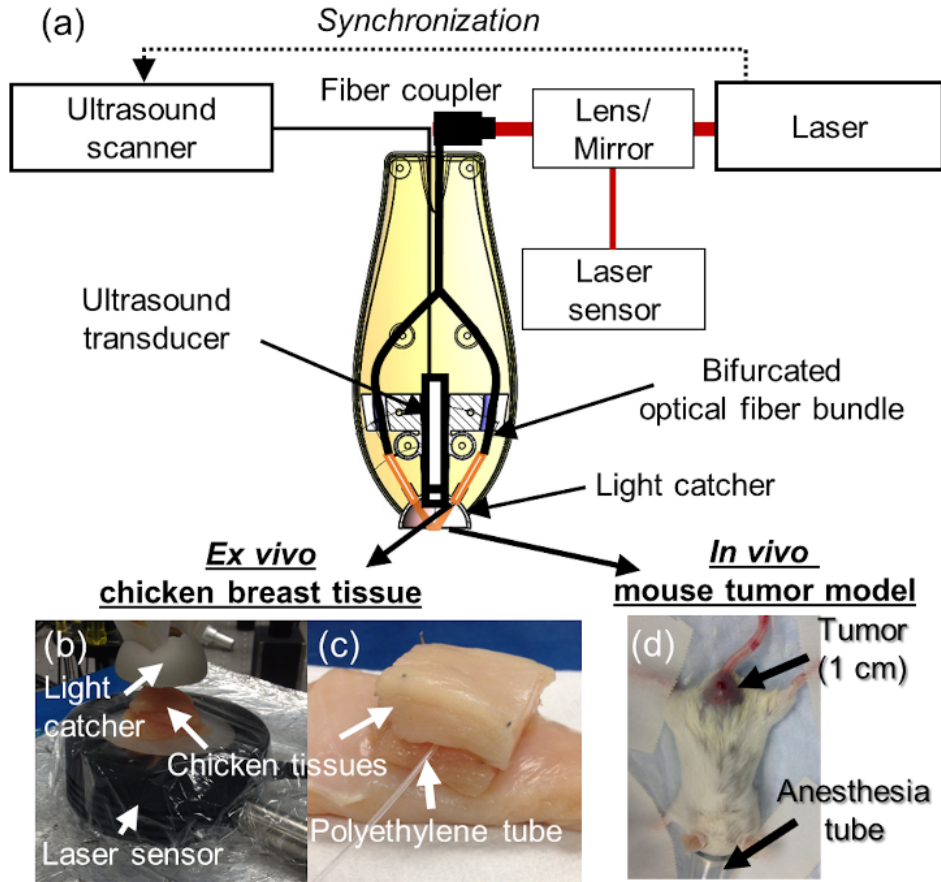


Figure 5 (a) Experimental setups for ex vivo tissue and *in vivo* animal study. A commercial research ultrasound scanner was synchronized with a tunable laser system. A short laser pulse of 5 ns long was delivered through a bifurcated optical fiber attached to both sides of the US transducer. The concave reflecting mirror of the light catcher was placed on the target covered with ultrasound gel. (b) Laser fluence was measured at different depths (5, 10, and 15 mm) in chicken breast tissues (thickness of each tissue slab: 5 mm) at 689 and 800 nm (c) PA signal was measured from a polyethylene tube (Inner diameter: 580 μm , Outer diameter: 965 μm) filled with a contrast agent that was placed between chicken breast tissues of varying thickness. (d) For *in vivo* animal study, a contrast agent was locally injected into a subcutaneous tumor (Diameter: 1 cm) on the back of a mouse.

For PA image reconstruction, the acquired raw PA RF data were processed off-line using delay-and-sum one-way dynamic receive beamforming. An envelope was extracted from the summed RF data applied with the Hilbert transform for PA image reconstruction. Ultrasound B-mode imaging was performed with 15 MHz transmit beam to focus at 10 mm depth. Acquired raw pulse-

echo RF data were processed using a conventional B-mode processing method; delay-and-sum dynamic receive beamforming, a band-pass filter (Bandwidth: 10.5-19.5 MHz) and, envelope detection using the Hilbert transform. The PA signal amplitudes were normalized to the measured averaged laser fluence over 50 laser pulses measured near the laser source output via using a laser sensor (YAG EnergyMax, J-50MB-YAG, Coherent Inc., Santa Clara, CA, USA).

2.2.4 Photoacoustic contrast agents

In this study, a clinical photosensitizer that has an absorption peak at 689 nm in NIR was employed as a PA imaging agent. The NIR region is the most preferred wavelength range for *in vivo* PA imaging due to relatively low background absorption by both water and blood. Visudyne®, also known as verteporfin (Liposomal verteporfin for injection, benzoporphyrin derivative monoacid ring A, BPD-MA; Valeant Pharmaceuticals North America LLC, Bridgewater, NJ, USA) is FDA approved photosensitizer that has been used in photodynamic therapy (PDT) for an anatomical treatment for vaso-occlusion of the arteriolarized neovessels. Even though the strongest absorption peak of the photosensitizer is nearby 430 nm (blue light), the absorption peak wavelength in the NIR, 689 nm, is mostly preferred for the PDT in the clinic as shown in Figure 6(a). The blue light attenuates quickly because of hemoglobin that has strong absorption in the same wavelength range. Instead, the sharp secondary peak at 689 nm, albeit relatively small absorption magnitude, can be used for *in vivo* PA imaging, as background absorption by hemoglobin, fibrotic tissue, or a skin chromophore such as melanin is relatively low at this wavelength. A solution of the photosensitizer was prepared with dose for human administration guidance written in the manufacturer's instruction. A vial of the photosensitizer of 15 mg was reconstituted with 7 mL of sterile water for injection resulting in the dark green colored

mother solution of 3.0 mM while the molar weight of the photosensitizer is 718.8 g/mol. The prepared mother solution was kept in dark storage to protect from ambient light. According to the clinical administration guideline, it would be diluted by using 5% dextrose to achieve a required dosage of the photosensitizer, 6 mg/m² of body surface area and the required total volume was 30 mL. Therefore, the clinical molar concentration of the photosensitizer should be kept under 0.7 mM. In addition, to test the light catcher efficiency at a different wavelength in NIR, indocyanine green (ICG) solution of 65 μ M with an absorption peak at 800 nm as shown in Figure 6(b) was used in *ex vivo* experiment [70]–[72]. The ICG solution was prepared by mixing the ICG powder of 50.4 μ g and distilled water of 1 mL. Note the molar weight of the ICG is 774.96 g/mol.

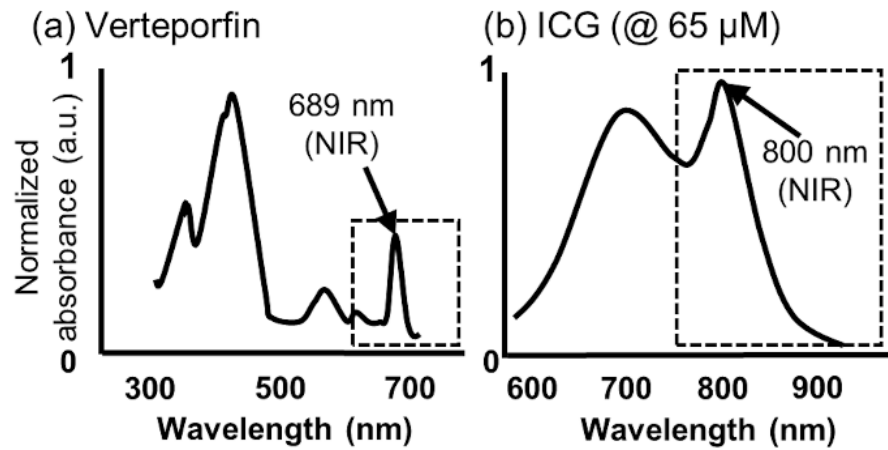


Figure 6. Normalized absorption spectrums of the verteporfin solution (a) and the ICG solution at 65 μ M (b). In addition to its major absorption peak at the visible light at nearby 430 nm (Blue light), a distinct secondary absorption peak of verteporfin in the NIR at 800 nm.

2.2.5 Ex vivo experiment using chicken breast tissues

Fat and blood removed chicken breast tissues were used for an *ex vivo* evaluation of the developed light catcher. To support the light fluence enhancement at the target depth when using the light catcher, laser pulse energy was measured at the same depth, maintaining all experimental conditions same. Laser energy was measured over 50 times by using the laser sensor covered with

thin clear plastic lab wrap (VWR, PA, USA), reducing variations from pulse-to-pulse laser energy fluctuation, at the bottom of the stacked chicken breast tissues with different thickness of 5, 10, and 15 mm, and compared with when the light catcher was not used as shown in Figure 5(b). Each chicken breast tissues were prepared with the size of about 20 mm (width) \times 20 mm (length) \times 5 mm (thickness). To compare corresponding PA signal enhancement due to increased light energy, a polyethylene tube (PE-50, Inner diameter: 580 μ m, Outer diameter: 965 μ m, Becton Dickinson, Sparks, MD, USA) filled with PA contrast agents was placed below three stacked chicken breast tissues of the total thickness of 15 mm. A separate large piece of chicken tissue of 20 mm thickness was placed at the bottom of the tube. Top and bottom chicken breast tissues were fixed by using pin nails. Centrifuged ultrasound gel was carefully applied to fill up the cavity of the light catcher before gently placing it onto the prepared chicken breast tissues. A thin layer of ultrasound gel also was applied between the layers of the tissue. To test the consistency of the performance in different NIR wavelengths, two different PA contrast agents were introduced at a time into the PE-50 tube embedded in the chicken tissue; verteporfin solution with an absorption peak at 689 nm and ICG solution with an absorption peak at 800 nm (Figure 6). PA images on short axis of the tube were acquired for both contrast agents using the laser pulse tuned at each absorption peak with and without the light catcher at the same depth. Mean and standard deviation of PA signal amplitude were calculated over tube area of each PA image. For each dye, PA images when using and without using the light catcher were shown in same dynamic range after being normalized to the peak PA signal amplitude when using the light catcher. The statistical significance was measured between mean values of paired PA images (with using the light catcher vs without using the light catcher) by using t-test.

2.2.6 *In vivo* experiment using mouse tumor model

EMT-6 breast cancer cells acquired from the American type culture collection (ATCC, Manassas, VA, USA) were cultured in Waymouth's MB 752/1 with L-glutamine culture medium (Gibco, Life Technologies, Grand Island, NY, USA) added with 15% fetal bovine serum albumin (FBS, Atlanta biological, GA, USA) and 2% penicillin-streptomycin (Lonza, Basel, Switzerland). Cells were cultured in the cell incubation t-flask chamber at 37°C with 5% CO₂ condition until reaching a number of cells $> 8 \times 10^6$. Cultured cells were withdrawn from incubated t-flask to a vial of 1×10^6 cells for each mouse. Each sample was washed 3 times and suspended in 0.2 mL hyclone hank's balanced salt solution (HBSS, Thermo Scientific, South Logan, UT, USA). Tumors were developed on 6-weeks old female BALB/c-albino mouse by subcutaneously injecting cells on her lower back. Tumor-bearing mice were taken care of until each tumor size reached up to 10 mm in diameter (Figure 5(d)). The prepared verteporfin solution of 50 μ L (3.0 mM) was locally administrated into the center of tumor of each anesthetized mouse using an injection needle of gauge 26. PA signal amplitudes from injected verteporfin were measured when using and without using the light catcher. For each animal, the paired PA images were normalized to the maximum PA signal intensity in the PA image when using the light catcher. All images are shown in the same normalized dynamic range. The total number of mice used in this study was 8 and significance of the measurements were determined by calculation of p-value using t-test statistical analysis. The *in vivo* animal study was conducted under an approved protocol of Institutional Animal Care and Use Committee (IACUC) of University of Pittsburgh.

2.3 RESULTS AND DISCUSSIONS

2.3.1 Ex vivo study: Light delivery enhancement with the light catcher in chicken breast tissues

Figure 7 compares laser energy at different depths in the chicken breast tissues between the cases when using and without using the light catcher. The white and black bars represent the mean value of measured laser energy with and without applying the light catcher, respectively, at 3 different depths of 5, 10, and 15 mm, with an error bar of the standard deviation over 50 measurements. Using the light catcher increases the laser energy by 27.9% (17.3 ± 1.1 mJ vs 12.3 ± 0.8 mJ, $p < 0.05$, when using the light catcher vs without using the light catcher for the rest of this paper) and 33.3% (26.4 ± 1.5 mJ vs 17.8 ± 1.0 mJ, $p < 0.05$) at 5 mm, 31.0% (11.7 ± 0.7 mJ vs 8.1 ± 0.5 mJ, $p < 0.05$) and 34.9% (17.4 ± 1.0 mJ vs 11.2 ± 0.7 mJ, $p < 0.05$) at 10 mm, and 30.4% (9.4 ± 0.6 mJ vs 6.3 ± 0.4 mJ, $p < 0.05$) and 34.4% (13.0 ± 1.0 mJ vs 8.5 ± 0.6 mJ, $p < 0.05$) at 15 mm for 689 nm (a) and 800 nm (b), respectively. Note that the measured laser energy without chicken breast (at depth 0 mm) are considered as same for both cases when using or without using the light catcher at each wavelength (36.3 ± 1.1 mJ vs 35.6 ± 0.9 mJ, $p < 0.05$ for 689 nm, 57.7 ± 1.5 mJ vs 57.3 ± 1.3 mJ, $p < 0.05$ for 800 nm). One of the limitations of this experiment is that laser pulse energy was measured instead of local laser fluence that directly affects initial local PA pressure because measuring local laser fluence could be erroneous without being able to know exact light propagation paths and beam profile. However, we believe that the increment ratio of total through-transmission of laser energy with the device would be very close to if not exactly same as the increment ratio of local laser fluence, while all experimental conditions were maintained the same.

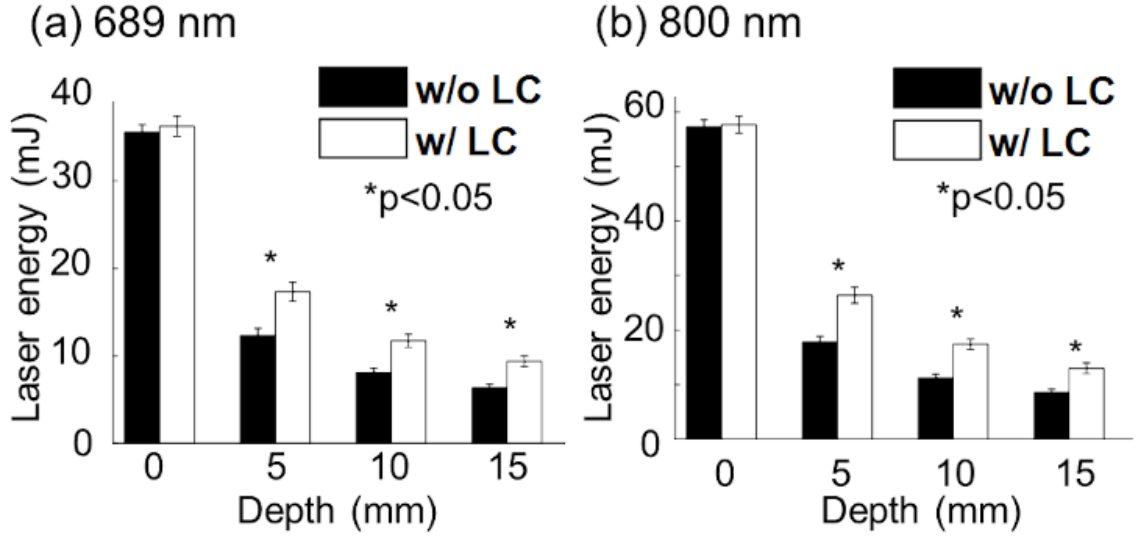


Figure 7. Ex vivo experiment results: Measured laser energy at 689 nm (a) and 800 nm (b) at different depths in chicken breast tissues. Laser energy is measured at 5, 10, and 15 mm depth of chicken breast tissues with (white) and without (black) the light catcher. Each bar represents the mean of laser energy over 50 measurements with an error bar of the standard deviation. w/o LC: without the light catcher; w/ LC: with the light catcher.

Figure 8 shows short-axis PA images from a tube filled with two different dyes embedded in chicken breast tissue at depth of 15 mm; verteporfin in (a) and ICG in (b). A white dotted circle represents the tube with inner diameter of 580 μm as a region of interest (ROI). PA signals were only detected on the top and bottom of the tube due to the linear array transducer's geometrical limited view [72], [73]. When using the light catcher, PA signal amplitudes over the tube area for both agents were significantly enhanced as shown in Figure 8(c); verteporfin at 689 nm: 37.6% enhancement, PA amplitudes of 39.9 ± 11.7 vs 24.9 ± 4.4 , and ICG at 800 nm: 32.5% enhancement, PA amplitudes of 70.2 ± 26.7 vs 47.4 ± 16.1 . A significant difference with $p < 0.05$ using t-test was shown for both cases. PA signal enhancement in two different wavelengths of 689 nm and 800 nm are in good agreement with laser fluence increase shown above and our previous *in silico* and *in vitro* results [63], [68]. This experiment result implies that PA signal would be amplified by increased laser fluence at depth when using the light catcher.

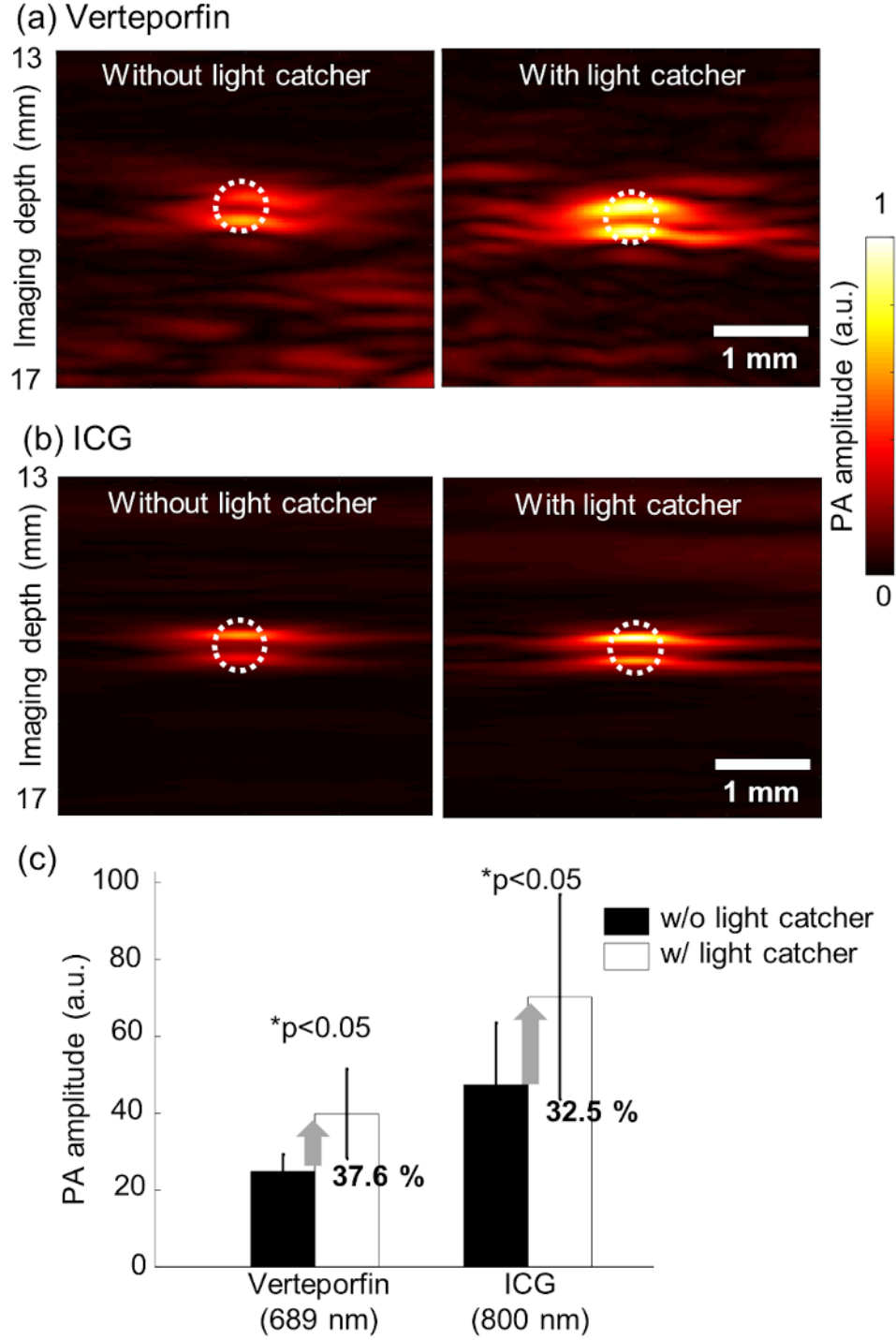


Figure 8. Ex vivo experiment results: Short-axis PA images from a tube filled with (a) verteporfin taken at 689 nm and (b) ICG taken at 800 nm that was embedded in chicken breast tissue at depth of 15 mm. The left panels are for the case without using the light catcher and the right panels are for the case when using the light catcher. White dotted circles represent a polyethylene tube. (c) PA signal was enhanced by 37.6% for verteporfin at 689 nm and by 32.5% for ICG at 800 nm.

2.3.2 *In vivo* study: PA signal enhancement with the light catcher in mouse tumor model

A representative PA image overlaid on ultrasound B-mode image is shown in Figure 9(a). Ultrasound B-mode image was log-compressed with 40 dB dynamic range. The yellow dashed contour draws the tumor of the mouse, and the top layer of the tumor is hair-removed skin. The white dashed box (Height: 1.2 mm, Width: 2.0 mm) in the image indicates the injection site within the tumor volume. The bright color at the center of the region of interest (ROI) indicates PA signal from the injected photosensitizer. The PA signals with much lower amplitudes found in the periphery of ROI are believed to be from the vascular network. In Figure 9(b), the reconstructed PA images in ROI of animal tumor models with and without the light catcher are compared next to each other. Overall, PA images acquired when using the light catcher (bottom panels in each row) clearly exhibit with higher signal levels than without using light catcher (top panels in each row).

Table 1 summarizes PA signal amplitudes averaged over ROI from each mouse and PA signal enhancement ratio of with and without the light catcher. With the light catcher, the percentage of PA signal enhancement ranges from 26.1% (mouse no. 4) to 37.0% (mouse no. 8) with an average of 33.7%. The statistical power analysis is shown in Figure 9(c). Circles represent the averaged PA signal amplitudes within ROI of each mouse with the light catcher, and triangles are averaged PA signal amplitudes without the light catcher. Central line in the boxplot represents the median, and both edges of the box indicate 25th and 75th percentiles. Two whiskers above and bottom of the boxplot display the range of measurements for the maximum and the minimum value, respectively. A p-value lower than 0.05 determines that PA signal level is significantly enhanced by an average of 33.7% when using the light catcher.

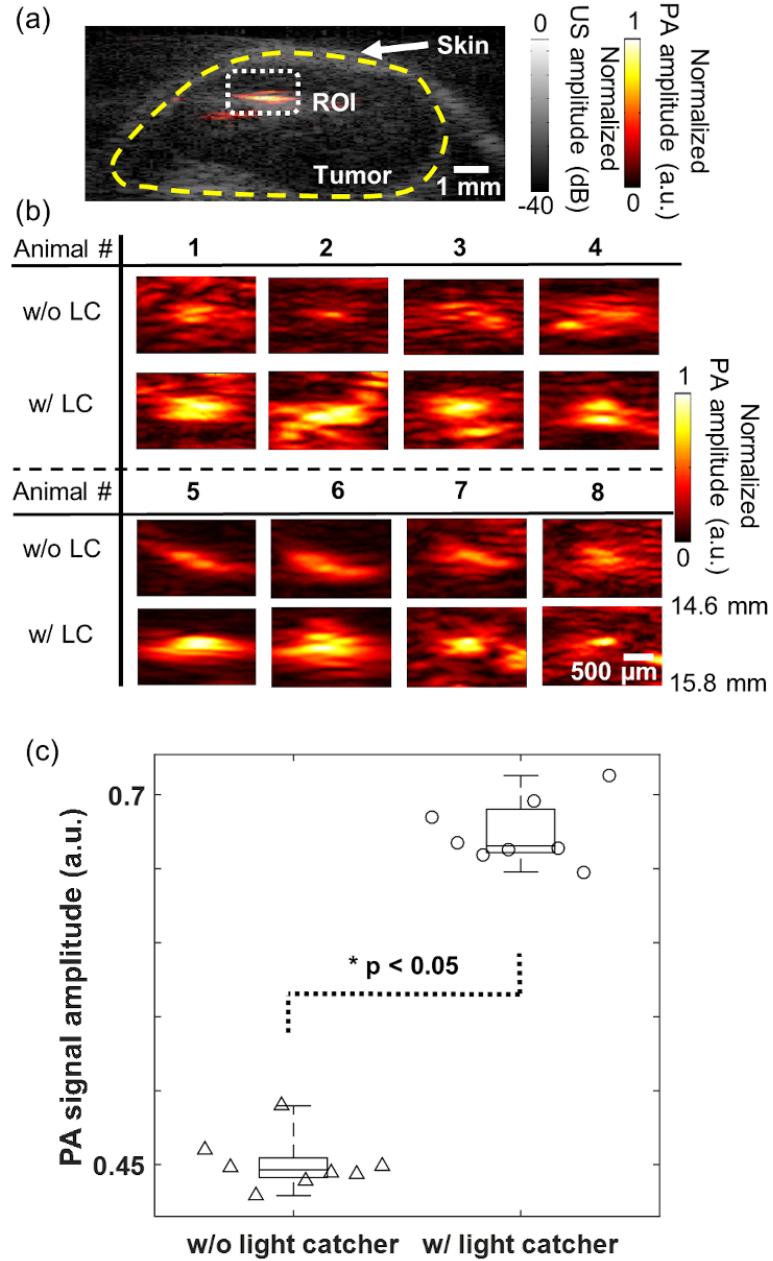


Figure 9. *In vivo* experiment results: Normalized PA images with and without the light catcher. (a) PA image overlaid on ultrasound B-mode image with 40 dB log-compression. The yellow dashed contour represents the tumor location of the mouse and the top layer of the tumor is skin with hair removed. The white dashed box (Height: 1.2 mm, Width: 2.0 mm) indicates the region of interest (ROI) where the photosensitizer is administered. (b) PA images of ROI when using (Lower row) and without using the light catcher (Upper row) for each mouse ($n = 8$) within a depth of 14.6-15.8 mm. All PA images are normalized by measured laser fluence and shown in same dynamic range. (c) Statistical analysis of *in vivo* study results (Table 1). Solid circles and triangles represent averaged PA signal amplitudes in ROI with and without the light catcher, respectively. The central line of the boxplot is median, the edges of the box are 25th and 75th percentiles, and two whiskers above and below of the box are the maximum and the minimum of measurements.

Table 1. *In vivo* experiment results: The normalized and averaged PA signal amplitude (a.u.) in the ROI and enhancement ratio when using the light catcher.

Mouse No.	1	2	3	4	5	6	7	8
PA amplitude w/o LC*	0.46	0.45	0.42	0.49	0.44	0.44	0.44	0.45
PA amplitude w/ LC*	0.68	0.67	0.66	0.66	0.70	0.66	0.65	0.71
Enhancement (%)	32.8	32.9	34.9	26.1	36.9	32.9	31.6	37.0
Averaged enhancement (%)								33.7

*PA signal amplitude of each mouse was mean value in ROI of the injected photosensitizer ($n = 8$). PA signal amplitudes were normalized by the laser fluence. All values are in arbitrary unit (a.u.). w/o LC: without the light catcher; w/ LC: with the light catcher.

In summary, enhancement of the laser fluence in tissues using the developed light catcher is evidenced by the increased PA signal amplitudes measured *ex vivo* in the chicken breast tissues. In an *in vivo* study using the mouse tumor model, significantly improved PA amplitudes are observed when using the light catcher. This suggests the potential of an increased PA imaging depth when using the light catcher. In addition, the light catcher may protect the operator and the subject from unwanted exposure of laser excitation that may allow free-hand PA imaging without needing eye protection goggles. For further translation of this technology and device, a few technical challenges have to be overcome. The current prototype of the reflecting mirror cone is fabricated using rigid, opaque material that makes difficult to use it on non-flat skin surfaces and prevents the operator from seeing the scanning area. Materials that are mechanically compliant and optically transparent to visible light, yet still reflective to the NIR, will be ideal for the reflecting mirror cone. In addition, the cone will have to be reasonably flat as well for easier free-hand scanning, without potentially trapping air bubbles inside. As long as the cone fully covers the skin surface, a similar efficiency can be expected for different geometry. Moreover, the light

catcher can be applicable to other optic-based technology such as PDT that is expected to increase light delivery efficiency thus for potentially improved treatment.

2.4 CONCLUSION

Significant PA signal enhancement by about 33.7 % is shown when using the developed light catcher in an *in vivo* mouse tumor model injected with a clinical photosensitizer, verteporfin that has an absorption peak at 689 nm in NIR. Such enhancement of PA signal amplitude is mainly attributed to improved effective laser fluence at the target depth when using the light catcher that collects and re-distributes the reflected light. This is further supported by both increased laser fluence and PA signal intensity in *ex vivo* chicken breast tissues experiments when using the light catcher. All these *ex vivo* and *in vivo* experiment results are in good agreement with our earlier simulation model [63], [68].

2.5 ACKNOWLEDGEMENTS

This work was supported by International Collaborative R&D Program (M0000053, Development of a Novel Multi-modal *In vivo* Imaging System for Animal-to-Human Use) funded by the Ministry of Trade, Industry and Energy (MOTIE), Korea.

3.0 VAPORIZATION AND RECONDENSATION DYNAMICS OF INDOCYANINE GREEN-LOADED PERFLUOROPENTANE DROPLETS IRRADIATED BY A SHORT PULSE LASER

The work presented in this chapter was reprinted from J. Yu, X. Chen, F. S. Villanueva and K. Kim, “Vaporization and recondensation dynamics of indocyanine green-loaded perfluoropentane droplets irradiated by a short pulse laser”, Appl. Phys. Lett. 109, 243701 (2016); doi: 10.1063/1.4972184, with the permission of AIP Publishing. © 2016 AIP.

Phase-transition droplets have been proposed as promising contrast agents for ultrasound and photoacoustic imaging. Short pulse laser activated perfluorocarbon-based droplets, especially when in a medium with a temperature below their boiling point, undergo phase changes of vaporization and recondensation in response to pulsed laser irradiation. Here, we report and discuss the vaporization and recondensation dynamics of perfluoropentane droplets containing indocyanine green in response to a short pulsed laser with optical and acoustic measurements. To investigate the effect of temperature on the vaporization process, an imaging chamber was mounted on a temperature-controlled water reservoir and then the vaporization event was recorded at 5 million frames per second via a high-speed camera. The high-speed movies show that most of the droplets within the laser beam area expanded rapidly as soon as they were exposed to the laser pulse and immediately recondensed within 1-2 μ s. The vaporization/recondensation process was consistently reproduced in six consecutive laser pulses to the same area. As the temperature of the media was increased above the boiling point of the perfluoropentane, the droplets were less likely to recondense and remained in a gas phase after the first vaporization. These observations will help

to clarify the underlying processes and eventually guide the design of repeatable phase-transition droplets as a photoacoustic imaging contrast agent.

3.1 INTRODUCTION

Perfluorocarbon (PFC) based optically-triggered phase-transition droplets have been recently introduced as a promising contrast agent for photoacoustic (PA) imaging [40], [41], [74], [75]. These PFC-droplets contain a light absorber that increases PFC core temperature with a light input, causing the phase transition from liquid to gas. The resulting rapid expansion of the droplet volume provides significant PA contrast enhancement compared to PA contrast via thermal expansion [76]. Furthermore, once vaporized, echogenicity also dramatically increases to a degree similar to that conferred by microbubbles designed as ultrasound (US) contrast agents. There have been various efforts to utilize optically-triggered droplets for more efficient medical PA imaging techniques. Strohm et al. demonstrated optically-triggered micron-sized PFC droplets, loaded with silica-coated lead sulfide nanoparticles, which work as a contrast agent for PA and US imaging [74]. They described that the PA signal amplitude from the vaporization is linearly proportional to the light absorber payload. Wilson et al. demonstrated contrast enhanced PA imaging using nano-sized PFC droplets containing gold nanorods [40]. PA signal via vaporization was several times higher than PA signal via thermal expansion *in vivo*. Subsequently, Hannah et al. developed an indocyanine green (ICG) loaded nano-sized PFC droplets for contrast-enhanced US and PA imaging in response to a laser excitation [41]. In their study, the PA signal increased as the PFC became superheated and volatile at a higher ambient temperature and therefore vaporized more easily with the same input laser fluence. Later, Asami et al. found repeatability of optically-

triggered droplet vaporization (ODV) that depended on the size of droplets [77]. Up to three times more enhanced PA signals - compared to PA signals from thermal expansion - were continually observed by repeated vaporization and recondensation processes of droplets 0.2-1.0 μm in diameter. However, the underlying mechanism of the ODV has not been fully unveiled due to the complexity and involvement of various parameters in the above studies. Lajoinie et al. observed the dynamics of the vaporization process of micron-sized PFC droplets under controlled environments using a high-speed camera. They suggested a model incorporating thermal diffusion of the heated hexadecane core with an ambient medium through the droplet shell [78]. In the present study, the phase transition dynamics of droplets undergoing the repeated vaporization and recondensation process in response to each short pulse laser and resulting PA signals were further investigated by concurrently recording acoustic signals and vaporized droplet shell motion dynamics. The relationship between PA signal amplitude and droplet size was determined and compared with those of the analytical model. The stability of the droplet, which showed dependency on the size and the ambient temperature, is discussed; these observations may help guide droplet design and lead to further advanced investigation.

3.2 MATERIALS AND METHODS

3.2.1 Synthesis of PFC droplet

Droplets were synthesized using an adapted method previously reported by other groups [41], [79]. Droplets contained perfluoropentane (PFP, C_5F_{12} , Boiling point of 29°C , Fluoromed) as a phase-transition medium, bovine serum albumin (BSA, Sigma-Aldrich) shell, and ICG

(Sigma-Aldrich) for localized volume heating with a laser input. Initially, blank droplets were emulsified by sonication (75D, VWR) using a mixture of PFP 0.3 mL and BSA solution (2 mg/mL) 2.7 mL in an iced water bath. Blank droplets were aspirated from the upper layer while residual PFP solution sank to the bottom. ICG was encapsulated by sonicating a mixture of 1 mM ICG and 6 mM tetrabutylammonium iodide (Sigma-Aldrich) solution in chloroform. The prepared ICG solution was supplemented dropwise with blank PFC droplets using a stirrer at 1,200 rpm (IsoTemp, Fischer Scientific). The droplets in the suspension were carefully extracted and then washed three times by discarding the light-green colored supernatant after centrifuging. The absorption peak of the droplet is around 800 nm. The design of a droplet is illustrated in Figure 10(a). Confocal fluorescence microscopy images (IX-81, Olympus) taken from a droplet pre- and post- vaporization are shown in Figure 10(b). ICG in the core of the droplet before vaporization was pushed into the outer-shell after vaporization.

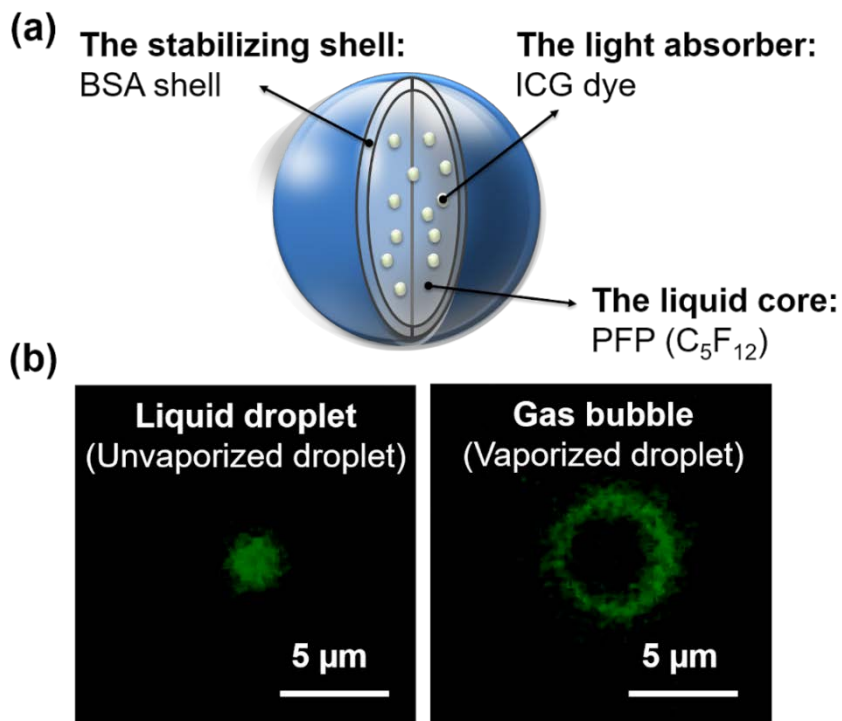


Figure 10. Schematic of the ICG-loaded PFP droplets (a); Confocal fluorescent microscopy image of a droplet (b) before vaporization (Left panel) and after vaporization (Right panel).

3.2.2 Experiment setup

To obtain a sufficient temporal resolution for optical observation of the dynamics of an ODV, high-speed microscopy with a water-immersion objective lens (LUMPLFLN $\times 60$, Olympus) was employed (Figure 11) [80]. An Opticell cartridge (ThermoScientific), injected with the sample suspended in equilibrated, gas-saturated de-ionized water to be investigated, was placed on the top of a temperature-controlled reservoir filled with de-ionized water. No investigation on potential effects by medium viscosity was performed in this study. The reservoir contained a focused single-element ultrasound transducer (V306-SU, 2.25 MHz, 60% bandwidth, Olympus) for PA signal detection. The transducer focus was co-aligned with the optical focus of the microscope, at an angle of 45° from the Opticell membrane. The detected PA signal was amplified by an ultrasonic receiver (PR-5900, Olympus) and digitized (WaveSurfer 452, Lecroy). The receiver circuitry was calibrated by using theories developed previously [81]–[83]. A strobe light (MVS-700, PerkinElmer), triggered from the camera timing board, was used as the light source for bright-field imaging. A laser pulse of 5-ns-long tuned at 800 nm by an optical parametric oscillator (Vibrant HE532I, OPOTEK) was delivered through a custom-made optical fiber (OZ optics) aligned with the microscopy. The excitation laser spot size of homogeneous Gaussian distribution was set to be around 40 μm in diameter to assure only individual droplet can be optically-activated.⁹ The laser fluence exposed to the sample was estimated to be 1.2 J/cm^2 . A near-infrared (NIR)-reflected dichroic mirror (ZT660DCSPXR, Chroma) was installed in a right-facing cube (IX2-MFB-SP-R, Olympus) to align the two optical paths: white light for imaging (red arrow in Figure 11) and NIR light for ODV (green arrow in Figure 11). An emission filter (FF01-650, Semrock) was used to reject any interference with excitation laser on recorded videos. These

three independent systems - an ultrasound measurement system, a high-speed camera, and a laser system - were synchronously interfaced by a custom-made timing controller. To calculate the acoustic pressure radiated from a droplet that undergoes rapid expansion and compression, radius-time curve was measured on the recorded high-speed video. Measured radius were interpolated, and then plugged into the analytical model for acoustic pressure estimation from a spherical bubble described by

$$P(r, t) = \rho_l \frac{R(t)}{r} \left(2\dot{R}(t)^2 + R(t)\ddot{R}(t) \right) \quad (2)$$

where ρ_l is the liquid density, $R(t)$ is the droplet radius, $\dot{R}(t)$ is the shell velocity, $\ddot{R}(t)$ is the shell acceleration, and r indicates the radial location in a spherical coordinate system [78], [84], [85]. A bandpass filter (0.5-3.2 MHz) was applied to the calculated pressure. All analyses were performed in MATLAB (Mathworks).

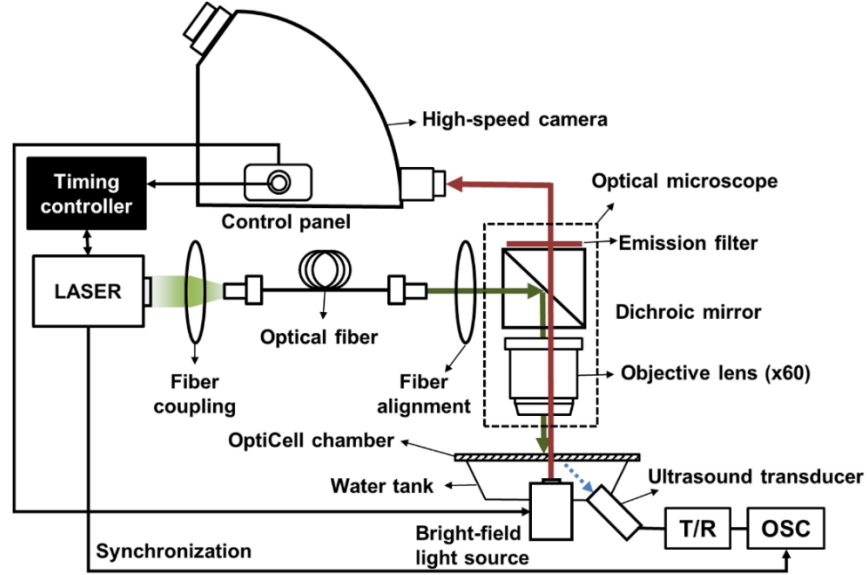


Figure 11. Experiment schematic. A high-speed optical microscopy apparatus equipped with a water immersion objective lens (60×) was combined with NIR laser for PA excitation. Short pulse laser of 5 ns duration tuned at 800 nm was illuminated onto the target through the objective lens. Acoustic signal from vaporization was captured by a single element focused ultrasound transducer. Green and red arrows represent the light paths of the excitation laser for vaporization and white light for brightfield imaging, respectively. Acoustic and optical systems were aligned on the focal plane of the sample and synchronized through a custom-made FPGA-based timing controller. T/R: Transmitter/Receiver, OSC: oscilloscope.

3.3 RESULTS AND DISCUSSIONS

A directly recorded PA signal from individual droplet was compared with the estimated acoustic pressure using an analytic model for two different size droplets. Figure 12 depicts selected frames cropped from the high-speed movies at every 0.2 μs during the vaporization (transient expanding) and recondensation (transient shrinking) processes of a large (Diameter: 4.8 μm) and a small (Diameter: 2.0 μm) droplet. The concurrently recorded acoustic emissions by the ultrasound transducer was compared with the pressure estimated using the analytic model in Eq. 2 at room temperature (20°C) as shown in Figures 12(c, f). Note that a single laser pulse was used to excite the sample at time 0 μs . For the larger droplet, the radius increased from 2.4 to 8.3 μm - approximately 3.5 times. The first 0.8 μs during which the droplet continued to expand represents the vaporization period. It was noted that the radius and interfacial velocity rapidly increased in the first 200 ns and the corresponding peak pressure was 70.5 pascal (Pa) in the envelope signal at 184 ns when the droplet had the highest shell velocity and acceleration. In the subsequent 1 μs , the contracting process followed. During the period of 0.8 to 1.3 μs , PA signal was not detected since the shell radius remained nearly constant. The subsequent radius decreases contributed to another positive peak toward the tail of the signal. Approaching the end of contracting phase, a number of small daughter droplets were identified. The thin albumin shell of the droplet might have ruptured due to the vigorous dynamics of the contracting phase, which might have broken the symmetry of the droplet [86]. For the smaller droplet, the radius increased from 1.0 to 2.4 μm - approximately 2.4 times. Peak pressure of the envelope signal was measured 7.8 Pa at 374 ns. In both cases, the predicted acoustic pressure compared reasonably well with the recorded pressure. As seen in Eq. 2, acoustic pressure from the vaporization process is a function of the time-dependent radius, and its first and second time derivatives. For instance, a larger droplet and faster shell velocity during

vaporization should generate a larger PA signal. In Figure 12(c, f), a larger PA signal amplitude was detected from a larger droplet with the same laser input fluence. Therefore, if utilizing larger droplets under the same circumstances such as ambient pressure and temperature, a larger PA signal is expected when excited with the same laser fluence. However, droplets with larger diameters can become unstable. Some larger droplets ($>7.5 \mu\text{m}$) tended to grow continually into a giant gas bubble after undergoing a single vaporization and contraction event. Their instability must have prevented repetitive ODV.

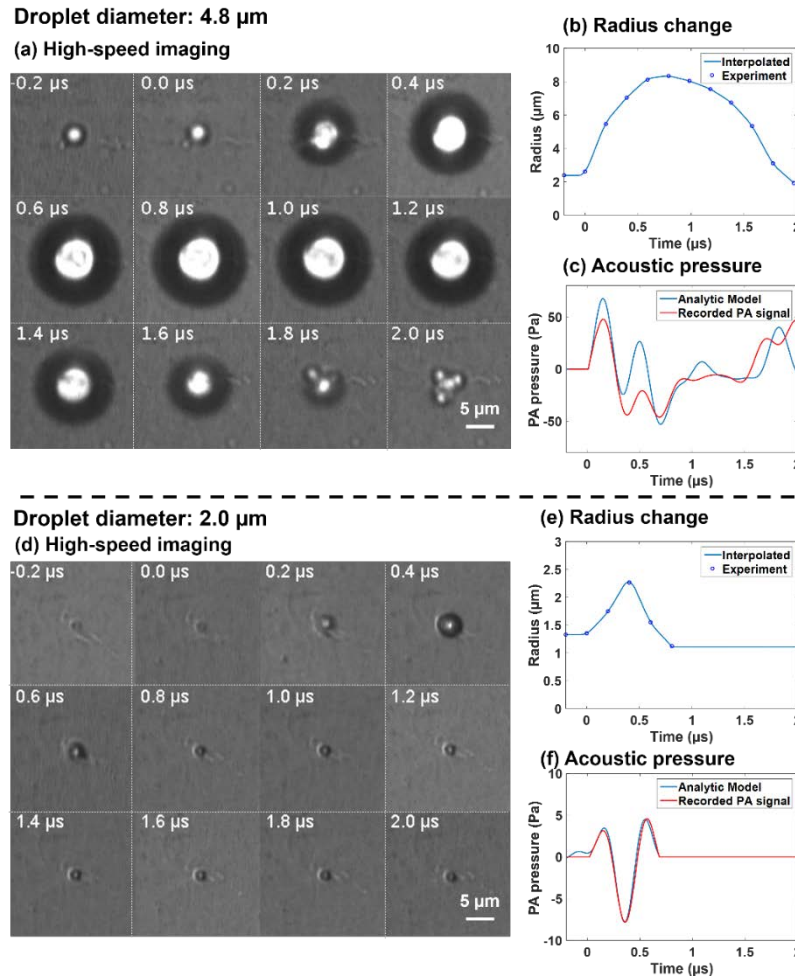


Figure 12. Selected frames of high-speed imaging at 5 million frames per second (a, d) and acoustic signal measurement (Red solid line in (c, f)) and theoretical estimation (Blue solid line in (c, f)) from shell dynamics of a large droplet (Diameter = $4.8 \mu\text{m}$, (a-c)) and a small droplet (Diameter = $2.0 \mu\text{m}$, (d-f)) with short pulse laser excitation. (5 ns duration, 800 nm wavelength). Laser was excited at $0 \mu\text{s}$. Analytic pressure calculation was performed using Eq. 2 with radius-time curves (b, e) measured by high-speed optical imaging.

Figure 13 compares the repeatability and stability in response to the same laser exposure of two different size droplets, 2.0 and 7.7 μm . Figure 13(a) delineate the dynamics of a 2.0 μm droplet in response to consecutive laser excitations at different time points: prior (far left panel) and one-hour post exposure to six laser pulses (far right panel). Three snapshots are shown from each laser pulse at 0, 0.4 and 1.0 μs post excitation. The absence of apparent changes in size between pre- and post- multiple laser exposures indicates the stability of a 2.0 μm droplet. Corresponding PA signals were measured with similar amplitudes over each laser pulse, as similarly observed by others [77]. However, a droplet of 7.7 μm (Figure 13(b)) was so unstable that it grew continually into a giant gas bubble without contracting after a laser excitation. The bubble started to float away from the imaging plane at 1 second post excitation. Consistent observations ($n = 5$ at each size) from multiple experiments with droplets of similar sizes indicate that droplets less than 2-3 μm are more stable than larger ones of 4.5 μm or more.

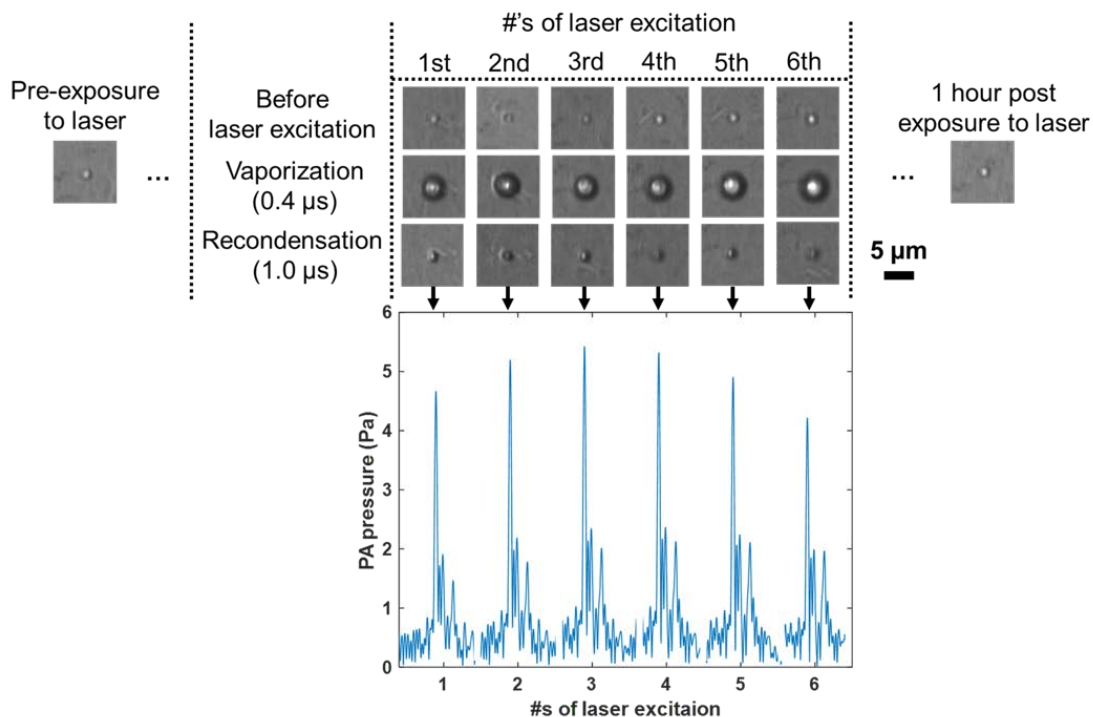
The high stability of these droplets formed in a micro- or nano-scale could be attributed to the increased boiling temperature from increased Laplace pressure which is inversely proportional to the size of the droplet as described by

$$P_{\text{inside}} - P_{\text{outside}} = \frac{2\sigma}{R} \quad (3)$$

where P_{inside} is the pressure inside a droplet, P_{outside} is the ambient pressure, σ is the surface tension of the shell, and R is the droplet radius [76], [87]. For example, estimated vaporization temperatures of droplets with 1, 3, 5, 7, and 9 μm in diameter (Appendix B for more detail) are 73.2, 49.5, 42.6, 39.3 and 37.3°C, respectively, for a given $\sigma = 75 \text{ mN/m}$ (at BSA concentration of 2 mg/mL) [76], [87], [88]. As a result, micron-sized droplets ($\sim 9 \mu\text{m}$) can remain in quasi-superheated state without spontaneous vaporization at body temperature, because the Laplace pressure of the droplet is sufficiently high such that the boiling point is increased to above the

boiling temperature of the bulk liquid. Therefore, the size of droplets should be carefully selected for repeatable ODV.

(a) Droplet diameter: 2.0 μm



(b) Droplet diameter: 7.7 μm

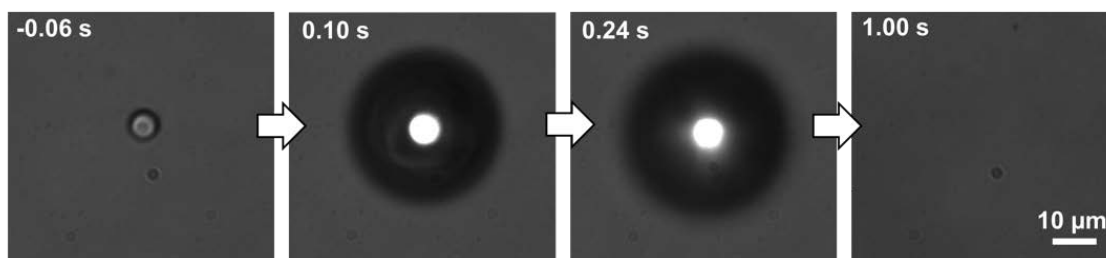


Figure 13. Repeatability of vaporization-recondensation and stability of droplet. (a) Optical (top panels) and acoustical (bottom panels) observations over 6 laser excitations on the same droplet measuring 2.0 μm in diameter at baseline. The envelopes of PA pressure were measured from multiple ODV processes of the same single droplet and corresponding high-speed images of each vaporization are shown in the top panel. Far left and far right panels depict droplets initially and 1 hour later, respectively. (b) Optical recording of a larger droplet (7.7 μm baseline diameter) over 1 second, imaged at lower frame rate. The vaporized droplet continually expanded after vaporization, and then floated away at 1 second.

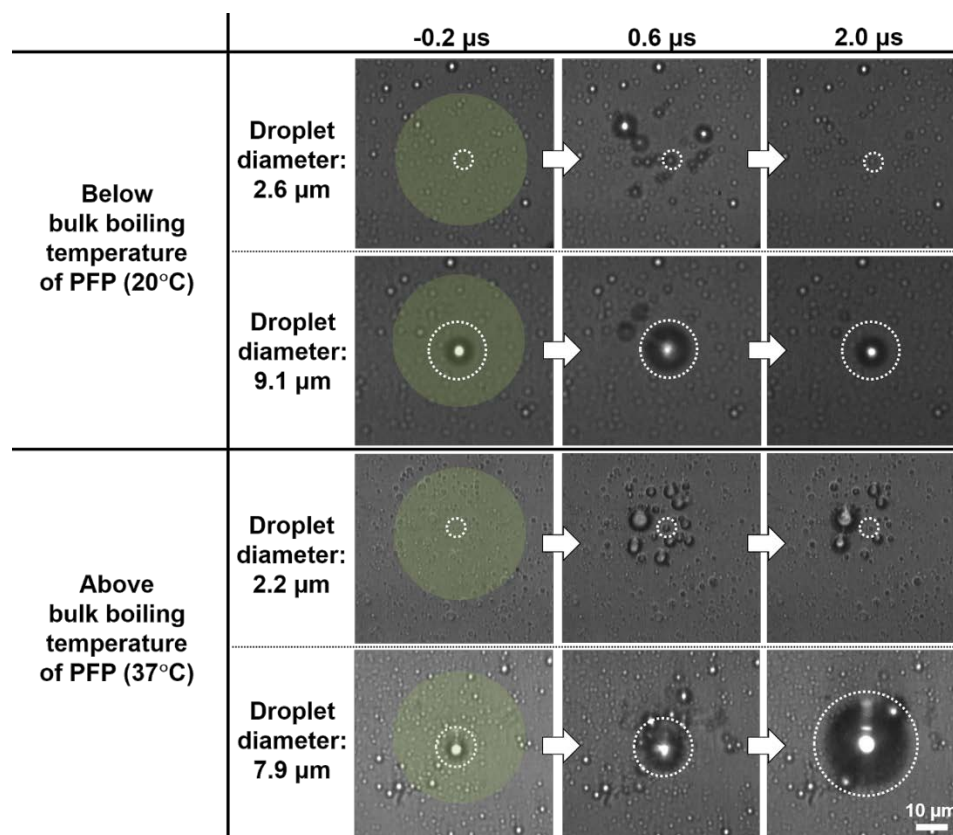


Figure 14. Laser-induced vaporization of various sized droplets at different ambient temperatures. The snapshots at three different time points of 0.2 μ s before laser excitation (left column), 0.6 μ s after laser excitation (center column) and 2 μ s after laser excitation (right column) during vaporization-recondensation processes below the bulk boiling temperature (20°C, top two rows) of PFP and above boiling temperature (37°C, bottom two rows) are depicted. Note that a laser pulse of 5 ns-long was induced at time 0 s over the circled area in green as shown in the left column. The dotted white circle identifies the droplet of interest located at the center of laser beam. The relatively large droplet (diameter of 7.9 μ m) in a medium with temperature above the bulk boiling temperature of PFP did not recondense after vaporization.

In order to study the effects of ambient temperature, droplets of 1-9 μ m were exposed to a laser pulse when in the medium with controlled temperature above (37°C) or below (20°C) the bulk boiling temperature of PFP. The vaporization-recondensation dynamics of different size of droplets under different ambient temperatures in short (initial 2.2 μ s) timescales were presented in Figure 14. The white dotted circle indicates droplets centered at the laser exposure spot illustrated in light-green circle. When the media temperature was below the boiling temperature, all of the droplets immediately shrunk back to their initial sizes following the ODV. However, large droplets

(>7 μm) grew continually after a brief contracting, and finally floated away from the field of view after 5 min. This transient contracting may be attributed to the partial recondensation of the vaporized PFP core and the diffusion of dissolved gas from surrounding medium into the liquid-gas mixed droplet, as similarly shown in an acoustic droplet vaporization, and may have caused growing of the liquid-gas mixed droplet [89]–[94]. When the media was at temperatures above the boiling point of PFP, only small droplets ($\sim 2\ \mu\text{m}$) recondensed after vaporizing. Droplets larger than 3 μm grew continually with vigorous coalescences between neighboring vaporized droplets and eventually floated after 5 min without recondensation.

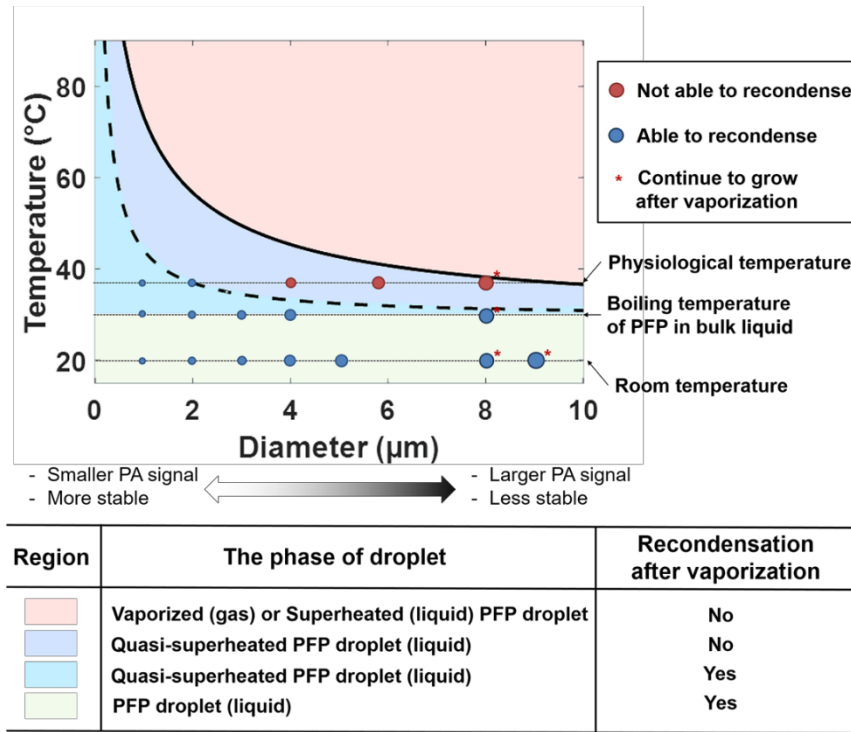


Figure 15. Summary of observation and interpretation of experimental results. Each solid circle represents a measurement condition ($n = 3$, data binned with $\pm 0.5\ \mu\text{m}$). Recondensation was observed in blue colored droplets, and not observed in red colored droplets. Note each circle was scaled to the initial droplet size. *These droplets grew continually into a large gas bubble at later time. A droplet can be placed in three different states: (1) Vaporized (gas) or superheated state (liquid, light-red region), (2) Quasi-superheated state (liquid, light-blue or light-purple region), (3) liquid state (light-green region). The solid curve represents the size-dependent estimated boiling points of droplets as a reference threshold for vaporization. The dotted curve indicates the initial size of the droplets at each given temperature that can reach to the size on the solid curve at the same temperature after vaporization. Therefore, the droplets below the dotted curve will likely recondense, while those above will likely not recondense after vaporization.

A summary of our observation and interpretation is illustrated in Figure 15. Each circle represents the baseline diameter of droplet on each experimental data point ($n = 3$). Color of the circle indicates whether recondensation after vaporization was observed (blue) or not (red). The solid curve represents the size-dependent increased boiling temperature of the droplet as a threshold for vaporization [76], [87], [88]. The dotted curve indicates the initial size of the droplets at each given temperature that can reach to the size on the solid curve at the same temperature after vaporization. The expansion ratio between liquid and gas was calculated using Eq. 3. The internal pressure, P_{inside} , was calculated using the ideal gas law combined with the conservation of mass between the initial droplet and the resulting bubble. Note that for this purpose, we assumed all PFP liquid contained in the droplet was fully vaporized. Therefore, the dotted curve separates the droplets that will likely recondense (below the dotted curve) from those that will likely not recondense after vaporization (above the dotted curve). A droplet can be placed in three different states, vaporized (gas) or superheated (liquid) state above the solid curve (light-red region), quasi-superheated state (liquid) between the solid curve and the bulk boiling point of PFP (light-purple and light-blue region), and normal liquid state below the bulk boiling point of PFP (light-green region).

3.4 CONCLUSIONS

Overall, experimental results agree well with the theoretical estimation. Droplets that are relatively large tend to generate larger PA signals, but are likely unstable. Once vaporized, unstable droplets reacted in two different ways: some continue to grow without recondensing (red circle

with asterisk), while others continue to grow after transient contracting (blue circle with asterisk) likely due to partial recondensing of the PFP core. Conversely, stable droplets (blue circle without asterisk) that were relatively small exhibited multiple laser-induced vaporization-recondensation repeatedly with a relatively small PA signal amplitude compared to the large droplets. In addition to the effect of initial droplet size, stability would also be affected by ambient medium temperatures relative to the boiling temperature. Based on this consideration, a liquid core with a higher boiling temperature, such as perfluorohexane (C_6F_{14} , Boiling point of $56^\circ C$), may confer greater stability. In this study, thermodynamic aspects of the liquid-gas phase transition were not considered. Only droplet shell dynamics due to phase transition were studied in relation to resulting PA signal generation given fixed input laser fluence and core material. In order to further explore the underlying mechanism of ODV, a computational multiphase transition model must be developed. This developed model may foster more optimal design parameters of optically-triggered droplets that include dye concentration, core materials, shell properties, as well as input laser fluence [41], [74], [95]–[101]. For further understanding of droplet dynamics under biologically relevant conditions such as body fluids or blood, viscosity of the medium also has to be considered [102]–[107].

4.0 PHOTOSTABLE, HYDROPHILIC, AND NEAR INFRARED QUATERRYLENE-BASED DYES FOR PHOTOACOUSTIC IMAGING

The work presented in this chapter was reprinted, with permission, from J.Yu, S. Pin, X. Lin, M. Bai and K. Kim, “Photostable, Hydrophilic, and Near Infrared Quaterrylene-based Dyes for Photoacoustic Imaging” that has been under reviewed.

Novel near-infrared contrast agents based on quaterrylene structure were strategically developed and tested for high photo-stability. Both a dendrimeric quaterrylene molecule, QR-G2-COOH, and a small molecule cationic quaterrylene dye, QR-4PyC4, remain optically stable and continue to generate competitive photoacoustic signal amplitude when irradiated by short near-infrared laser pulses for a relatively long time in in-vitro cell study, unlike indocyanine green that rapidly decrease photoacoustic signal amplitude. The small molecule dye, QR-4PyC4 exhibits not only significantly higher cellular uptake rate than QR-G2-COOH and indocyanine green, but also low toxicity at concentration of up to 10 μ M. The dendrimeric dye, QR-G2-COOH that has surface functional groups available for conjugation with targeting and therapeutic agents shows the highest photoacoustic amplitude with high optical stability. Therefore, QR-4PyC4 can be a promising universal, sensitive and reliable photoacoustic contrast agent and QR-G2-COOH has great potential as a nano-platform with stable photoacoustic imaging capability.

4.1 INTRODUCTION

Photoacoustic (PA) imaging is a multi-wave imaging technology with a conversion from light energy to acoustic energy, exploiting both optical and acoustical characteristics. The PA signal generated from the thermo-elastic expansion of the tissue irradiated by a short-pulse laser is received by a ultrasound transducer, being able to provide optical contrast at ultrasonic imaging depth as complementary benefits from both technologies [108]. In efforts to enable PA imaging technology to detect biomarkers of interest with high sensitivity and specificity, several exogenous PA contrast agents, for example, organic dyes [109]–[111], carbon nanotube [112]–[114], gold nanoparticles [25], [115]–[119], and optically activatable phase-transition droplet [39], [40], [74], [120] have been developed. Some features as an ideal PA contrast agent include (1) a high molar absorption coefficient with low quantum yield at other than visible and infra-red (IR) region, preferably chosen in near-infrared (NIR) region, to maximize imaging depth and signal-to-noise ratio (SNR), because most endogenous optical contrast such as blood in vasculature [21], [43] and primary or metastatic melanoma [44] strongly absorb the visible or IR light [45], (2) high photostability which is necessary for a consistent long-term monitoring of biological activity progress under physiological environment *in vivo* [46], [47] and (3) high intracellular uptake or binding affinity, which determines functional or molecular selectivity. A common strategy is to conjugate targeting molecules to PA contrast agents to allow for specific binding to the target [42]. However, most current organic dyes used for PA imaging suffer from photobleaching or/and low cellular uptake [48], [49]. In addition, cell viability is an absolute prerequisite for practical usefulness just like for any other *in vivo* molecular imaging modality. For example, quantum dots (QD) has been studied as highly resisting to photobleaching with great PA contrast agent [50], but its toxicity prevents QD from being widely spread for *in vivo* imaging study.

In this study, to mainly overcome the poor photostability of most current PA contrast agents, we report two strategically designed agents based on the quaterrylene structure, a dendrimeric quaterrylene molecule (QR-G2-COOH) and a small molecule cationic quaterrylene dye (QR-4PyC4). We choose the quaterrylene structure because our recent study suggests that quaterrylene-based agents can be highly photostable at NIR ranges [46]. Quaterrylene dyes have also been reported to have extremely high chemical stability as they can be heated to 570 °C without decomposition or melting [121]. PA contrast agents can be generally categorized into small-molecules such as dyes [122], [123], nanoparticles such as gold nanoparticles, carbon nanotubes and organic polymer nanoparticles [115], [124]–[126], and combination of both [116], [127]. Nanoparticles have high chemical, structural flexibility for incorporating targeting, signaling and therapeutic moieties and small molecules can easily pass through physiological barriers and get cleared quickly from biological systems [45]. For our newly developed PA contrast agent, the dendrimer represents a nanoplatform for PA imaging with surface functional groups available for conjugation with targeting and therapeutic agents to image/treat specific target of interest, and the small molecule cationic quaterrylene dye represents a universal PA agent, which is designed to provide high PA imaging intensity with high intracellular uptake efficiency that does not require a binding ligand to cell surface biomarkers. The generation-2 dendrimer (QR-G2-COOH) is selected in this study, because lower generations (generation 1-2) show lower fluorescence quantum yield and therefore higher non-radiative conversion of light energy to heat to provide strong PA signal [42], while the QR-G2-COOH dendrimer still has sufficient surface carboxyl functional groups to allow for bioconjugation [128]. Moreover, both contrast agents are tuned to have strong absorption spectrum at NIR region of 650-850 nm, which is the preferably chosen PA imaging window in medical applications for low background endogenous molar

absorptivity, therefore maximum imaging depth and SNR [63], [111]. Photostability of both agents in a small tube is tested followed by an intracellular uptake experiment, comparing with a representative PA agent, Indocyanine green (ICG) that is the only NIR dye approved by Food and Drug Administration.

4.2 MATERIALS AND METHODS

4.2.1 Materials: Synthesis of QR-4PyC4 and QR-G2-COOH

The solvents used are of commercial grade. The synthesis of QR-G2-COOH shown in Figure 16(a) was reported in our previous study [46]. The precursor of QR-4PyC4, QR-4Py shown in Figure 16(b), was synthesized by following our reported procedures [129]. Silica gel (standard grade, 60A, Sorbtech, Norcross, GA, USA) column chromatography was used to purify synthesized compounds. The ^1H and ^{13}C NMR spectra were recorded on the Bruker Avance III 400 MHz instruments. UV/Vis spectra were recorded on a Cary 100 Bio UV-Vis spectrophotometer, and fluorescence spectra were recorded on a Cary Eclipse fluorescence spectrophotometer. The following instrument and reagent were applied in the cell viability evaluation: SynergyTM H4 Hybrid Multi-Mode Microplate Reader (BioTek, Winooski, VT, USA) was used for cell via, Zeiss Axio Observer fluorescent microscopy system (Zeiss, Jena, Germany), 96-well optical black plates (Fisher Scientific, Pittsburgh, PA, USA), CellTiter-Glo Luminescent Cell Viability Assay kit (Promega, Madison, WI, USA).

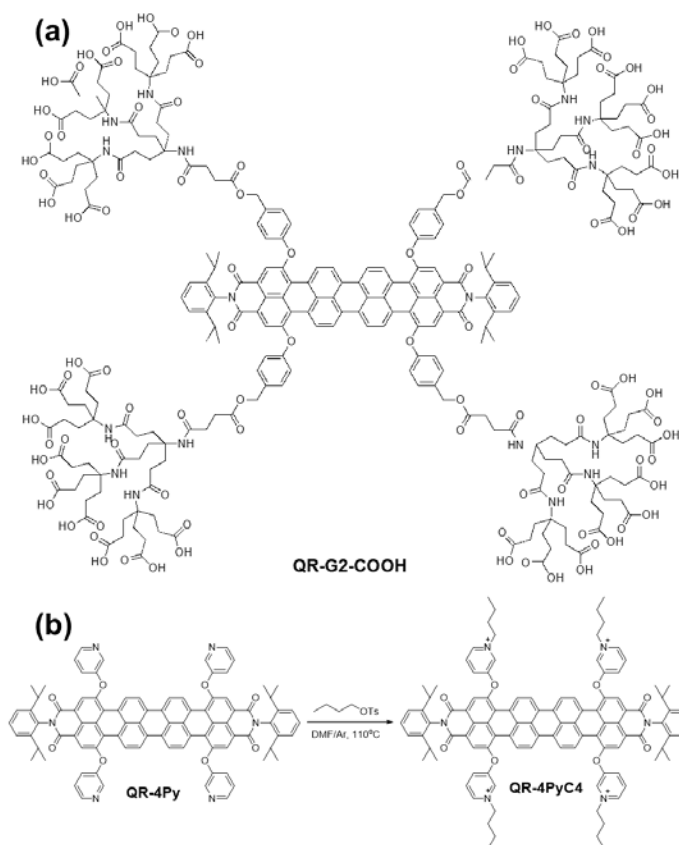


Figure 16. (a) Chemical structure of QR-G2-COOH; (b) The precursor QR-4Py and the synthetic route of QR-4PyC4

The precursor QR-4Py (12.5 mg, 9.4 μ mol, Figure 16(b)) was heated at 110 $^{\circ}$ C in dimethylformamide (2 mL) under argon. 4-Methylbenzenesulfonate (1 mL, 4.9 mmol) was added and the resulting mixture was kept at 110 $^{\circ}$ C for 3 days. After the reaction mixture was cooled to room temperature, dimethylformamide was removed by rotary evaporation. The green solid was purified by dialysis (membrane cutoff = 1000) in methanol first and then in water for 2 days. QR-4PyC4 (16 mg, 76 %) was obtained after being dried in lyophilizer. ^1H NMR (400 MHz, d_4 -MeOD, 25 $^{\circ}$ C, TMS): δ = 9.14 (s, 4 H), 9.07 (d, J = 8 Hz, 4 H), 8.61-8.65 (m, 8 H), 8.44 (s, 4 H), 8.37 (d, J = 8 Hz, 4 H), 7.94-7.98 (m, 4 H), 7.53 (d, J = 8 Hz, 8 H), 7.46-7.50 (m, 2 H), 7.34 (d, J = 7.6 Hz, 4 H), 7.04 (d, J = 8 Hz, 8 H), 4.45 (t, J = 7.2 Hz, 8 H), 2.85 (sep, J = 6.8 Hz, 4 H), 2.20

(s, 12 H), 1.75-1.79 (m, 8 H), 1.12-1.14 (m, 32 H), 0.74 (t, $J = 7.2$ Hz, 12 H). ^{13}C NMR (d_4 -MeOD): δ =164.30, 157.32, 151.44, 147.19, 141.45, 141.08, 136.56, 134.73, 133.17, 131.82, 131.36, 130.55, 130.04, 129.74, 128.09, 127.98, 127.76, 127.07, 126.81, 125.19, 123.82, 63.23, 34.35, 30.30, 24.53, 21.25, 20.18, 13.76.

4.2.2 Cell culture of MDA-MB-231

MDA-MB-231 cells were cultured in Dulbecco's Modified Eagle's Medium (DMEM, Sigma-Aldrich, St. Louis, MO, USA) containing 10% fetal bovine serum (FBS, Fisher Scientific, Pittsburgh, PA, USA), and 1% Penicillin-Streptomycin-Glutamine (Life Technology, Carlsbad, CA, USA). Cells were incubated in a water jacketed incubator (37 °C, 5% CO₂).

4.2.3 Cytotoxicity evaluation of QR-4PyC4

Cell viability was determined by CellTiter-Glo assay per the manufacturer's instructions. The luminescent intensity was directly proportional to the amount of remaining viable cells. Cells were seeded into 96-well plates, incubated for 24 h, and then treated with QR-4PyC4 (0.1, 0.5, 1, 5, 10, and 20 μM) for 6 hours. Doxorubicin (DOX, 50 μM) was used as the positive (toxic) control. Cell medium was used as the negative (non-toxic) control. Cell viabilities were determined by recorded luminescent intensity in each group over that of the vehicle group.

4.2.4 Cellular uptake study

The cell uptake of ICG, QR-G2-COOH and QR-4PyC4 were evaluated in MDA-MB-231 cells, which were seeded onto 96-well plates and incubated for 24 h before treatment. The cell uptake of ICG was measured by fluorescence. The fluorescence intensities were recorded using a plate reader (excitation/emission 750/820 nm). Cells were treated with ICG (10 μ M) and then divided into two groups (4 wells/group): experiment group was washed with PBS once to remove extracellular ICG and control group was used without wash. The cell uptake of ICG was calculated as the ratio of the fluorescence intensity of the experiment group to that of the control group.

The cell uptake of QR-G2-COOH and QR-4PyC4 was evaluated using modified extraction method [130]. To account for the low fluorescence signal from QR-G2-COOH and QR-4PyC4 upon irradiation, we used absorption to quantify the cell uptake, instead of fluorescence. Cells were divided into 3 groups (4 wells/group). The experiment group, control group, and the third group was used for absorption background calibration. The medium in the control and background groups was removed gently, and 10 μ M of dye (QR-G2-COOH or QR-4PyC4) in DMSO and pure DMSO were added, respectively, followed by absorption measurement. For the experiment group, cells were treated with dye (10 μ M) in cell medium for 6 h, washed with PBS once and DMSO was added to extract intracellular dye molecules for absorption measurement. Raw absorption values were recorded using a plate reader, and true absorption values were obtained after subtracting the background reading. The cell uptake is calculated as the ratio of the absorption intensity of the experiment group to that of the control group.

4.2.5 Photoacoustic imaging and bright-field imaging

Acoustic-resolution photoacoustic microscopy system was utilized for all this study to acquire PA images (Figure 17). A tunable laser system with an optical parametric oscillator (OPO, Vibrant HE532I, OpoTek, Carlsbad, CA, USA) pumped by Q-switch Nd: YAG pulsed Laser (Quantel, Bozeman, MT, USA) generates a short pulse of 5 ns long at pulse repetition frequency of 10 Hz. The pulse laser wavelength is tuned at 740 nm to have similar absorption coefficients for QR-4PyC4 and QR-G2-COOH. The collimated laser beam was focused by a concave lens and then illuminated onto the target. Target can be moved by dual-axis motorized translational stage (T-L SR150B, Zaber, Vancouver, BC, Canada) for raster scanning. The excited laser energy was monitored using an energy meter (EnergyMax, J-50MB-YAG, Coherent, Santa Clara, CA, USA). Measured laser pulse fluence is approximately 22 mJ/cm², satisfying the American National Standards Institute safety guideline for laser use (ANSI, Z136.1). A focused single element ultrasonic transducer (V375, $f_0 = 30$ MHz, Olympus NDT, Waltham, MA, USA) was employed to detect the PA signal. Received PA signal was amplified (5900PR, Olympus NDT, Waltham, MA, USA), and then digitized by an oscilloscope (WaveSurfer 452, LeCroy, Chestnut Ridge, NY, USA). Laser excitation system and data acquisition system were synchronized.

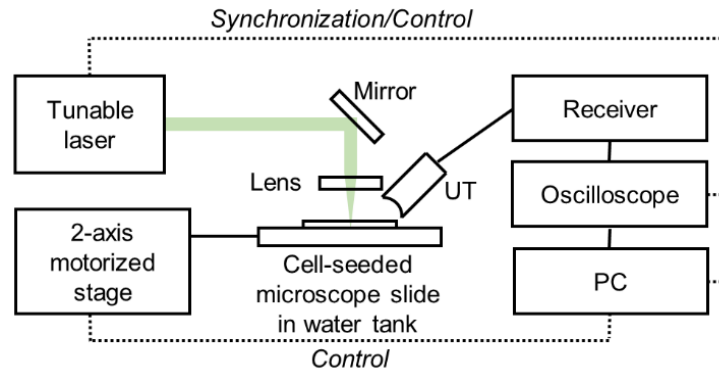


Figure 17. Acoustic-resolution photoacoustic microscopy setup for cell study. UT: Single element focused ultrasound transducer ($f_0 = 30$ MHz)

A lowpass filter (cut-off bandwidth: 45 MHz) was applied to the raw RF PA signal, and then its envelope was extracted using the Hilbert-transform to generate a PA image. For photostability study, PA signal amplitudes were continuously measured from the polyethylene tube (PE-50, Inner diameter: 580 μm ; Outer diameter: 965 μm , BD intramedic, Franklin Lakes, NJ, USA) filled with the diluted dye solution at 10 μM . For cell study, cell treated with each dye on the slide was located on the slide holder. The scan area was about 3.2 mm length by 2.4 mm width with 400 μm step size. The diameter of the irradiation beam size is larger than this area to provide the uniform light illumination. The PA signal was averaged three times at each scanning grid point to minimize the pulse-to-pulse energy variation and to increase the signal to noise ratio. The maximum amplitude projection and log-compression were applied to the filtered data. All signal processing was performed offline using MATLAB software. For verification purpose, cell locations were derived as a ground truth for PA image. Raster scanned multiple bright-field images by using inverted microscope (IX-81, Olympus, Center Valley, PA, USA) were stitched to form single image. To select only nuclei on the image, image contrast was adjusted higher, and then local maxima represented in green dots with proper threshold was derived by using ImageJ software. The image of localized cells was overlaid on the PA image for comparison

4.3 RESULTS AND DISCUSSIONS

4.3.1 Dendrimer characterization

Dendrimers provide a superior nanoplatform due to their precisely controlled size, shape, and surface chemistry. These unique properties allow dendrimers to be developed with high

structural mono-dispersity, desired plasma circulation time and bio-distribution properties, as well as control over drug release. In addition, targeting moieties can be attached to the surface functional groups of dendrimers to allow targeted drug delivery, and signaling molecules can be attached to monitor drug delivery, release, and efficacy. We recently reported a series of quaterylene-based dendrimers for fluorescence imaging [46]. We found that these quaterylene-based dendrimers are biocompatible and show intense NIR absorption, with remarkable chemical and photostability. Importantly, the low generation quaterylene-based dendrimers show minimal fluorescence quantum yield; therefore, it may generate strong PA signal. In this study, we choose the second generation, QR-G2-COOH (Figure 16(a)), to evaluate the potential in PA imaging. In addition to QR-G2-COOH, we also synthesize a small molecule quaterylene dye, QR-4PyC4 (Figure 18(b)). The design of QR-4PyC4 has several features: (1) the quaterylene structure offers intense NIR absorption; (Figure 18(a)) (2) high hydrophilicity due to charges; and (3) four positive charges for strong binding to mitochondria membrane. Recent studies have suggested that mitochondria increase in size and number in malignant cells [131]. Therefore, these features qualify QR-4PyC4 as a universal PA agent for cancer imaging without the need of targeting ligands.

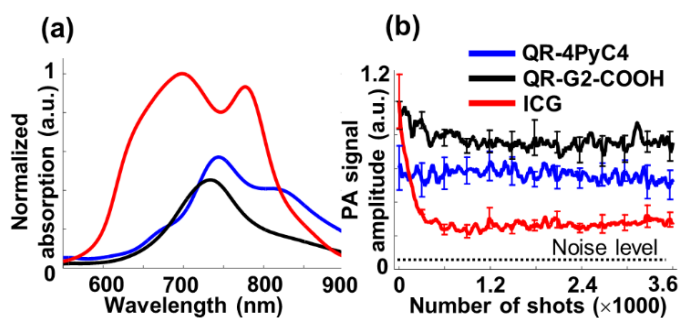


Figure 18. Optical characteristic and photoacoustic response of QR-4PyC4, QR-G2-COOH, and ICG dyes. (a) Absorption spectra of QR-4PyC4 (blue solid line), QR-G2-COOH (black solid line), and ICG (red solid line) in PBS solution at 10 μ M concentration. (b) Change of PA signal amplitude at 740 nm of QR-4PyC4 (blue solid line), QR-G2-COOH (black solid line), and ICG (red solid line) over 3,600 short-pulse laser exposures. Each data point represents an average over 5 measurements and error-bars are shown every 60 points.

As shown in table 2, QR-G2-COOH and QR-4PyC4 exhibits relatively intense absorption in the NIR region in PBS, although their molar extinction coefficients ($\epsilon=0.52$ and $0.66 \times 10^5 \text{ cm}^{-1} \text{ M}^{-1}$ for QR-G2-COOH and QR-4PyC4 in PBS respectively, as compared to $\epsilon=2.45 \times 10^5 \text{ cm}^{-1} \text{ M}^{-1}$ for ICG) are lower than that of ICG, which is likely ascribed to the significant aggregation of quaterylene rings at high concentration of $10 \mu\text{M}$. Importantly, both QR-G2-COOH and QR-4PyC4 are much less fluorescent than ICG at the same concentration (Figure 19, Table 2).

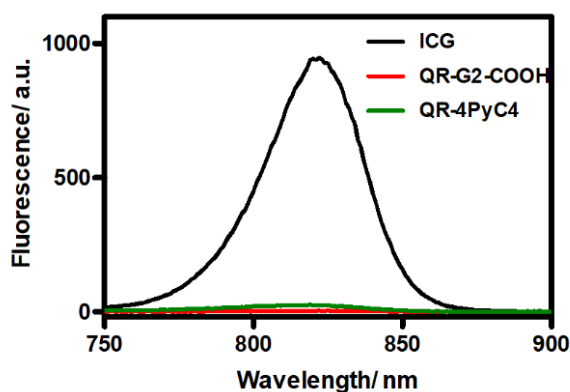


Figure 19. Fluorescence spectra of ICG, QR-G2-COOH and QR-4PyC4 at $10 \mu\text{M}$

As a result, the energy decay mechanism of ICG has two major contributions: non-radiative and radiative, whereas the excited QR-G2-COOH and QR-4PyC4 molecules mainly decay through non-radiative pathway, light to heat energy conversion that produces PA signal [128].

Table 2. The photophysical properties of ICG, QR-G2-COOH and QR-4PyC4 at $10 \mu\text{M}$ PBS solution.

	$\lambda_{\text{abs}}/\text{nm}$ ($\epsilon/10^5 \text{ cm}^{-1} \text{ M}^{-1}$)	$\lambda_{\text{em}}/\text{nm}$
QR-G2-COOH	734 (0.52)	--
QR-4PyC4	743 (0.66)	--
ICG	777 (1.08); 699 (1.15)	804

--: too weak to be detected.

4.3.2 Photostability evaluation

We first carried out photobleaching test in a polyethylene tube to evaluate the photostability of QR-4PyC4, QR-G2-COOH and ICG. PA signal amplitudes at 740 nm were measured from each dye over continuous 3,601 laser excitations of 22 mJ/cm² (Figure 18(b)). Normalized PA signal amplitudes of ICG, QR-G2-COOH, and QR-4PyC4 at the first laser excitation are 1.5, 1.2, and 0.6, respectively, among which the difference is expected from the absorption spectrum of those dyes (Figure 18(a)). After being exposed to continuous laser irradiation for 300 shots, however, PA signal amplitude of ICG dramatically decreases by 66.7% and corresponding SNR is changed from 37.4 dB to 27.8 dB, while PA signal amplitude of QR-4PyC4 and QR-G2-COOH only decreases by 13.1% and 4.7%, respectively, and corresponding SNR is changed from 33.0 dB to 31.8 dB and from 36.6 dB to 36.2 dB, respectively. After additional 3,300 shots, PA response of QR-4PyC4 becomes stable as a PA signal amplitude changes in only 1.1%, and corresponding SNR drops from 31.8 dB to 31.7 dB, while PA signal amplitude for QR-G2-COOH and ICG continually decreases by 13.7% and 16.1%, respectively, and corresponding SNR drops from 36.2 dB to 34.9 dB and from 27.8 dB to 26.3 dB, respectively. These results indicate that the developed dendrimer dyes, QR-4PyC4 and QR-G2-COOH, retaining with high photostability with competitive PA signal generation efficiency over a total of 3,601 laser shots

4.3.3 Cellular uptake and viability test

To demonstrate the high cellular uptake of QR-4PyC4, we compared uptake of QR-4PyC4, QR-G2-COOH and ICG in MDA-MB-231 cells. We observe as high as 13% cell uptake of QR-4PyC4 (3.2-fold higher than QR-G2-COOH), as compared to 4% for QR-G2-COOH and 1% for

ICG (Figure 20). As we discussed above, the four positive charges on QR-4PyC4 allows for strong binding to mitochondria membrane, therefore, high cellular uptake is expected. It's not surprising that QR-G2-COOH also shows higher uptake than ICG because it has been reported that nanostructures are prone to endocytosis by cells [132].

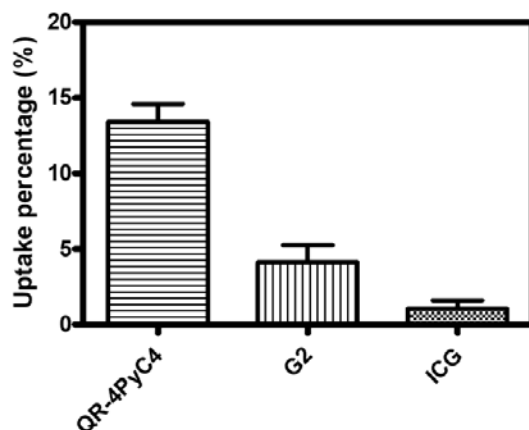


Figure 20. Cellular uptake percentage of QR-4PyC4, G2-QR-COOH, and ICG dyes.

As the following study, cell viability was evaluated after treating with QR-4PyC4 dye that has superior photostability and intracellular uptake characteristics. Our cytotoxicity study shown in Figure 21 suggests that most cells treating with QR-4PyC4 at the concentration of up to 10 μM can survive. Low cytotoxicity of QR-G2-COOH has been reported in the our previous study [46].

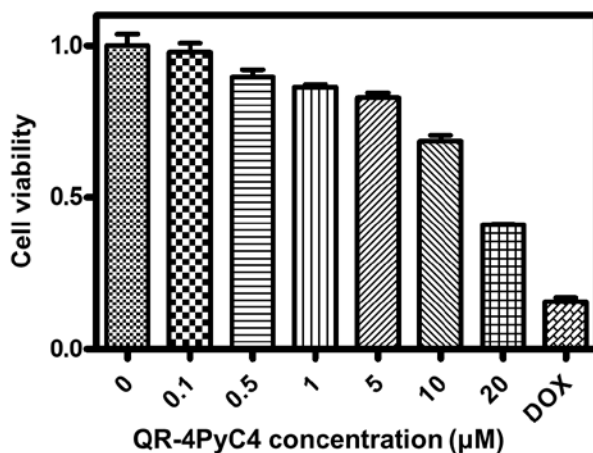


Figure 21. Cell viability of QR-4PyC4 in MDA-MB-231 cells. Cell medium (Dye concentration at 0 μM) was used as a negative control, non-toxic, and, Doxorubicin (DOX) was used as a positive control, toxic.

4.3.4 Photoacoustic imaging of MDA-MB-231 using QR-4PyC4, QR-G2-COOH, and ICG

In Figure 22, the PA signal intensity map (Figure 22(b)) is compared with the cell distribution shown in the wide-view bright field microscopy image (Figure 22(a)) that is stitched from individual microscopy images. Green dots that indicate each cell locations in microscopy image (Figure 22(a)) are overlaid on PA image (Figure 22(b)) for presentation purpose of comparison. While the cells could not be individually identified in PA image due to the limited spatial resolution of the ultrasound transducer (Theoretical beam diameter: $167\text{ }\mu\text{m}$ @ -6 dB bandwidth), PA signal amplitude would be expected to be proportional to cell distribution within the focal region of ultrasound transducer and it is well shown in Figure 22.

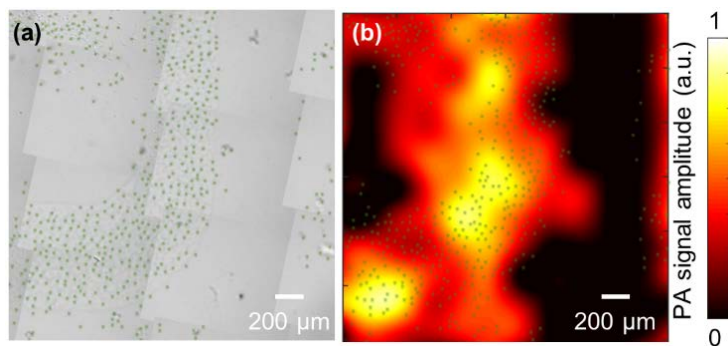


Figure 22. (a) Optical microscopy image (10x) and (b) Photoacoustic image of MDA-MB-231 cells with QR-4PyC4 dye overlaid on microscopy image. Cells are marked as green spots. PA signal intensity is directly proportional to cell confluence.

In order to evaluate the photostability of the dye, three PA images were sequentially acquired from MDA-MB-231 cells treated with QR-4PyC4, QR-G2-COOH, and ICG as depicted in Figure 23.

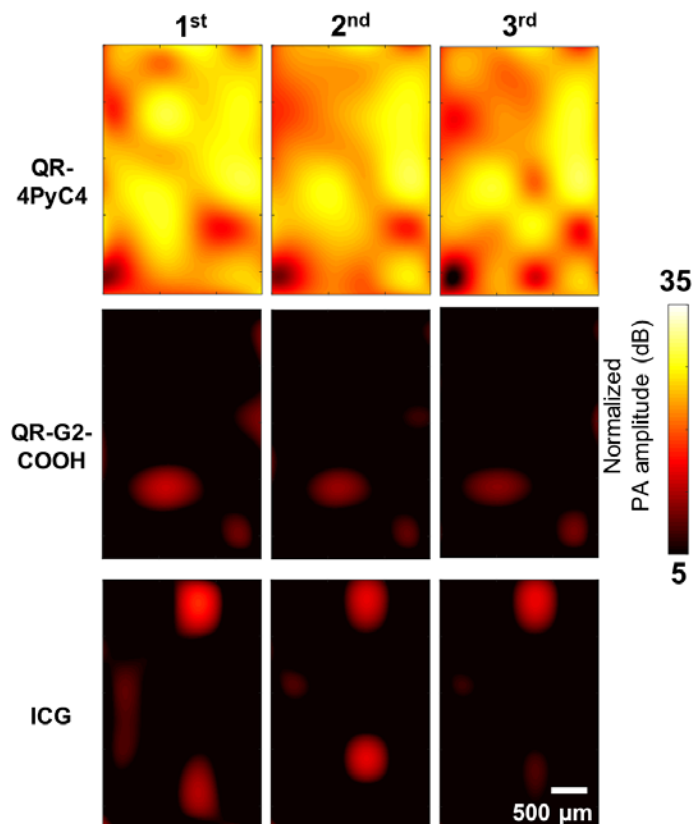


Figure 23. Photoacoustic image of MDA-MB-231 cells stained with QR-4PyC4, QR-G2-COOH, and ICG. Images in each column are subsequently acquired.

Averaged PA signal amplitude on each image was shown in Figure 24. Interestingly, PA signal amplitude averaged on the ROI from QR-4PyC4 dye shows higher amplitude (30.0 ± 0.7 dB) than signal amplitudes from the other two dyes (QR-G2-COOH: 8.6 ± 3.4 dB, ICG: 11.1 ± 3.5 dB) at the 1st scanning. PA signal from QR-G2-COOH shows the lowest value in the cell study although absorption coefficient and PA signal amplitude of QR-G2-COOH shows the highest values in vitro. This is mainly attributed to lower cell uptake efficiency of QR-G2-COOH dyes compared to QR-4PyC4 dye due to its large molecular structure. Reflecting the signal drop by photobleaching, averaged PA signal amplitude decreases by 5.6% (from 30.0 ± 0.7 dB to 29.5 ± 1.1 dB) for QR-4PyC4, 16.1% (from 8.6 ± 3.4 dB to 7.1 ± 3.2 dB) for QR-G2-COOH, and 17.7% (from 11.1 ± 3.5 dB to 8.4 ± 6.0 dB) for ICG between 1st and 2nd scanning. In the following 3rd scanning,

PA signal from QR-4PyC4 and QR-G2-COOH does not decrease as much as initial signal drop by only 0% (from 29.5 ± 1.1 dB to 29.5 ± 1.3 dB) and 1.1% (from 7.1 ± 3.2 dB to 7.0 ± 3.3 dB), respectively, but PA signal from ICG continue to decrease by 12.9% (from 8.4 ± 6.0 dB to 7.2 ± 5.0 dB). Looking at the entire scanning period, averaged PA signal amplitude decreases by 5.6% (from 30.0 ± 0.7 dB to 29.5 ± 1.3 dB) and 16.8% (from 8.6 ± 3.4 dB to 7.0 ± 3.3 dB) for QR-G2-COOH, and 36.2% (from 11.1 ± 3.5 dB to 7.2 ± 5.0 dB) for ICG, between the 1st scanning and 3rd scanning. In summary, while PA signal from ICG continually decreases as scanning trial increases, PA signals from QR-4PyC4 and QR-G2-COOH dyes retains stable level after a decrease during the initial scanning.

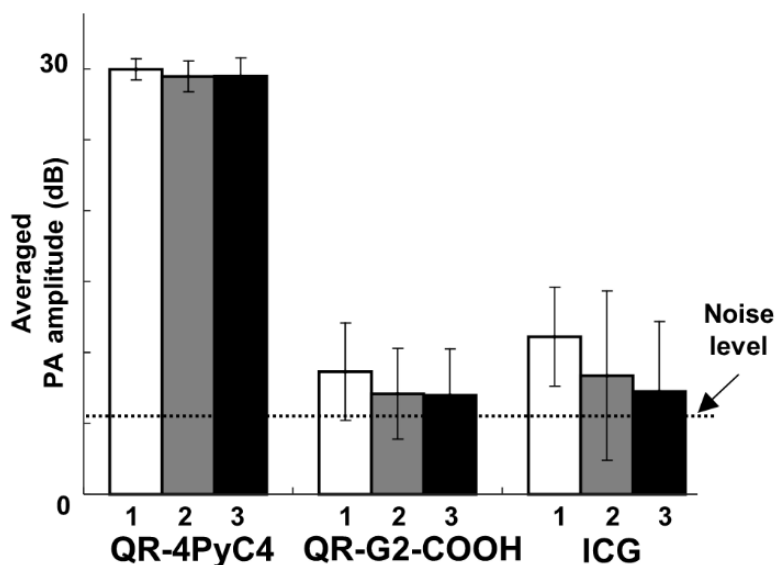


Figure 24. Averaged PA signal amplitudes of MDA-MB-231 cells stained with QR-4PyC4, QR-G2-COOH, and ICG.

These overall trends shown in Figure 24. are well-matched with in vitro photostability measurement shown in Figure 18(b). Note that the cells were exposed to the laser light in multiple times during each raster scan due to the laser beam (3 mm in radius, 28.3 mm^2 in area) is bigger than the scanning step size of $400 \text{ }\mu\text{m}$. All these results suggest that QR-4PyC4 could be potentially

used for long-term PA monitoring of the biological activities due to its high photostability and cell uptake efficiency. After modification with some special moieties, such as ligand and drug, QR-G2-COOH could also be utilized for long-term PA monitoring, thus permitting the application of different imaging modalities and therapeutic strategy. Due to lack of the efficient laser exposure system for several days continuously, this study is limited to evaluate their photostability by using only short and strong laser pulses within limited time. However, we have expected that the quaterylene dyes keeps its photostability against more light exposures over several days. Based on our experience, these dyes can be stored under the room light for several months without significant loss of PA imaging capability. In future work, the photostability of our developed quaterylene structure dyes will be quantitatively evaluated day-by-day to extend the timeline limitation of this study with more systemic designed experimental system

4.4 CONCLUSION

Both QR-4PyC4 and QR-G2-COOH show significantly high photostability as compared to ICG, which makes them strong candidates of reliable PA agents for a long-term imaging. While overall PA signal intensity from QR-G2-COOH is higher, cell uptake rate of QR-4PyC4 is found superior to QR-G2-COOH and ICG. Due to the superior photostability, cell uptake, and cell viability, this study suggests that QR-4PyC4 is a promising candidate as a universal, sensitive, and reliable PA agent and QR-G2-COOH has potential as a nano-system with its high structural flexibility for PA imaging.

4.5 ACKNOWLEDGEMENTS

This work was supported by the NIH Grant # R21CA174541 (PI: Bai).

5.0 SUPER-RESOLUTION ULTRASOUND IMAGING WITH HIGH TEMPORAL RESOLUTION: *IN VIVO* FEASIBILITY ON VASA VASORUM IN ATHEROSCLEROSIS RABBIT MODEL

The work presented in this chapter was reprinted, with permission, from J.Yu, L. Lavery and K. Kim, “Super-resolution ultrasound imaging with high temporal resolution: In vivo feasibility on vasa vasorum in atherosclerosis rabbit model” that was submitted and under reviewed.

Traditional ultrasound imaging techniques are limited in spatial resolution to visualize angiogenic vasa vasorum that is considered as an important marker for atherosclerotic plaque progression and vulnerability. The recently introduced super-resolution imaging technique based on microbubble center localization has shown potential to achieve unprecedented high spatial resolution beyond acoustic diffraction limit. However, a major drawback of the current super-resolution imaging approach is low temporal resolution because it requires a large number of imaging frames. In this study, a new imaging sequence and signal processing approach for super-resolution ultrasound imaging are presented to improve temporal resolution by employing deconvolution and spatio-temporal-interframe-correlation based data acquisition. *In vivo* feasibility of the developed technology is demonstrated and evaluated on vasa vasorum in the rabbit atherosclerosis model. The proposed method not only identifies a tiny vessel with diameter of 41 μm , 5 times higher spatial resolution than the acoustic diffraction limit at 7.7 MHz, but also significantly improves temporal resolution that allows for imaging vessels over cardiac motion.

5.1 INTRODUCTION

Acute coronary syndromes (ACS), a leading cause of morbidity and mortality in the US and Europe, is generally caused by the plaque rupture or erosion [133]–[136]. Extensive efforts to characterize and predict vulnerable plaques assessing a few known markers have been made for several decades [133]–[139]. It has been found that abnormally dense neovascularization of the vessel wall, often infiltrating into the plaque core, is associated with development of atherosclerotic plaque and progression of the disease [136], [140]. These micro-vasculatures may lead to intraplaque hemorrhage, which typically accompanies unstable plaque [136], [140], [141]. Therefore, abnormal proliferation of adventitial vasa vasorum (VV) is an important clinical imaging target to assess vulnerability of the atherosclerotic plaques [136]–[140], [142]. However, the lack of adequate noninvasive and high-resolution imaging technology to visualize VV is a big challenge. Micro-CT, optical coherent tomography (OCT) and contrast enhanced ultrasound (CEU) imaging have been demonstrated to image VV in pre-clinical studies, but these technologies have suffered from hazardous radiation (micro-CT), poor imaging depth (OCT), and insufficient spatial resolution (CEU) [137], [138], [143]–[145].

CEU is one of well-established imaging modalities to evaluate microvasculature *in vivo* animal study using gas-filled microbubbles that can provide high echogenic contrast [138], [145], [146]. In previous studies with CEU using a mid-frequency linear array transducer (Transmit at 7 MHz and receive at 15 MHz), they have shown the correlation of adventitial VV density based on ultrasonic image intensity with VV progression [138], [145], [146]. However, identifying VV, especially those near the lumen of the main vessel, at mid-frequency was limited mainly due to low spatial resolution [138]. Because of this limitation with spatial resolution, accuracy of VV density measure therefore was limited. High spatial resolution is essential for separating individual

tiny VV from the lumen of the main vessel to improve accuracy of adventitial VV density as an indicator of VV progression. A high-frequency ultrasound transducer that can provide spatial resolution of 35-40 μm at center frequency higher than 30 MHz might be able to identify VV *in vivo*, but it is preferably utilized in intravenous approach due to its limited imaging depth less than 2 cm. This approach is not ideal if considering eventual translation with full noninvasiveness. Therefore, transcutaneous imaging approach using a mid-frequency transducer commonly used in clinic would be sought after.

Super-resolution US imaging technology has been recently introduced to overcome the limitation of inherent spatial resolution of US imaging defined by the acoustic diffraction limit [51], [52]. This approach utilizes two state-of-the-art technologies; tissue rejection and microbubbles localization technique [51], [54], [56], [147]. It is known that ultrafast plane wave imaging in general significantly improves the performance of the eigen decomposition based adaptive clutter filtering technique, outperforming in suppressing stationary signal that comes from the clutter component, compared to conventional clutter filtering techniques used in typical Doppler imaging[56]. Moreover, microbubble center localization technique allows to estimate each location of microbubbles in sub-pixel level precision [51], [54], [147]. Each microbubble could be considered as a point source because its size ($\sim 3 \mu\text{m}$) is much smaller than the spatial resolution of the imaging system that operates at mid-frequency ultrasound of around 5 - 10 MHz (100~200 μm). Therefore, received echo signal from individual microbubble would be represented as a point spread function (PSF) of the imaging system, and each microbubble is expected to be located at the centroid of the PSF. After summing up localized microbubbles in blood flow over a large number of frames, a vascular network image in high spatial resolution beyond the acoustic diffraction limit can be formed. Errico et al., successfully reconstructed single static super-resolved

image of rat brain vasculature network, identifying the micro-vessel in diameter as small as 9 μm full-width at half-maximum (FWHM) with using a 20 MHz linear array transducer [51]. However, the major drawback of this method requires a long data acquisition time of 150 seconds for a total of 75,000 frames at 500 frames per second. Requiring a long data acquisition time makes this imaging technology susceptible to target motion and therefore hinders widespread of this technology for various applications.

Here, we present a new approach of super-resolution US imaging technology to achieve a high temporal resolution as well. A strategically designed approach in two steps is employed to drastically improve temporal resolution; 1) deconvolution localization technique to reduce data acquisition time, and 2) spatio-temporal-interframe-correlation (STIC) based data acquisition to compensate motion over reduced data acquisition time. First, applying deconvolution separates each center of microbubbles from densely grouped microbubbles while previous approach, 2D Gaussian fitting, typically requires discarding such frames in which clumped microbubbles cannot be separated. Therefore, deconvolution technique can significantly reduce data acquisition time. However, reduced data acquisition time using deconvolution only is not short enough to ignore fast physiologic motion such as cardiac-dependent motion. In addition to deconvolution technique, therefore, STIC data acquisition inspired from 3D fetal echo-cardiology imaging technique is adapted to further overcome fast physiologic motion [148]. STIC acquisition allows it to synchronize collected images over multiple cardiac cycles. *In vivo* feasibility of the developed technique in identifying VV is demonstrated in rabbit atherosclerotic plaque model.

5.2 MATERIALS AND METHODS

5.2.1 Deconvolution-based super-resolution US imaging sequence

Super-resolution imaging sequence was implemented into a fully-programmable ultrasound scanner (Vantage 128, Verasonics, Kirkland, WA, USA) equipped with a high frequency hockey stick linear array transducer centered at 8.8 MHz (CL15-7, ATL-Philips, Bothell, WA).

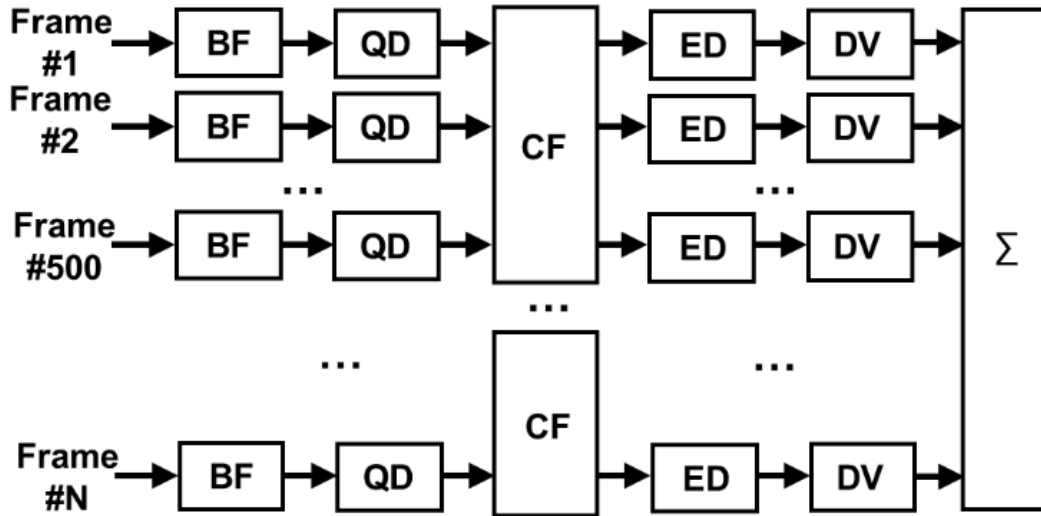


Figure 25. Block diagram for signal processing of super-resolution ultrasound imaging. BF: Delay-and-sum beamformer; QD: Quadrature demodulator; CF: Eigen-based spatio-temporal clutter filter; ED: Envelope detector; DV: Deconvolution with the system PSF; Σ : Integrator with STIC data alignment based on estimated cardiac pulsation.

Ultrasound plane waves were insonified to the target with high pulse repetition frequency (PRF) of 1,500 Hz with three different steering angles (-3° , 0° , 3°) for compounding, therefore the effective PRF is 500 Hz. Signal processing algorithm was illustrated in Figure 25. Acquired raw radio-frequency (RF) channel data were beamformed by delay-and-sum algorithm, and then

downmixed to the baseband using a quadrature demodulator. The echo signal from microbubbles were extracted from compounded analytic baseband signal of 500 frames by using a spatio-temporal eigen-based decomposition clutter filter[56], [149], [150]. Envelope of the echo signal from microbubbles was interpolated for an increased pixel resolution of $15 \mu\text{m}$ (lateral) \times $10 \mu\text{m}$ (axial) and deconvolved with the measured system PSF to localize each microbubble. Richardson-Lucy (RL) deconvolution is a non-linear iterative deconvolution method that has been widely used for deblurring image with the presence of Poisson distributed noise in astronomy and biomedical applications[57], [151]–[153]. The iterative process is described by

$$i^{(k+1)} = i^{(k)} \left(h * \frac{g}{h \otimes i^{(k)}} \right)$$

where, $*$ is the correlation operator, \otimes is the convolution operator, $i^{(k)}$ is the estimated image after k iterations, h is the PSF of the imaging system and g is blurred image modeled by $g = h \otimes i^{(0)} + \text{noise}$ [153]. The concept of this approach is illustrated in Figure 26.

The echo signal received by the imaging system (Figure 26(c)) is represented by convolving the PSF of the imaging system (Figure 26(a)) with two point targets (Figure 26(b)). Figure 26(c, e) shows the received signal (indicated by ‘Overall’) from two targets separated by $70 \mu\text{m}$, smaller than the spatial resolution of the system. With using deconvolution (#s of iteration = 100), however, this signal can be separated into two different targets as shown in Figure 26(d, f). A potential problem with the RL deconvolution algorithm is noise amplification, which is known to be generic for all maximum likelihood techniques. Therefore, any false target can be expected when signal-to-noise ratio is not high enough due to noise-sensitive RL deconvolution. For example, in Figure 26(e, f) deconvolving the received signal from two targets with significant Gaussian white noise resulted in imperfect target locations. This high sensitivity to noise can be

alleviated with several available standard regulation approaches. In this study, thresholding at -10 dB was applied to pre-deconvolved signal to suppress noise component.

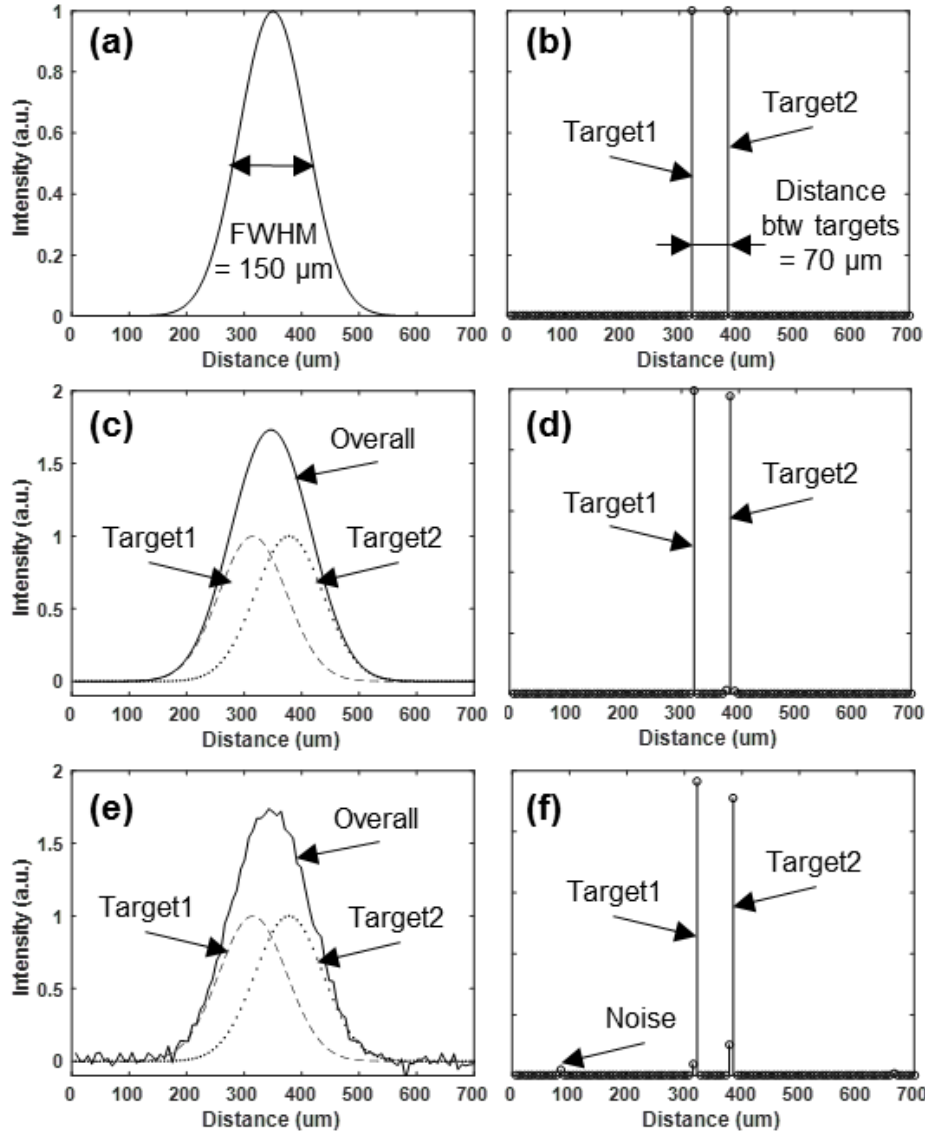


Figure 26. Conceptual demonstration of sub-wavelength localization using deconvolution on synthetic data. (a) PSF of imaging system. FWHM is assumed as $150\ \mu\text{m}$. (b) The locations of the two neighboring targets. Two targets are positioned $70\ \mu\text{m}$ apart. (c) Synthetic signal received from two targets is shown in (b) using the imaging system with PSF shown in (a). Two targets cannot be separated in the image due to their distance is shorter than the spatial resolution of imaging system. (d) Deconvolution results of received signal shown in (c) using the system PSF shown in (a). Two targets are distinctly identified. (e) Synthetic signal received from two targets when noise is added is shown in (b) using the same imaging system. (f) Deconvolution results of (e), where two targets are clearly identified with minimal interference due to noise

5.2.2 Spatio-Temporal-Interframe-Correlation (STIC) based data re-alignment algorithm

STIC data re-alignment algorithm that synchronizes among collected cardiac cycles based on estimated cardiac pulsation is developed to monitor fast physiological event under limited imaging speed. To capture rapid physiological dynamics at a limited frame rate, sequentially acquired RF data over multiple cardiac cycles can be synchronized based on the cardiac cycle period estimated from the periodically changing signal intensity, which reflects the number of microbubbles. Rigid motion in frame-by-frame caused by respiratory or operator dependent motion was compensated by applying an offset to match acquired images. Offset was estimated by taking 2-dimensional cross-correlation between frames. If correlation coefficient between images is smaller than 0.9, the image can be excluded. The eigen-based spatio-temporal tissue rejection filter technically removes all stationary tissue information except for moving objects, such as microbubbles. At diastolic phase, microbubbles are less likely flow, therefore smaller number of moving microbubbles are detected. On the contrary, the number of detected microbubbles significantly increases as microbubbles are moving fast toward the systole. Low-pass filter is applied to the detected signal from flowing microbubbles to estimate the cardiac period. Figure 27 illustrates an example of the number of detected microbubbles as a function of time (blue solid line) over 2 seconds totaling 1,000 data points. The reference frame for synchronization (red solid line) was chosen at the minima after low pass filtering. The estimated period of 5 Hz by this approach has good agreement with the heart rate recorded by electrocardiogram of 290-310 beats per minute.

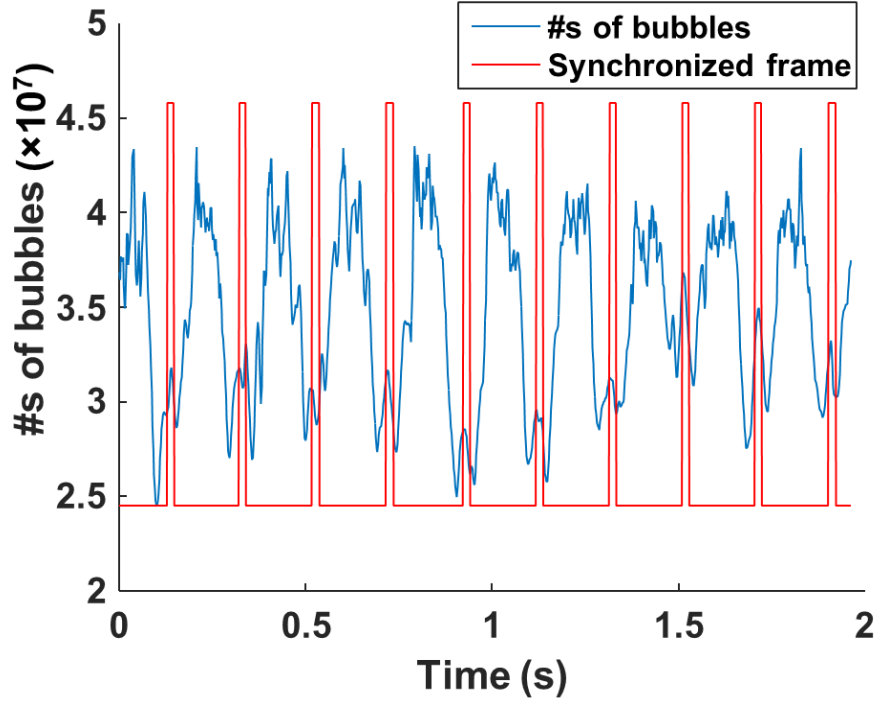


Figure 27. Estimated cardiac pulsation by counting the numbers of flowing microbubbles (blue solid line). After applying low-pass-filtering, the frames with minimum value are chosen as reference frames for synchronization (red solid line)

Figure 28 shows overall graphical diagram of STIC acquisition method. First, we collected raw ultrasound RF data sequentially over multiple cardiac cycles. Acquired US frames are synchronously aligned based on cardiac period estimated by the numbers of microbubbles. Re-aligned images are integrated to form a super-resolution image of single cardiac cycle. In this study, we collected continuous 3,000 frames over 6 seconds, which is equivalent to approximately 15-30 cardiac cycles. Each cardiac cycle was divided by 10 sections and entire dataset was aligned based on section number. Aligned frames in each section were summed to reconstruct single super-resolution frame. Therefore, single cardiac cycle containing 10 reconstructed frames with super-resolution was generated and each super-resolution image contains around 300 acquired frames collected over multiple cardiac cycles.

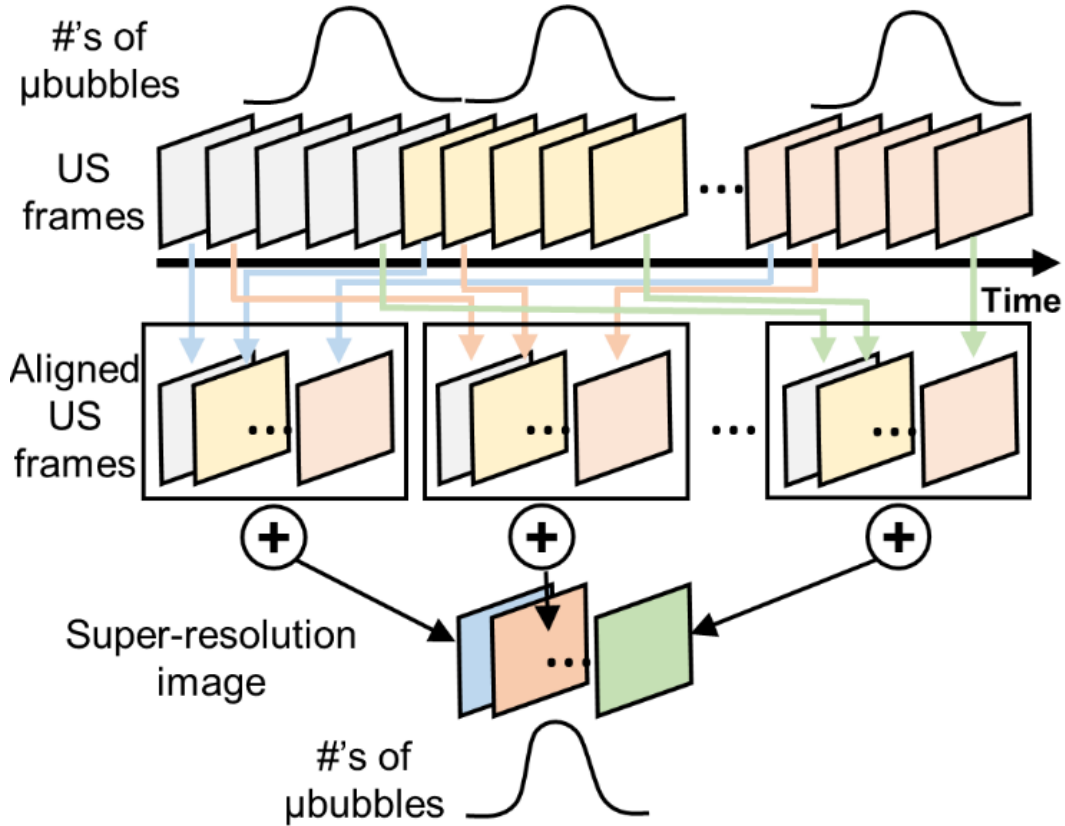


Figure 28. Graphical diagram of STIC data acquisition. Sequentially acquired multiple datasets are synchronized to form single cardiac cycle event based on the cardiac pulsation estimated by the numbers of bubbles.

5.2.3 Rabbit atherosclerotic plaque model

A New Zealand white rabbit (3.5 kg) was fed a high fat and cholesterol diet (cholesterol 1%, peanut oil 2.5%, and fat 10%) over 6 weeks to accelerate development of atherosclerosis[138]. Balloon injuries were induced to the superficial femoral artery on the right side of an anaesthetized rabbit (ketamine 150 mg IM, xylazine 8 mg IM and 2.5% inhaled isoflurane) by using a 2F Fogarty balloon catheter (Edwards Life Sciences, CA, USA) one-week after feeding. The balloon inflated at 2 atm was moved back and forth several times to apply injury to the vessel walls around bifurcation area under guidance of high-frequency ultrasound scanning (Vevo2100 equipped with

a linear array transducer centered at 18.5 MHz, FUJIFILM Visualsonics, Toronto, On, Canada). Upon completion of imaging, blood of 5 mL was obtained to measure cholesterol concentration.

5.2.4 Ultrasound imaging protocol

At twelve weeks after surgery, ultrasound imaging were performed injecting a commercial microbubbles (Definity, Lantheus Medical Imaging, N. Billerica, MA). A 0.2 mL microbubbles bolus was intravenously administrated through an ear vein access catheter for each imaging session. An anaesthetized rabbit (same protocol of surgery) was prepared with hair-shaved legs (Figure 29). US gel was applied for ultrasonically coupling. Super-resolution US imaging sequence was performed to the surgical side and thereafter contralateral side by using a fully programmable research ultrasound scanner (Vantage 128, Verasonics, Kirkland, WI) equipped with a hockey stick linear array transducer (CL15-7, ATL-Philips, Bothell, WA). A transducer holder was used to fix the transducer. Compounded plane wave images with 3 different angles of total 9,600 frames were acquired in each data acquisition. To verify repeatability, total three datasets were collected on the possibly same imaging plane. All signal processing was performed offline using MATLAB software (Mathworks, Natick, MA). Harmonic MIP imaging was sequentially conducted on the same location by using a commercial ultrasound imaging equipped with a linear array transducer (Acuson Sequoia 512 with 15L8, SIEMENS, Mountain view, CA). To quantify degree of vasa vasorum development, vessel density was calculated by

$$Vasa\ Vasorum\ density = \frac{signal\ intensity\ on\ adventitia\ area}{adventitia\ area}$$

where, adventitia area was manually selected on the B-mode. Above *in vivo* surgery and imaging protocols of rabbit were approved by Institutional Animal Care and Use Committee (IACUC) of University of Pittsburgh.

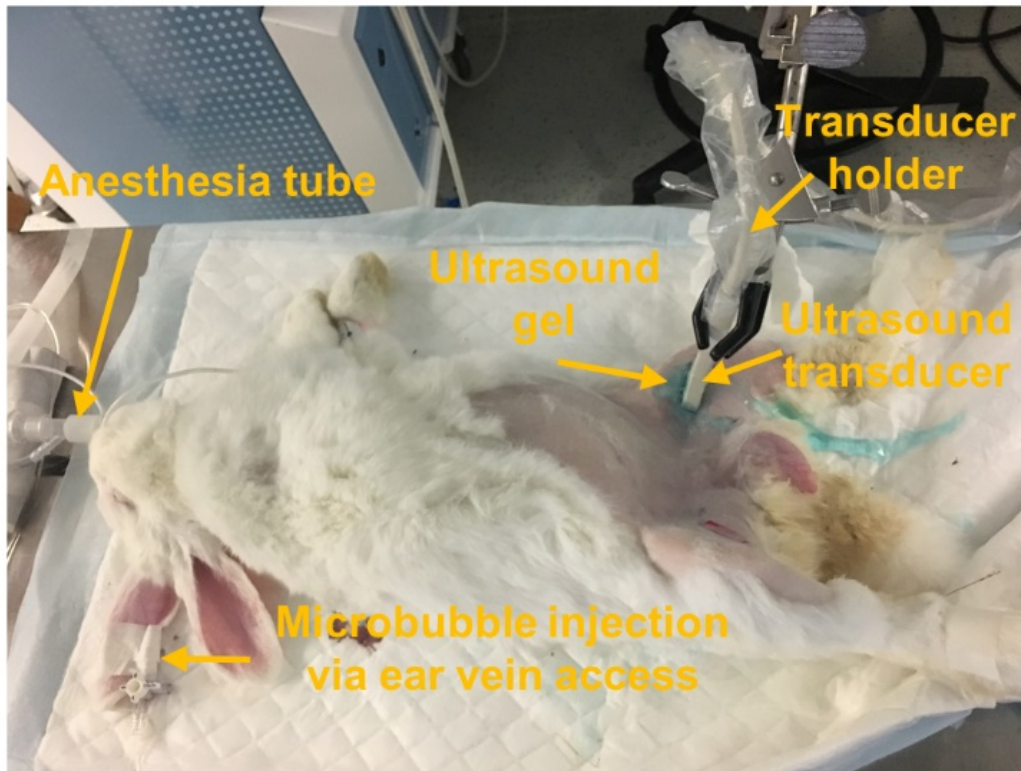


Figure 29. Experiment setup of rabbit imaging. Microbubbles were injected via ear vein access. A hockey stick linear array ultrasound transducer was used for imaging. Transducer holder is used to remove operator-dependent motion in this study

5.2.5 Histology and Immunofluorescence

Femoral arteries were perfusion fixed using paraformaldehyde, and then carefully excised along with a block of the surrounding muscle to save neighbor vasculature in the connective tissues. Excised tissues were then carefully fixed in 4% paraformaldehyde, embedded in the paraffin-block and serially sectioned. Cross-sections of the paraffin block were stained with

hematoxylin and eosin (H&E) and Von Willebrand Factor (vWF) for endothelium staining. In briefly, for antigen retrieval, treatment dewaxed slides were heated in sodium citrate buffer (pH 6.0, abcam, Cambridge, MA) at 95°C for 30min in blocking solution of goat serum and incubated with the anti-vWF antibody (Millipore, Burlington, MA) at 4°C overnight. Incubated slides were washed with PBS 3 times for 3 mins. The slides were incubated with Cy3-conjugated IgG (Jackson ImmunoResearch Laboratories, West Grove, PA) and counterstained with DAPI. The stained slides were observed by using a fluorescent microscope (IX-81, Olympus, Center Valley, PA). Brightness (+20%) and contrast (-20%) of acquired fluorescence images were adjusted to improve visibility by using ImageJ software [154].

5.3 RESULTS AND DISCUSSIONS

5.3.1 Deconvolution based super-resolution ultrasound imaging

In Figure 30, our developed imaging technique on a rabbit femoral artery is compared with conventional imaging technologies. The white rectangle represents the balloon injured area that is expected to develop the plaque with VV, and white arrows in all images indicate a big branch near the femoral artery that is used as the landmark to match the image plane among different modalities. Cadence^{TR} harmonic contrast-enhanced imaging technique with using microbubbles operated by a commercial ultrasound scanner (Accuson Sequoia 512, SIEMENS, Mountain view, CA) shown in Figure 30(a) is a typical standard method in the clinic to evaluate microvasculature perfusion[138], [145], [155], [156]. However, this technique is limited in spatial resolution to identify and separate VV from the major vessel such as the femoral artery in this study.

Conventional B-mode image shown in Figure 30(b) only illustrates structural information of bifurcation area of the rabbit femoral artery and small vasculatures surrounding the femoral artery cannot be identified due to limited spatial resolution. To amplify signal from the blood, power Doppler based temporal maximum intensity persistence (MIP) imaging technique (#'s of frames = 2,000) implemented in Verasonics system is used as shown in Figure 30(c).

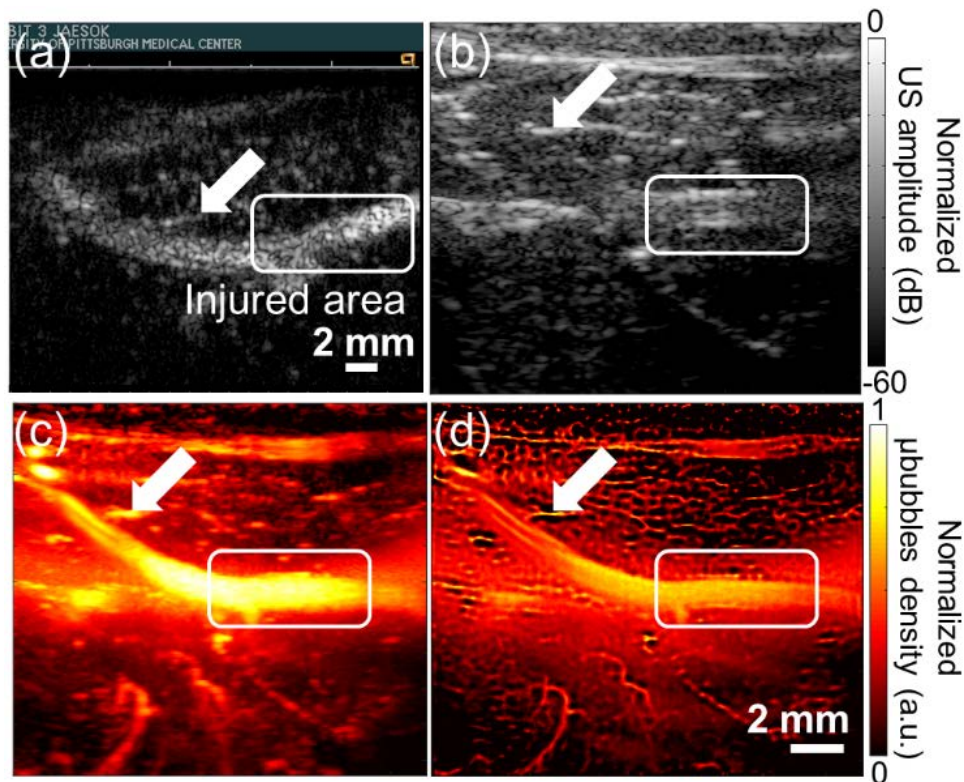


Figure 30. Comparison of several imaging modalities. (a) CadenceTR contrast enhanced imaging with microbubbles acquired by commercial ultrasound scanner (Sequoia 512, Siemens), (b) conventional B-mode imaging, (c) temporal MIP vascular imaging, (d) proposed super resolution imaging of ROI. Same raw data is used to reconstruct images (b-d). White rectangle represents balloon injured area that the plaque is expected to be developed. White arrow indicates the same vessel branch that shows correlation of images acquired by two different ultrasound scanners.

This method employs a tissue-rejection filter that suppresses stationary signal from tissue and extracts only signal from flowing microbubbles. However, its spatial resolution is still insufficient to clearly identify individual VV. The proposed super-resolution ultrasound imaging method implemented in Verasonics system shown in Figure 30(d) delineates detail of microvasculature

that is shown blurred in other imaging methods due to low spatial resolution that is mainly limited by diffraction limit of the operating frequency.

To estimate maximum spatial resolution of our developed method, one of the finest vessels is chosen among discernable vasculatures in the Figure 31(a) (Selected region of Figure 30(d)). FWHM on lateral axis of the selected vessel is estimated to be 41 micron that is 5-fold smaller than wavelength as shown in Figure 31(b).

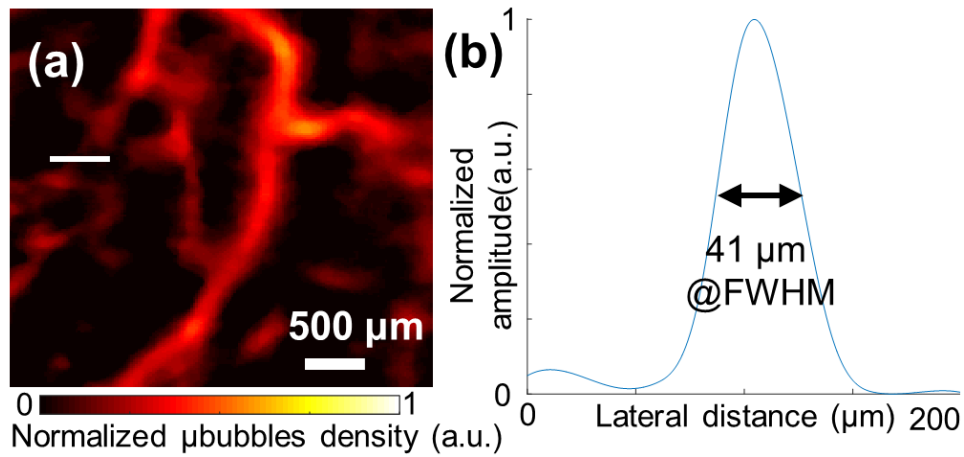


Figure 31. Spatial resolution of proposed imaging method. (a) One of the finest vessels is chosen (white solid line) in the ROI, (b) Spatial profile of selected vessel. FWHM is estimated by 41 μm ($<\lambda/5$).

Three sequential data-set are independently acquired using our super-resolution imaging sequence to verify repeatability of our proposed method. For three independent imaging sessions, bifurcation of femoral artery and the branched vessel indicated in white arrow in Figure 30 are identified as landmark to maintain the same imaging plane. Figure 32(a) depicts temporal MIP vascular imaging using the first data set of 2,000 frames, and Figure 32(b-d) represents reconstructed images from sequentially acquired the first, second and third data set (2,000 frames for each acquisition), respectively using our super-resolution imaging sequence. Note that Figure 32(a) and (b) are reconstructed from same raw dataset. An obviously same major vessel is observed

at the center in all three reconstructed images to assure the same imaging plane among three imaging sessions. Some microvasculature in the background shown slightly different can be attributed to tilted imaging plane within three different imaging sessions.

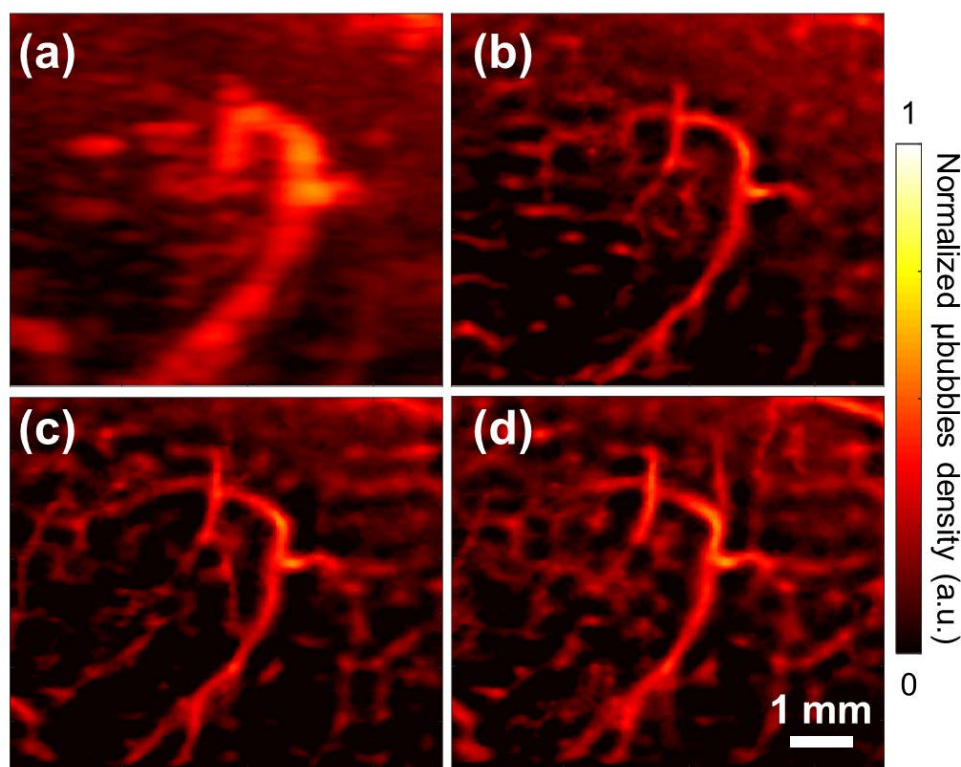


Figure 32. Repeatability of proposed method. (a) temporal MIP vascular network imaging using eigen-decomposition method. (b-d) Super-resolution images using sequentially acquired three datasets (2,000 frames per each image) from same region of interest.

5.3.2 *In vivo* feasibility of the developed super-resolution technique in imaging vasa vasorum on a rabbit femoral artery

Conventional B-mode imaging and super resolution imaging for vascular network of both side femoral artery, injured (experimental side) and contralateral non-injured side (control side),

are shown in Figure 33. In B-mode images (Figure 33(a, d)), adventitia area is represented in the yellow dotted line. Figure 33(b, c, e, f) show super-resolution images at diastole and systole on injured and the non-injured side, respectively. Each image at different stage of cardiac cycle is reconstructed from around 300 frames synchronized by STIC algorithm.

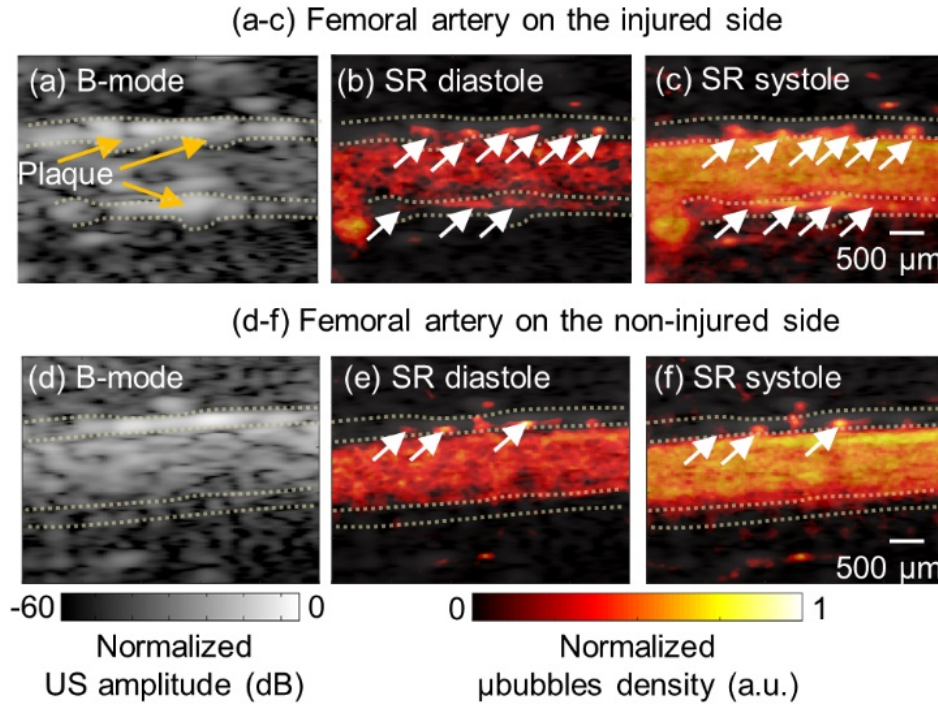


Figure 33. B-mode image (a, d) and corresponding super-resolution perfusion image overlaid on the B-mode image at diastole (b, e) and systole state (c, f). Top panel images are acquired from the injured side and bottom panel images are acquired from the non-injured side. Significant plaques are shown in the B-mode image on the injured side. Yellow dotted line represents adventitia region and white arrows indicate vasa vasorum in the adventitia

The abundance of VV in adventitia indicated by white arrows can be clearly observed on the injured-side in the super-resolution ultrasound imaging. Normalized VV density on the injured-side is 0.027 ± 0.004 , which is approximately 3 times greater than non-injured side with 0.010 ± 0.001 . Furthermore, apparent uneven surface on the vessel wall on the injured side is observed most likely due to plaque formation on the lumen wall. The vessel wall is overall thickened (injured: $410 \mu\text{m}$ vs non-injured: $220 \mu\text{m}$) and the lumen diameter is decreased (injured:

1.1 mm vs non-injured: 1.4 mm) in injured side. These observations are more clearly confirmed by closely looking at blood flowing through VV from adventitia into media.

VVs are more populated and believed to be infiltrated into the medial area of injured area, while less populated VV are found only in adventitial and connective tissue area in non-injured area. Atherosclerotic plaque formation and corresponding VV development is evidenced by histology of femoral artery section shown in Figure 34. The atherosclerotic lesions are characterized on injured side by neointimal proliferation, shown in Figure 34(b) by hematoxylin and eosin (H&E) stain and abnormally enriched VV development on adventitia, shown in Figure 34(d) by immunofluorescence of von Willebrand Factor (vWF) stain. Pink solid line in Figure 34(b) was drawn along endothelium in the tunica intima of the lumen. Total cholesterol level is measured 291 mg/dL that is approximately 3 times higher than standard range (< 100 mg/dL) due to feeding high-fat diet.

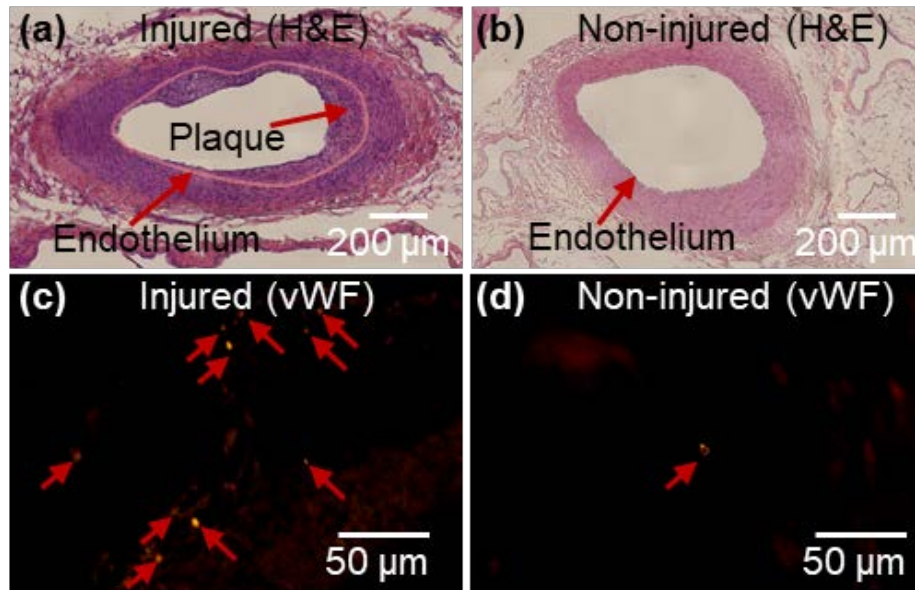


Figure 34. Haematoxylin and eosin stained vessel on the injured side (a) and non-injured side (b). Thirty images acquired at $\times 40$ magnification are stitched to reconstruct overall image of the vessel for (a) and (b). Significant plaque development is found in injured side (a). Vasa vasorum on adventitia in selected region was stained by anti-von Willebrand factor. A large number of vasa vasorum are found in adventitia on the injured side (c), but a few vasa vasorum are found in adventitia on the non-injured side (d).

5.4 CONCLUSION

It has been shown that super-resolution ultrasound imaging technique has strong potential to extend the application of ultrasound imaging with unprecedented high spatial resolution [51], [52], [59], [157]. We further developed this imaging technology to overcome the limitation of the temporal resolution, which makes it capable of imaging of fast event. Our proposed super-resolution imaging method successfully assesses VV density on the plaque in a rabbit femoral artery with enhanced temporal resolution as well as high spatial resolution. In our approach, deconvolution and STIC data acquisition were investigated to improve temporal resolution of US sub-diffraction imaging. It should be noted that deconvolution technique is known to be sensitive to noise as discussed in method section. Thresholding used in this study can successfully suppress noise, however it potentially also suppresses true signal when signal-to-noise ratio is relatively low for example in a fast plane-wave imaging. Therefore, more advanced adaptive noise reduction approach needs to be sought after to maximize signal-to-noise ratio while maintaining high temporal resolution in the future study. In addition, STIC data acquisition is generally used to collect and synchronize 3D data acquired from fast-moving fetal heart when using a relatively slow acquisition speed. It should be noted that there is an assumption in STIC acquisition; cardiac pulsation pattern over data acquisition period is stationary. With reduced total number of frames thanks to deconvolution, we were able to generate ten super-resolution images using 3,000 acquired frames that can be collected within 6 seconds. Therefore, our approach has potential for free-hand scanning in the clinics because the acquisition time is significantly shorter than free-hand data acquisition time of 3D-fetal echocardiography when using STIC acquisition in the standard clinical protocol that takes around 4 ~ 5 minutes on average[148], [158].

Since this study is concentrated on the technical development and *in vivo* feasibility demonstration, it is not intended to investigate any correlation between VV development and plaque stage with enough statistics, although this well-established rabbit model has been studied for a long time for various diseases in association with atherosclerotic plaques. Further extended study with an increased number of rabbits and time points is planned in the following study. In addition, the histology is limited for providing anatomically matched cross sections as a gold standard. An established anatomical imaging modality with high spatial resolution is necessary as a gold standard to provide more direct comparison, for example, ex-vivo microCT that enables to provide volumetric microvasculature information[159], [160].

5.5 ACKNOWLEDGEMENTS

Authors thank to Dr. You-Jin Choi, Dr. Hyunjung An and Dr. Jianhui Zhu for great helps and discussions in preparation and analysis of histology samples.

6.0 CONCLUSIONS

The combined US and PA medical imaging system integrated with the developed innovative technologies provides superior signal and contrast to noise ratio that significantly improves imaging depth of PA imaging, which is one of critical barriers of current PA imaging for eventual translation. The developed system in this dissertation also achieves unprecedented high spatial resolution that opens door to further investigate microvasculature, which has been inherently limited in US enhanced contrast imaging due to the acoustic diffraction limit. The technology development involves a device that enhances laser light delivery scheme for PA imaging, novel dual-mode contrast agent for US/PA imaging as well as photo-stable small molecule dye for PA imaging, and novel super resolution imaging technique for US imaging.

Initial efforts in PA imaging was based on that with conventional laser light delivery scheme a large portion of incident laser energy is lost due to strong reflection on the skin surface. Such light loss directly led to a reduction of PA signal amplitude, thus limiting imaging depth. In this work, the hemisphere-shaped device was developed to recover incident light loss. The device improved PA signal intensity by approximately 30% *in vivo* that is close to the expected light loss from the skin when using the traditional laser delivery scheme. The device was evaluated in mouse cancer imaging *in vivo*. In the next effort in PA imaging, a novel exogenous PA contrast agents that utilizes vaporization, being a more efficient PA mechanism than traditionally used thermal expansion mechanism were developed. In this work, the underlying mechanism of the optically-triggered vaporization process was investigated by concurrent acoustic and optical measurements. The finding based on these observations is highly expected to foster further optimal design parameters of optically-triggered phase transition droplets. In addition, novel near-infrared PA

contrast agents, QR-4PyC4 and QR-G2-COOH, based on quaterylene structure are strategically designed as strong candidates of reliable PA agents for a long-term imaging. QR-4PyC4 is a promising candidate as a universal, sensitive, and reliable PA agent and QR-G2-COOH has potential as a nano-system with its high structural flexibility for PA molecular imaging. The following work was to achieve unprecedented spatial resolution of US imaging beyond the acoustic diffraction limit using innovative microbubble localization technique, so called super-resolution US imaging. In this study, a deconvolution-based microbubble localization technique combined with spatio-temporal interframe correlation based data acquisition technique was developed to not only overcome the traditional physical barrier in the spatial resolution but also improve the temporal resolution that is major shortcoming of typical localization technique. The *in vivo* feasibility of the developed technique was evaluated using the rabbit atherosclerotic plaque model. The spatial resolution was improved by up to 5 times the acoustic diffraction limit with significantly shortened data acquisition time of six seconds or less.

For the long-term goal of the research program, we envision that the developed novel imaging technologies will provide a strong motivation and a key technical foundation to build a US and PA multi-modal imaging system which can be used in pre-clinical and clinical research and for extensive investigations for further translation from benchtop to bedside.

APPENDIX A

LIST OF RELATED JOURNAL PUBLICATIONS AND CONFERENCE PROCEEDINGS

A.1 PEER-REVIEWED JOURNAL PUBLICATIONS

- [1] (Submitted and under review) J. Yu, L. Lavery, and K. Kim, “Super-resolution ultrasound imaging with high temporal resolution: *In vivo* feasibility on vasa vasorum in atherosclerosis rabbit model”
- [2] (Submitted and under review) J. Yu, S. Pin, X. Lin, M. Bai, and K. Kim, “Photostable, Hydrophilic, and Near Infrared Quaterylene-based Dyes for Photoacoustic Imaging”
- [3] (Submitted and under review) X. Lin, J. Yu, N. Feng, and M. Sun, “Aperture orientation effect in the synthetic aperture based linear-array photoacoustic tomography”
- [4] J. Yu, SG Lee, JH Chang, J-K Lee, and K. Kim, “A light illumination enhancement device for photoacoustic imaging: *in vivo* animal study”, IEEE Trans Ultrason Ferroelectr Freq Control 2017 (*featured on the front cover*); 64(8):1205-1211; doi: 10.1109/TUFFC.2017.2713599
- [5] J. Yu, X. Chen, FS Villanueva, and K. Kim, “Vaporization and recondensation dynamics of indocyanine green-loaded perfluoropentane droplets irradiated by a short pulse laser”, Appl. Phys. Lett. 109, 243701 (2016);
- [6] Kagan V.E, Kapralov A, St Croix CM, Watkins S, Kisin E, Kotchey G, Balasubramanian K, Yu J, Kim K, Seo W, Mallampalli R, Star A, Shvedova A. Lung Macrophages "Digest" Carbon Nanotubes Using a Superoxide/Peroxynitrite Oxidative Pathway. ACS Nano, 2014, Vol. 8, No. 6, 5610-5621, DOI: 10.1021/nn406484b.

A.2 CONFERENCE PROCEEDINGS

- [1] J. Yu, L. Lavery, and K. Kim, “*In vivo* super-resolution imaging of vasa vasorum in rabbit atherosclerotic plaque model using deconvolution-based localization technique” in International Ultrasonic Symposium (IUS), 2017 IEEE International, 2017.
- [2] J. Yu, and K. Kim, “Deconvolution-based approach for super-resolution photoacoustic imaging” in Acoustical Society of America 2016.
- [3] J. Yu, F TH Yu, JJ Pacella, FS Villanueva, and K. Kim, “*In vivo* super-resolution imaging of muscle vasculature using microbubble localization technique” in International Ultrasonic Symposium (IUS), 2016 IEEE International, 2016.
- [4] J. Yu, X. Chen, Flordeliza SV, and K. Kim, “High-speed imaging of vaporization and recondensation dynamics of ICG-loaded PFP droplets irradiated by a short pulse laser” in International Ultrasonic Symposium (IUS), 2015 IEEE International, 2015.
- [5] J. Yu, M. M. Nguyen, and K. Kim, “High spatial-resolution cavitation imaging of laser-triggered PFP droplets” in International Ultrasonics Symposium (IUS), 2015 IEEE International, 2015.
- [6] J. Yu, M. M. Nguyen, and K. Kim, “Laser-induced vaporization and acoustic-induced cavitation of droplets,” The Journal of the Acoustical Society of America, vol. 137, no. 4, pp. 2398–2398, Apr. 2015.
- [7] J. Yu, Y. Jung, J. Kang, S. G. Lee, J. H. Chang, J.-K. Lee, and K. Kim, “Enhancement of photoacoustic signal using a novel light illumination improvement device: *In vivo* feasibility animal study,” in International Ultrasonic Symposium (IUS), 2014 IEEE International, 2014, pp. 349–352.

- [8] M. M. Nguyen, X. Ding, J. Yu, D. Park, F. Yu, and K. Kim, “Tri-modality ultrasound imaging system: Design and phantom experiment results,” in International Ultrasonic Symposium (IUS), 2014 IEEE International, 2014, pp. 325–328.

APPENDIX B

THEORETICAL ANALYSIS OF VAPORIZATION CONDITION

B.1 ESTIMATED VAPORIZATION TEMPERATURE THRESHOLD BASED ON THE LAPLACE PRESSURE

For small droplets of perfluoropentane stabilized by bovine serum albumin shells, the developed Laplace pressure may increase boiling temperature. The Laplace pressure is caused by surface tension at the interface between droplet liquid and bulk liquid that can be expressed by

$$\Delta P = P_{inside} - P_{outside} = \frac{2\sigma}{r_{droplet}}$$

where P_{inside} is the pressure inside a droplet, $P_{outside}$ is the pressure outside a droplet (standard atmosphere pressure), σ is surface tension and $r_{droplet}$ is radius of droplet.

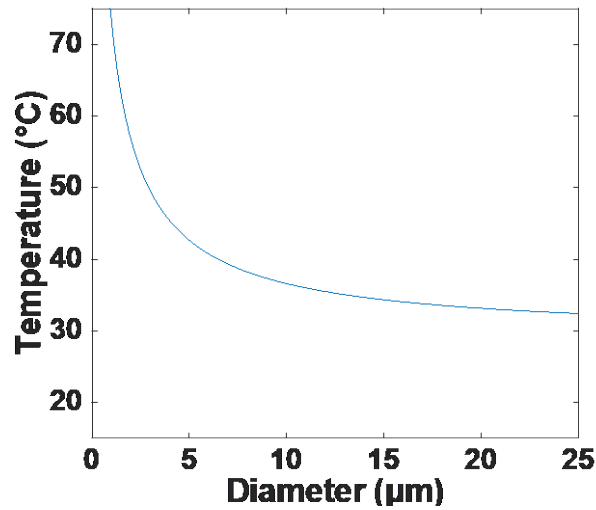


Figure 35. Vaporization threshold temperature according to droplet diameter

The vaporization threshold temperature depending on droplet size can be calculated by using Antoine equation given as

$$\log_{10} P = A - \left(\frac{B}{T + C} \right)$$

where A,B, and C are the constants for the perfluoropentane were reported in previous [76]. Here we used $P_{outside} = 1 \text{ atm}$, $\sigma = 75 \text{ mN/m}$, $A = 6.88375$, $B = 961.192$, and $C = 75512.4$

B.2 ESTIMATED EXPANSION RATIO OF DROPLET

Calculation of Laplace pressure of vaporized droplet at the interface between bubble and bulk liquid can be represented by

$$\Delta P = P_{inside} - P_{outside} = \frac{2\sigma}{r_{bubble}}$$

Ideal gas law can be applied to the vaporized droplet, that is bubble.

$$P_{bubble}V = nRT$$

where P_{bubble} is the pressure inside the bubble, V is the volume of the bubble, n is the amount of substance of the gas, R is the Boltzmann constant, and T is the absolute of the bubble. Here, volume can be expressed by radius if shell thickness can be ignored,

$$V = \frac{4}{3}\pi r_{bubble}^3$$

and n can be calculated by below equation if we assume that the droplet is fully vaporized.

$$n = \frac{4}{3}\pi r_{droplet}^3 \times \text{Density}_{PFP-liquid} \times \frac{1}{\text{MolarWeight}_{PFP}}$$

All these equations can be combined into one equation, it can be expressed by

$$R_{droplet} = \left(\frac{P_{atm}}{\alpha} R_{bubble}^3 + \frac{2\sigma}{\alpha} R_{bubble}^2 \right)^{\frac{1}{3}}$$

where α is constant can be expressed by

$$\alpha = \frac{RT \text{Density}_{PFP-liquid}}{\text{MolarWeight}_{PFP}}$$

The molar weight of perfluoropentane is 288.04 g/mol and the density of perfluoropentane is $1.59 \times 10^6 \text{ g/m}^3$ (at 37°C).

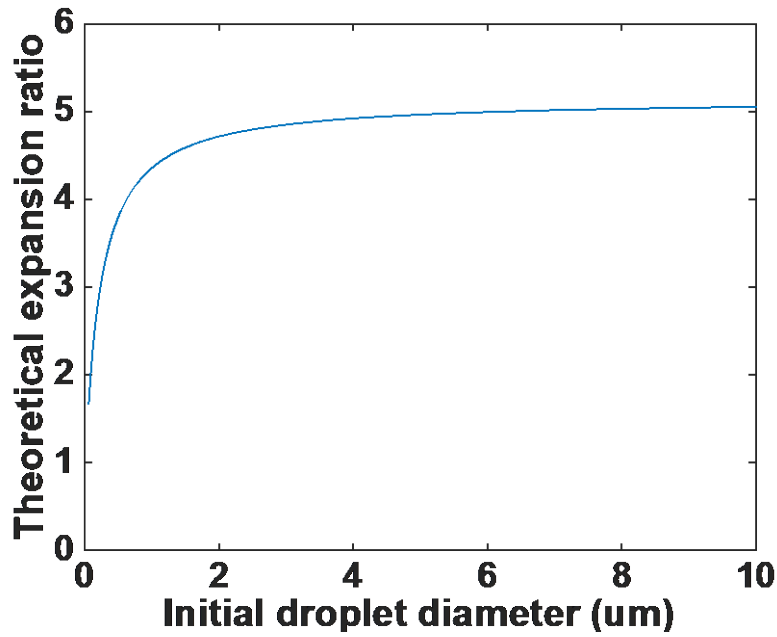


Figure 36. Theoretical expansion ratio vs droplet diameter

APPENDIX C

FPGA DESIGN OF TIMING CONTROLLER IN CHAPTER 3

C.1 SYSTEM DESIGN RESTRICTIONS

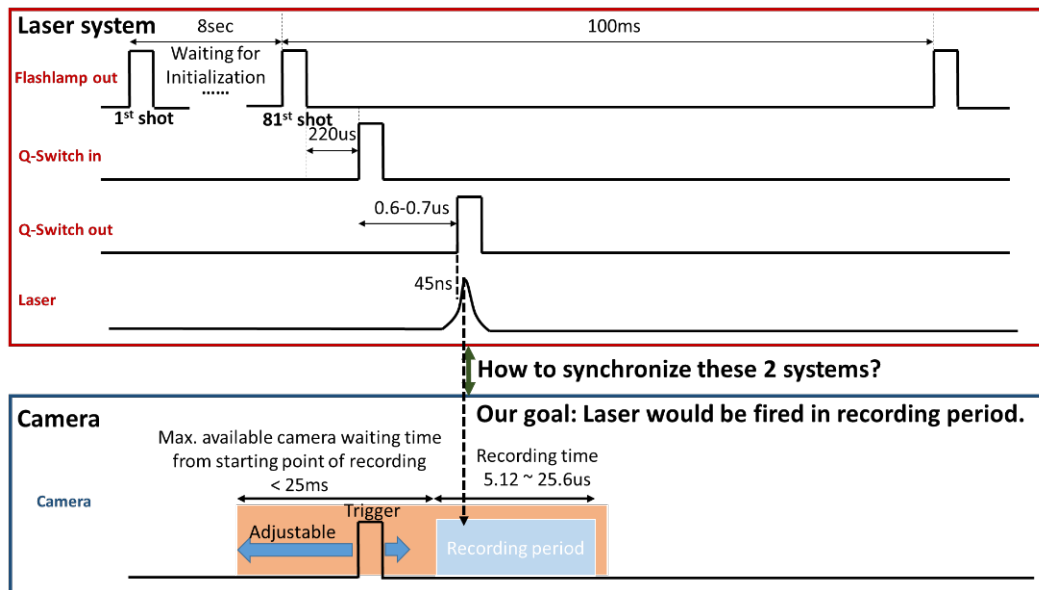


Figure 37. Timing diagram for the laser system and the high-speed camera

- Requirements for laser system (OPOTEK Vibrant 532HE) - Figure 35
 - o Master clock for flash lamp operation should have 10Hz clock with 10% tolerance. It cannot be changed once flashlamp starts.
 - o Delay between “flashlamp sync out” and “Q-Switch external trigger-in” should be $\geq 220\mu$ s. (To get max power, it should be set as 220 μ s). Therefore, signals of flashlamp-out, Q-switch in and Q-switch out is automatically determined depending on flashlamp-out timing to maintain stable and the highest laser power.

- Initialization time of “8 secs” for warm-up should be required to avoid transient thermal effect for Nd:YAG rod when flashlamp start from idle state.
- Requirements for the high-speed camera (UPMC cam, Cordin 512) – Figure 35
 - There are only “Trigger out signal” to other systems and no “Trigger-in” for synchronization purpose.
 - Trigger out signal from the camera can be advanced up to 15 ms from camera recording start. This delay has jitter error due to turbine mechanism.
- Issue and solution
 - In ideal case, synchronization between flashlamp clock (SLOW, 10 Hz) and high-speed camera system (FAST, 5-25 MHz) is required, however the master clock cannot be shared due to system design restriction. Therefore, handshaking communication is necessary between two asynchronous systems. Common approach is triggering from the fast system (the camera) to the slow system (the laser), however, the laser system has to wait 8 secs for warm-up after initial input of flashlamp-in clock while the camera trigger signal can be advanced the only 15 ms. Therefore, the perfect synchronization is not available for this case.
 - Solution: Therefore, there should be some missing case. To maximize success rate, utilization of 10 % tolerance of flashlamp-in (9-11 Hz, therefore, adjusting the laser flashlamep clock adaptively) could have potential to synchronize between two systems with success rate of 20-31.3%. (depending on parameters) In this case, custom-made central timing controller to provide adaptive master clock for the laser system is demanded to manage trigger signals of each system.

Caution! Using external trigger signals for laser operation may give electrical damage (Especially clock control) to the laser system, so, all parameters should be carefully chosen after confirmation of all related signals timing before connecting to the laser system

C.2 BLOCK DIAGRAM

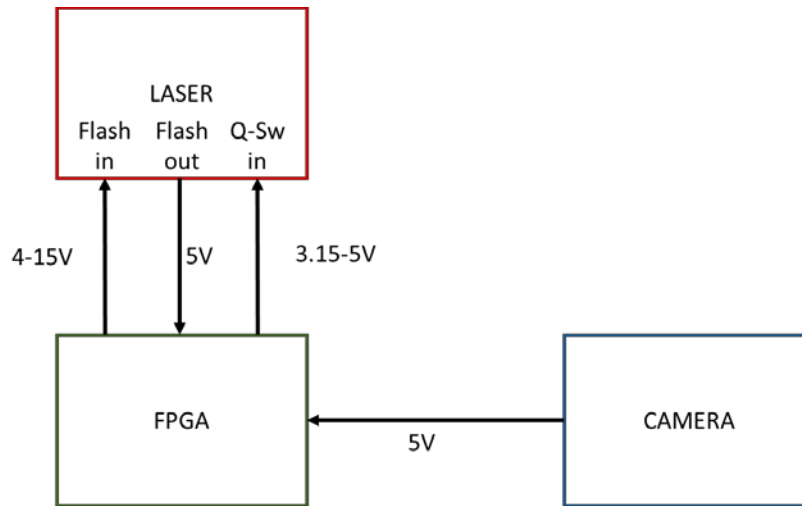


Figure 38. Block diagram of the interface between FPGA, the high-speed camera, and the laser system.

Figure 38 shows the block diagram of interface between FPGA, camera, and laser system. Required input electronic characteristic of synchronization for laser system is shown in below Figure as a reference. All systems are connected by using shielded-BNC cable with 50 ohm impedance. For this setup, the FPGA timing controller generates master clock for the laser system flash lamp and a trigger signal for Q-switch. The laser system should be configured to use external clocks. Using internal clock for Q-switch is not recommended while the internal clock generation mechanism is black box.

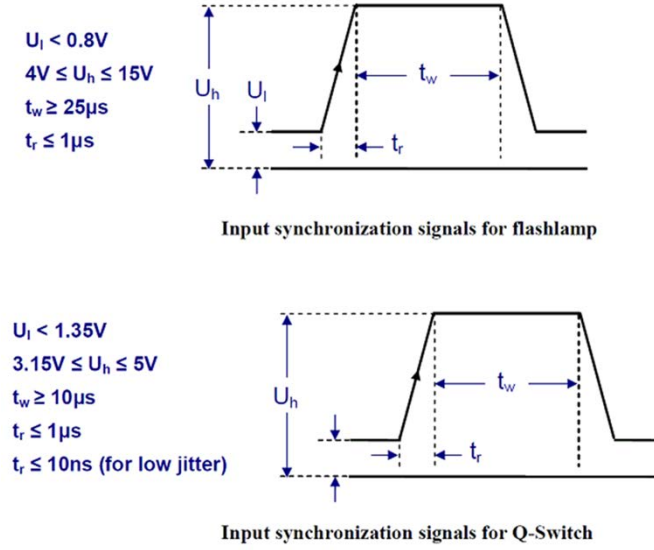


Figure 39. Timing diagram of flash-lamp and Q-switch of the laser system

C.3 TIMING DIAGRAM

As explained in the section B.1, the only flashlamp-in signal can be adjustable within 10 % tolerance. All other signals (Q-Switch in/out) will be determined depending on flashlamp-in signal. First, flash lamp master clock is set as 10 Hz, therefore, period duration of flash lamp clock is 100 ms. This is the maximum time duration for each event. While the master clock duration can be adjustable between 90 – 110ms, the systems can be synchronized only when the camera trigger signal come into between 75 – 95 ms indicated in the red zone. If the camera trigger arrives other than the red zone, the timing controller ignore the camera trigger signal and does not generate Q-switch trigger signal. To increase success rate, flash lamp master clock can be chosen as 9 Hz and corresponding period duration is 110 ms. In this case, success time zone is 75 – 109.5ms, therefore, success rate can be increased up to 31.3 % (34.5 ms / 110 ms). Delay between flashlamp-out and laser excitation may be around 220-230 μs . Around 250 μs is added as a margin. However, the

parameters for this setup is not recommended due to possibility of unexpected system burden. For all experiments, all parameters should be carefully chosen with sufficient margin to minimize malfunction of the laser system.

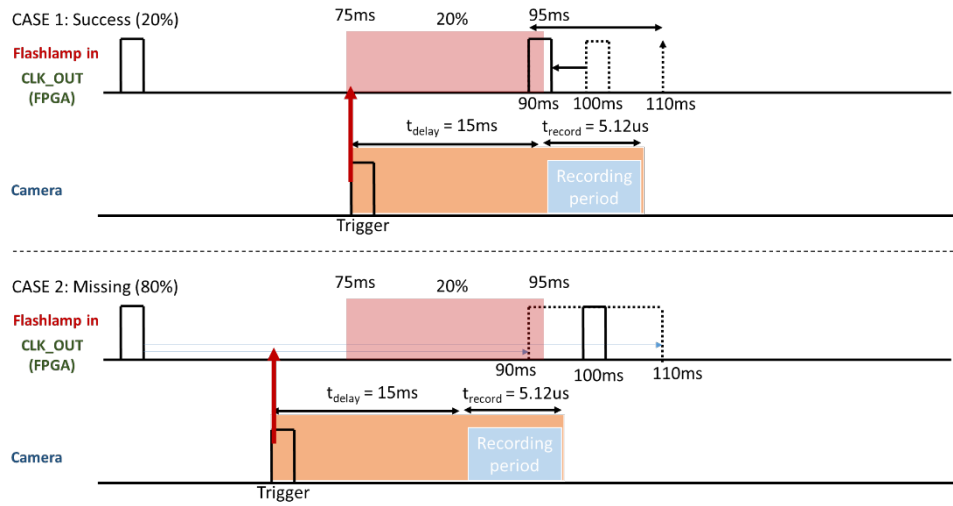
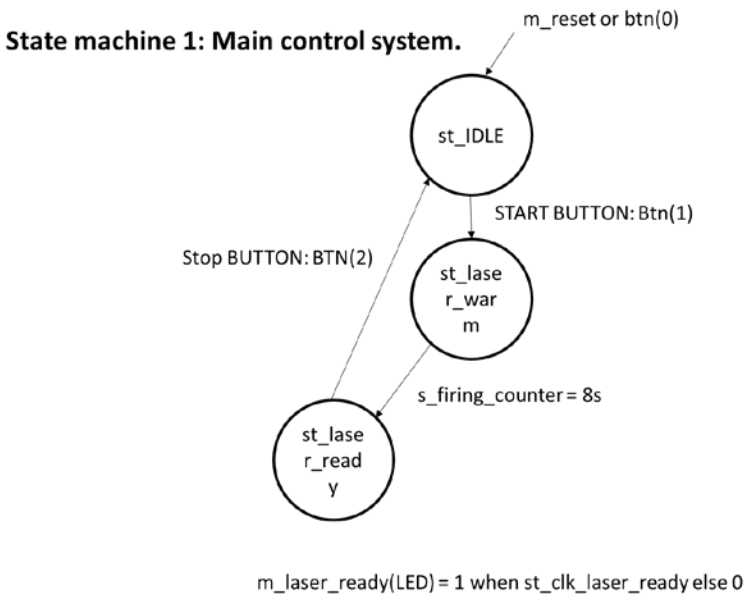
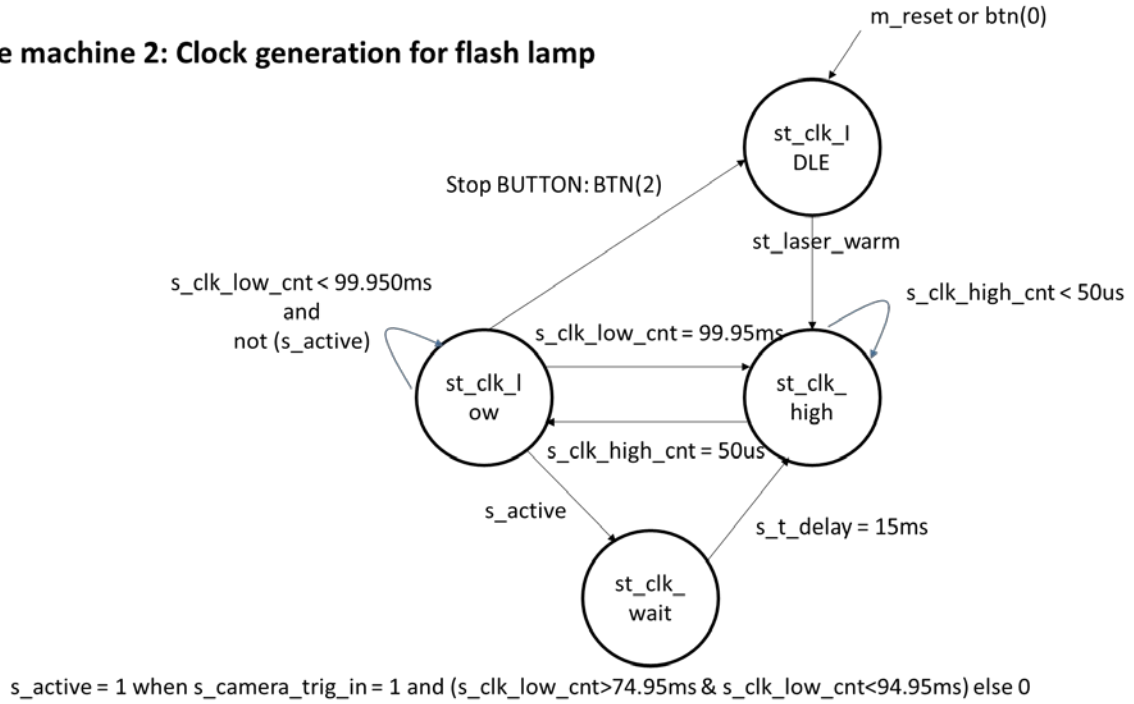


Figure 40. Scenarios for capture success and failure

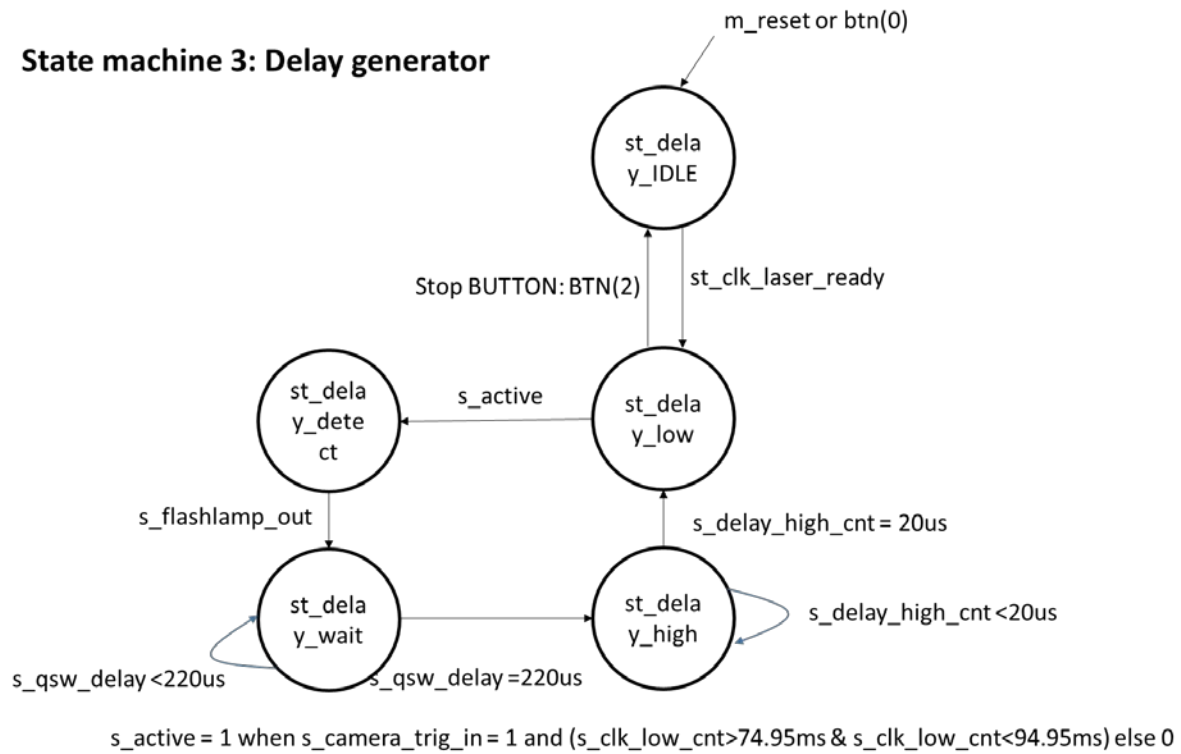
C.4 STATE MACHINE DESIGNS AND IMPLEMENTATIONS



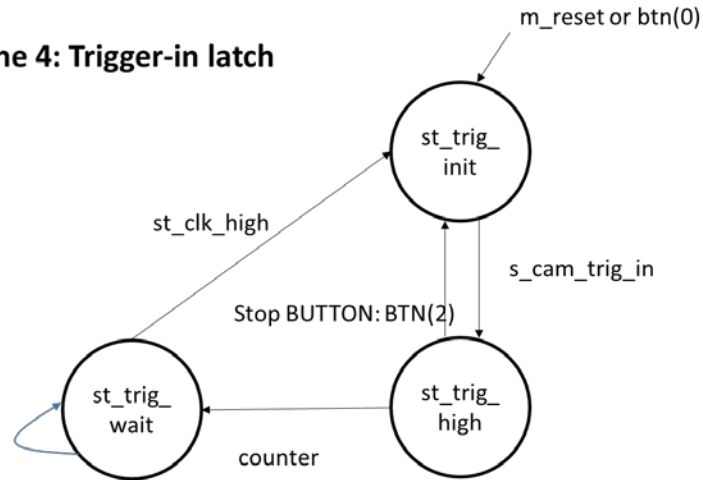
State machine 2: Clock generation for flash lamp



State machine 3: Delay generator



State machine 4: Trigger-in latch



The timing controller written in VHDL (See Appendix. B. 5) is implemented into the FPGA board connected with custom-made input/output circuit as shown in Figure. Below are specification of the FPGA board and development environment (Figure 41).

- FPGA: Xilinx Spartan 6 XC6LX16-CS324 (Digilent Nexsys3 FPGA starter kit)
- Digital system description language: VHDL
- Synthesizer: Xilinx XST
-

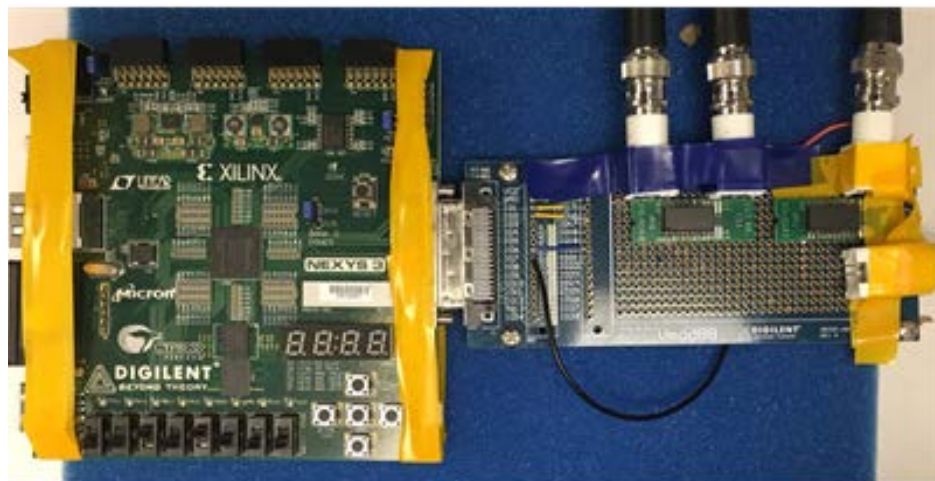


Figure 41. Developed timing controller using FPGA board with add-on input/output circuit

C.5 VHDL HARDWARE DESCRIPTION FOR STATE MACHINE

```
-----
-- University of Pittsburgh
-- Jaesok Yu
--
-- Create Date: 15:12:22 12/28/2013
-- Design Name: Timing controller between the laser system and the camera
-- Module Name: m_timing_top - Behavioral
--
--
-- Revision 0.01
--
-----

library IEEE;
use IEEE.STD_LOGIC_1164.ALL;
use IEEE.STD_LOGIC_ARITH.ALL;
use IEEE.STD_LOGIC_UNSIGNED.ALL;

-- Uncomment the following library declaration if using
-- arithmetic functions with Signed or Unsigned values
--use IEEE.NUMERIC_STD.ALL;

-- Uncomment the following library declaration if instantiating
-- any Xilinx primitives in this code.
--library UNISIM;
--use UNISIM.VComponents.all;

entity m_timing_top is
    Port ( SW : in STD_LOGIC_VECTOR (7 downto 0);
          BTN : in STD_LOGIC_VECTOR (4 downto 0);
          CLK : in STD_LOGIC;
          DATA : out STD_LOGIC_VECTOR (1 downto 0);
          DATA_IN : in STD_LOGIC_VECTOR (0 downto 0);
          LED : out STD_LOGIC_VECTOR (7 downto 0)
        );
end m_timing_top;

architecture Behavioral of m_timing_top is

    type type_delay_state is (st_init, st_active, st_wait);
    signal st_state : type_delay_state;
    signal st_state_data_in : type_delay_state;
    signal s_clk : std_logic;
    signal s_reset: std_logic;
    signal s_delay_start : std_logic;
    signal s_delay_start_data_in : std_logic;
    signal s_tc_pulse : std_logic;
    signal s_tc_wait: std_logic;
    signal s_pulse_delay: std_logic_vector(27 downto 0);
    signal s_wait_delay: std_logic_vector(27 downto 0);
    --signal c_pulse_delay : std_logic_vector(27 downto 0); -- 200ms/Laser Setup : 10Hz
    constant c_pulse_delay : std_logic_vector(27 downto 0) := X"1312D00"; -- 200ms/Laser Setup : 10Hz
```

```

--constant c_pulse_delay : std_logic_vector(27 downto 0) := X"0E4E1C0"; -- 150ms/Laser Setup : 10Hz
--constant c_pulse_delay : std_logic_vector(27 downto 0) := X"0989680"; -- 100ms/Laser Setup : 10Hz
--constant c_pulse_delay : std_logic_vector(27 downto 0) := X"04C4B40"; -- 50ms/Laser Setup : 10Hz
constant c_wait_delay : std_logic_vector(27 downto 0) := X"5F5E100"; -- 1S/ Laser Setup :10Hz

```

```

begin
-- CLK & RESET
-- CLK : 100MHz, 10ns
-- BTN(4) : Reset
s_clk    <= CLK;
s_reset  <= BTN(4); -- Active high reset
s_delay_start <= BTN(0) or s_delay_start_data_in; -- Delay Start
s_delay_start_data_in <= '1' when st_state_data_in = st_active else '0';

```

```

-- Pulse Duration Counter
PulseDuration_Counter : process(s_clk, s_reset)
begin
if s_reset = '1' then
s_pulse_delay <= (others=>'0');
elsif rising_edge(s_clk) then
if st_state = st_active then
s_pulse_delay <= s_pulse_delay + '1';
else
s_pulse_delay <= (others=>'0');
end if;
end if;
end process;
s_tc_pulse <= '1' when s_pulse_delay = c_pulse_delay else '0';

```

```

-- Wait Duration Counter
WaitDuration_Counter : process(s_clk, s_reset)
begin
if s_reset = '1' then
s_wait_delay <= (others=>'0');
elsif rising_edge(s_clk) then
if st_state = st_wait and s_tc_wait = '0' then
s_wait_delay <= s_wait_delay + '1';
elsif st_state = st_wait and s_tc_wait = '1' then
s_wait_delay <= s_wait_delay;
elsif st_state = st_init then
s_wait_delay <= (others=>'0');
else
s_wait_delay <= s_wait_delay;
end if;
end if;
end process;
s_tc_wait <= '1' when s_wait_delay = c_wait_delay else '0';

```

```

-- Main State Machine
MainStateMachine : process(s_clk, s_reset)
begin
if s_reset = '1' then

```

```

        st_state <= st_init;

    elsif rising_edge(s_clk) then
        case st_state is
            when st_init =>
                if s_delay_start = '1' then
                    st_state <= st_active;
                else
                    st_state <= st_init;
                end if;

            when st_active =>
                -- Burst Case
                --
                -- Normal Case
                if s_tc_pulse = '1' and s_delay_start = '0' then

                    if s_tc_pulse = '1' then
                        st_state <= st_wait;
                    else
                        st_state <= st_active;
                    end if;

                when st_wait =>
                    if s_delay_start = '1' or s_tc_wait = '0' then
                        st_state <= st_wait;
                    else
                        st_state <= st_init;
                    end if;
                end case;
            end if;
        end process;

    -- Trigger in
    GenerateTriggerInSignal : process(s_clk, s_reset)
    begin
        if s_reset = '1' then
            st_state_data_in <= st_init;

        elsif rising_edge(s_clk) then
            case st_state_data_in is
                when st_init =>
                    if DATA_IN(0) = '1' then
                        st_state_data_in <= st_active;
                    else
                        st_state_data_in <= st_init;
                    end if;

                when st_active =>
                    st_state_data_in <= st_wait;
                    --
                    --
                    --
                    --
                    if s_tc_pulse = '1' then
                        st_state_data_in <= st_wait;
                    else
                        st_state_data_in <= st_active;
                    end if;

                when st_wait =>
                    if DATA_IN(0) = '1' then

```

```

                                st_state_data_in <= st_wait;
                                else
                                st_state_data_in <= st_init;
                                end if;
                                end case;
                                end if;
                                end process;

-- Trigger Signal Generator
    DATA(0) <= '0' when st_state = st_active else '1';
    DATA(1) <= '1' when st_state = st_active else '0';

-- LED Pins
    LED(0) <= DATA_IN(0) or BTN(0); -- R
    LED(1) <= BTN(1); -- D
--    LED(2) <= BTN(2); -- L
--    LED(3) <= BTN(3); -- U
    LED(2) <= '1' when (st_state_data_in = st_init) or (BTN(2) = '1') else '0'; -- UBTN(1); -- D
    LED(3) <= '1' when st_state_data_in = st_active else '0'; -- U
    LED(4) <= BTN(4); -- RESET
    LED(5) <= '1' when st_state = st_init else '0'; -- Active
    LED(6) <= '1' when st_state = st_active else '0'; -- Active;
    LED(7) <= '1' when st_state = st_wait else '0'; -- Active;
end Behavioral;

```


BIBLIOGRAPHY

- [1] J. Ferlay *et al.*, “Cancer incidence and mortality worldwide: Sources, methods and major patterns in GLOBOCAN 2012,” *Int. J. Cancer*, vol. 136, no. 5, pp. E359–E386, Mar. 2015.
- [2] C. M. C. Tempany *et al.*, “Multimodal imaging for improved diagnosis and treatment of cancers,” *Cancer*, vol. 121, no. 6, pp. 817–827, Mar. 2015.
- [3] L. Fass, “Imaging and cancer: a review,” *Mol. Oncol.*, vol. 2, no. 2, pp. 115–152, Aug. 2008.
- [4] J. Blancher, C. Leger, and L. D. Nguyen, “Time-varying, 3-D echocardiography using a fast-rotating probe,” *IEEE Trans. Ultrason. Ferroelectr. Freq. Control*, vol. 51, no. 5, pp. 634–639, May 2004.
- [5] G. R. Curry and D. N. White, “Color coded ultrasonic differential velocity arterial scanner (Echoflow),” *Ultrasound Med. Biol.*, vol. 4, no. 1, pp. 33–35, Jan. 1978.
- [6] M.-T. Lo, J. Tsao, and D. Su, “Volume scattering of distributed microbubbles and its influence on blood flow estimation,” *IEEE Trans. Ultrason. Ferroelectr. Freq. Control*, vol. 50, no. 12, pp. 1699–1710, Dec. 2003.
- [7] I. Céspedes, J. Ophir, H. Ponnekanti, and N. Maklad, “Elastography: Elasticity Imaging Using Ultrasound with Application to Muscle and Breast in Vivo,” *Ultrason. Imaging*, vol. 15, no. 2, pp. 73–88, Apr. 1993.
- [8] R. M. Lerner, S. R. Huang, and K. J. Parker, “‘Sonoelasticity’ images derived from ultrasound signals in mechanically vibrated tissues,” *Ultrasound Med. Biol.*, vol. 16, no. 3, pp. 231–239, 1990.
- [9] N. Miyanaga *et al.*, “Tissue elasticity imaging for diagnosis of prostate cancer: a preliminary report,” *Int. J. Urol. Off. J. Japanese Urol. Assoc.*, vol. 13, no. 12, pp. 1514–1518, Dec. 2006.
- [10] H. Zhi, B. Ou, B.-M. Luo, X. Feng, Y.-L. Wen, and H.-Y. Yang, “Comparison of ultrasound elastography, mammography, and sonography in the diagnosis of solid breast lesions,” *J. Ultrasound Med. Off. J. Am. Inst. Ultrasound Med.*, vol. 26, no. 6, pp. 807–815, Jun. 2007.
- [11] L. Pallwein *et al.*, “Real-time elastography for detecting prostate cancer: preliminary experience,” *BJU Int.*, vol. 100, no. 1, pp. 42–46, Jul. 2007.
- [12] M. Tsutsumi *et al.*, “The impact of real-time tissue elasticity imaging (elastography) on the detection of prostate cancer: clinicopathological analysis,” *Int. J. Clin. Oncol.*, vol. 12, no. 4, pp. 250–255, Aug. 2007.

- [13] X. Ding, D. Dutta, A. M. Mahmoud, B. Tillman, S. A. Leers, and K. Kim, "An adaptive displacement estimation algorithm for improved reconstruction of thermal strain.," *IEEE Trans. Ultrason. Ferroelectr. Freq. Control*, vol. 62, no. 1, pp. 138–51, Jan. 2015.
- [14] X. Ding *et al.*, "Improved Estimation of Ultrasound Thermal Strain Using Pulse Inversion Harmonic Imaging.," *Ultrasound Med. Biol.*, vol. 42, no. 5, pp. 1182–92, May 2016.
- [15] C. H. Seo, Y. Shi, S.-W. Huang, K. Kim, and M. O'Donnell, "Thermal strain imaging: a review.," *Interface Focus*, vol. 1, no. 4, pp. 649–64, Aug. 2011.
- [16] T. J. Czernuszewicz *et al.*, "Non-invasive in Vivo Characterization of Human Carotid Plaques with Acoustic Radiation Force Impulse Ultrasound: Comparison with Histology after Endarterectomy," *Ultrasound Med. Biol.*, vol. 41, no. 3, pp. 685–697, Mar. 2015.
- [17] A. M. Mahmoud, X. Ding, D. Dutta, V. P. Singh, and K. Kim, "Detecting hepatic steatosis using ultrasound-induced thermal strain imaging: an *ex vivo* animal study," *Phys. Med. Biol.*, vol. 59, no. 4, pp. 881–895, Feb. 2014.
- [18] A. M. Mahmoud, D. Dutta, L. Lavery, D. N. Stephens, F. S. Villanueva, and K. Kim, "Noninvasive detection of lipids in atherosclerotic plaque using ultrasound thermal strain imaging: In vivo animal study," *J. Am. Coll. Cardiol.*, vol. 62, no. 19, pp. 1804–1809, Nov. 2013.
- [19] D. W. Park *et al.*, "Invivo monitoring of structural and mechanical changes of tissue scaffolds by multi-modality imaging," *Biomaterials*, vol. 35, no. 27, pp. 7851–7859, Sep. 2014.
- [20] A. G. Bell, "THE PRODUCTION OF SOUND BY RADIANT ENERGY," *Science*, vol. 2, no. 49, pp. 242–253, May 1881.
- [21] H. F. Zhang, K. Maslov, G. Stoica, and L. V. Wang, "Functional photoacoustic microscopy for high-resolution and noninvasive in vivo imaging," *Nat. Biotechnol.*, vol. 24, no. 7, pp. 848–851, Jul. 2006.
- [22] K. Maslov, H. F. Zhang, S. Hu, and L. V. Wang, "Optical-resolution photoacoustic microscopy for in vivo imaging of single capillaries," *Opt. Lett.*, vol. 33, no. 9, pp. 929–931, May 2008.
- [23] K. H. Song and L. V. Wang, "Deep reflection-mode photoacoustic imaging of biological tissue," *J. Biomed. Opt.*, vol. 12, no. 6, pp. 60503–60503–3, 2007.
- [24] X. Wang, Y. Pang, G. Ku, X. Xie, G. Stoica, and L. V. Wang, "Noninvasive laser-induced photoacoustic tomography for structural and functional in vivo imaging of the brain," *Nat. Biotechnol.*, vol. 21, no. 7, pp. 803–806, 2003.
- [25] A. Agarwal *et al.*, "Targeted gold nanorod contrast agent for prostate cancer detection by photoacoustic imaging," *J. Appl. Phys.*, vol. 102, no. 6, p. 64701, Sep. 2007.

- [26] S. Mallidi, G. P. Luke, and S. Emelianov, "Photoacoustic imaging in cancer detection, diagnosis, and treatment guidance," *Trends Biotechnol.*, vol. 29, no. 5, pp. 213–221, May 2011.
- [27] A. Hellebust and R. Richards-Kortum, "Advances in molecular imaging: targeted optical contrast agents for cancer diagnostics," *Nanomedicine (Lond.)*, vol. 7, no. 3, pp. 429–445, Mar. 2012.
- [28] M. C. Pierce, D. J. Javier, and R. Richards-Kortum, "Optical contrast agents and imaging systems for detection and diagnosis of cancer," *Int. J. Cancer*, vol. 123, no. 9, pp. 1979–1990, Nov. 2008.
- [29] M. Rajadhyaksha, M. Grossman, D. Esterowitz, R. H. Webb, and R. R. Anderson, "In vivo confocal scanning laser microscopy of human skin: melanin provides strong contrast," *J. Invest. Dermatol.*, vol. 104, no. 6, pp. 946–952, Jun. 1995.
- [30] P. M. Lane *et al.*, "Simple device for the direct visualization of oral-cavity tissue fluorescence," *J. Biomed. Opt.*, vol. 11, no. 2, p. 24006, Apr. 2006.
- [31] A. Badon, D. Li, G. Lerosey, A. C. Boccara, M. Fink, and A. Aubry, "Smart optical coherence tomography for ultra-deep imaging through highly scattering media.," *Sci. Adv.*, vol. 2, no. 11, p. e1600370, Nov. 2016.
- [32] C. Kim, T. N. Erpelding, L. Jankovic, M. D. Pashley, and L. V. Wang, "Deeply penetrating in vivo photoacoustic imaging using a clinical ultrasound array system," *Biomed. Opt. Express*, vol. 1, no. 1, p. 278, Aug. 2010.
- [33] J. M. Brown and W. R. Wilson, "Exploiting tumour hypoxia in cancer treatment," *Nat. Rev. Cancer*, vol. 4, no. 6, pp. 437–447, Jun. 2004.
- [34] S. Hu and L. V Wang, "Neurovascular photoacoustic tomography.," *Front. Neuroenergetics*, vol. 2, p. 10, 2010.
- [35] "ANSI Z136.1, American National Standard for Safe Use of Lasers." American National Standards Institute Inc, 2007.
- [36] L. M. Lyamshev, "Optoacoustic sources of sound," *Sov. Phys. Uspekhi*, vol. 24, no. 12, pp. 977–995, Dec. 1981.
- [37] M. W. Sigrist, "Laser generation of acoustic waves in liquids and gases," *J. Appl. Phys.*, vol. 60, no. 7, pp. R83–R122, Oct. 1986.
- [38] H. Chen and G. Diebold, "Chemical Generation of Acoustic Waves: A Giant Photoacoustic Effect," *Science (80-.)*, vol. 270, no. 5238, pp. 963–966, Nov. 1995.
- [39] J. Yu, X. Chen, F. S. Villanueva, and K. Kim, "Vaporization and recondensation dynamics of indocyanine green-loaded perfluoropentane droplets irradiated by a short pulse laser," *Appl. Phys. Lett.*, vol. 109, no. 24, p. 243701, 2016.

- [40] K. Wilson, K. Homan, S. Emelianov, S. Dong, and J. B. Fowlkes, "Biomedical photoacoustics beyond thermal expansion using triggered nanodroplet vaporization for contrast-enhanced imaging," *Nat. Commun.*, vol. 3, p. 618, Jan. 2012.
- [41] A. Hannah, G. Luke, K. Wilson, K. Homan, and S. Emelianov, "Indocyanine green-loaded photoacoustic nanodroplets: dual contrast nanoconstructs for enhanced photoacoustic and ultrasound imaging," *ACS Nano*, vol. 8, no. 1, pp. 250–259, Jan. 2014.
- [42] P. Shao, S. Zhang, and M. Bai, "Near Infrared Fluorescent Quaterrylenediimide-cored Dendrimers for Bio-imaging," in *Optics in the Life Sciences*, 2015, p. OM4D.6.
- [43] J. Yao, K. I. Maslov, Y. Zhang, Y. Xia, and L. V. Wang, "Label-free oxygen-metabolic photoacoustic microscopy in vivo," *J. Biomed. Opt.*, vol. 16, no. 7, pp. 76003-76003–11, 2011.
- [44] J.-T. Oh, M.-L. Li, H. F. Zhang, K. Maslov, G. Stoica, and L. V. Wang, "Three-dimensional imaging of skin melanoma in vivo by dual-wavelength photoacoustic microscopy," *J. Biomed. Opt.*, vol. 11, no. 3, p. 34032, 2006.
- [45] J. Weber, P. C. Beard, and S. E. Bohndiek, "Contrast agents for molecular photoacoustic imaging," *Nat. Methods*, vol. 13, no. 8, pp. 639–650, Jul. 2016.
- [46] P. Shao and M. Bai, "Photostable, hydrophilic and functional near infrared quaterrylenediimide-cored dendrimers for biomedical imaging.," *Chem. Commun. (Camb).*, vol. 48, no. 76, pp. 9498–500, Oct. 2012.
- [47] C. D. Geddes, H. Cao, and J. R. Lakowicz, "Enhanced photostability of ICG in close proximity to gold colloids," *Spectrochim. Acta Part A Mol. Biomol. Spectrosc.*, vol. 59, no. 11, pp. 2611–2617, Sep. 2003.
- [48] M. Zhang, M. Yudasaka, K. Ajima, J. Miyawaki, and S. Iijima, "Light-Assisted Oxidation of Single-Wall Carbon Nanohorns for Abundant Creation of Oxygenated Groups That Enable Chemical Modifications with Proteins To Enhance Biocompatibility," *ACS Nano*, vol. 1, no. 4, pp. 265–272, Nov. 2007.
- [49] A. P. Leonov, J. Zheng, J. D. Clogston, S. T. Stern, A. K. Patri, and A. Wei, "Detoxification of Gold Nanorods by Treatment with Polystyrenesulfonate," *ACS Nano*, vol. 2, no. 12, pp. 2481–2488, Dec. 2008.
- [50] J. Frangioni, "In vivo near-infrared fluorescence imaging," *Curr. Opin. Chem. Biol.*, vol. 7, no. 5, pp. 626–634, Oct. 2003.
- [51] C. Errico *et al.*, "Ultrafast ultrasound localization microscopy for deep super-resolution vascular imaging.," *Nature*, vol. 527, no. 7579, pp. 499–502, 2015.
- [52] K. Christensen-Jeffries, R. J. Browning, M. X. Tang, C. Dunsby, and R. J. Eckersley, "In vivo acoustic super-resolution and super-resolved velocity mapping using microbubbles," *IEEE Trans. Med. Imaging*, vol. 34, no. 2, pp. 433–440, 2015.

- [53] P. Korkolopoulou *et al.*, “Prognostic evaluation of the microvascular network in myelodysplastic syndromes,” *Leukemia*, vol. 15, no. 9, pp. 1369–1376, Sep. 2001.
- [54] E. Betzig *et al.*, “Imaging Intracellular Fluorescent Proteins at Nanometer Resolution,” *Science* (80-.), vol. 313, no. 5793, pp. 1642–1645, Sep. 2006.
- [55] S. T. Hess, T. P. K. Girirajan, and M. D. Mason, “Ultra-High Resolution Imaging by Fluorescence Photoactivation Localization Microscopy,” *Biophys. J.*, vol. 91, no. 11, pp. 4258–4272, Dec. 2006.
- [56] C. Dmené *et al.*, “Spatiotemporal Clutter Filtering of Ultrafast Ultrasound Data Highly Increases Doppler and fUltrasound Sensitivity,” *IEEE Trans. Med. Imaging*, vol. 34, no. 11, pp. 2271–2285, Nov. 2015.
- [57] E. A. Mukamel, H. Babcock, and X. Zhuang, “Statistical deconvolution for superresolution fluorescence microscopy,” *Biophys. J.*, vol. 102, no. 10, pp. 2391–2400, 2012.
- [58] J. Yu, L. Lavery, and K. Kim, “In vivo super-resolution imaging of vasa vasorum in rabbit atherosclerotic plaque model using deconvolution-based localization technique,” in *2017 IEEE International Ultrasonics Symposium (IUS)*, 2017, pp. 1–1.
- [59] A. Bar-zion, C. Tremblay-darveau, O. Solomon, D. Adam, and Y. C. Eldar, “Super-Resolution Ultrasound Imaging of Vascular Structures with High Temporal Resolution,” vol. 7, pp. 1–11.
- [60] A. Bar-Zion, C. Tremblay-Darveau, O. Solomon, D. Adam, and Y. C. Eldar, “Fast Vascular Ultrasound Imaging With Enhanced Spatial Resolution and Background Rejection,” *IEEE Trans. Med. Imaging*, vol. 36, no. 1, pp. 169–180, Jan. 2017.
- [61] K. Kwon, T. Son, K.-J. Lee, and B. Jung, “Enhancement of light propagation depth in skin: cross-validation of mathematical modeling methods,” *Lasers Med. Sci.*, vol. 24, no. 4, pp. 605–615, Jul. 2009.
- [62] C. Yeo *et al.*, “Development of compression-controlled low-level laser probe system: towards clinical application,” *Lasers Med. Sci.*, vol. 25, no. 5, pp. 699–704, Sep. 2010.
- [63] Z. Wang, S. Ha, and K. Kim, “A new design of light illumination scheme for deep tissue photoacoustic imaging,” *Opt. Express*, vol. 20, no. 20, pp. 22649–59, Sep. 2012.
- [64] J. D. Hardy and C. Muschenheim, “RADIATION OF HEAT FROM THE HUMAN BODY. V. THE TRANSMISSION OF INFRA-RED RADIATION THROUGH SKIN,” *J. Clin. Invest.*, vol. 15, no. 1, pp. 1–9, Jan. 1936.
- [65] J. D. Hardy, H. T. Hammel, and D. Murgatroyd, “Spectral Transmittance and Reflectance of Excised Human Skin,” *J. Appl. Physiol.*, vol. 9, no. 2, pp. 257–264, Sep. 1956.
- [66] P. Han and Y.-C. Tseng, “Spectral Shift Amplification and Polarization-Controlled Spectral Shift with Silver Metal,” *Metals (Basel)*, vol. 6, no. 1, p. 7, Dec. 2015.

- [67] L. Nie, X. Cai, K. Maslov, A. Garcia-Urbe, M. A. Anastasio, and L. V. Wang, "Photoacoustic tomography through a whole adult human skull with a photon recycler," *J. Biomed. Opt.*, vol. 17, no. 11, pp. 110506–110506, 2012.
- [68] J. Yu *et al.*, "Enhancement of photoacoustic signal using a novel light illumination improvement device: In vivo feasibility animal study," 2014, pp. 349–352.
- [69] L. V. Wang, "Tutorial on Photoacoustic Microscopy and Computed Tomography," *IEEE J. Sel. Top. Quantum Electron.*, vol. 14, no. 1, pp. 171–179, Jan. 2008.
- [70] M. L. Landsman, G. Kwant, G. A. Mook, and W. G. Zijlstra, "Light-absorbing properties, stability, and spectral stabilization of indocyanine green," *J. Appl. Physiol.*, vol. 40, no. 4, pp. 575–583, Apr. 1976.
- [71] J. T. Alander *et al.*, "A review of indocyanine green fluorescent imaging in surgery," *Int. J. Biomed. Imaging*, vol. 2012, p. 940585, 2012.
- [72] P. Beard, "Biomedical photoacoustic imaging," *Interface Focus*, p. rsfs20110028, Jun. 2011.
- [73] M. Xu and L. V. Wang, "Photoacoustic imaging in biomedicine," *Rev. Sci. Instrum.*, vol. 77, no. 4, p. 41101, Apr. 2006.
- [74] E. Strohm, M. Rui, I. Gorelikov, N. Matsuura, and M. Kolios, "Vaporization of perfluorocarbon droplets using optical irradiation," *Biomed. Opt. Express*, vol. 2, no. 6, p. 1432, Jun. 2011.
- [75] C. Wei *et al.*, "Nonlinear contrast enhancement in photoacoustic molecular imaging with gold nanosphere encapsulated nanoemulsions," *Appl. Phys. Lett.*, vol. 104, no. 3, p. 33701, Jan. 2014.
- [76] E. J. Barber and G. H. Cady, "Vapor Pressures of Perfluoropentanes," *J. Phys. Chem.*, vol. 60, no. 4, pp. 504–505, Apr. 1956.
- [77] R. Asami and K. Kawabata, "Repeatable vaporization of optically vaporizable perfluorocarbon droplets for photoacoustic contrast enhanced imaging," in *2012 IEEE International Ultrasonics Symposium*, 2012, pp. 1200–1203.
- [78] G. Lajoinie *et al.*, "Ultrafast vapourization dynamics of laser-activated polymeric microcapsules," *Nat. Commun.*, vol. 5, p. 3671, Apr. 2014.
- [79] V. B. Rodriguez, S. M. Henry, A. S. Hoffman, P. S. Stayton, X. Li, and S. H. Pun, "Encapsulation and stabilization of indocyanine green within poly(styrene-alt-maleic anhydride) block-poly(styrene) micelles for near-infrared imaging," *J. Biomed. Opt.*, vol. 13, no. 1, pp. 14025–14025–10, 2008.
- [80] X. Chen, J. Wang, M. Versluis, N. de Jong, and F. S. Villanueva, "Ultra-fast bright field and fluorescence imaging of the dynamics of micrometer-sized objects," *Rev. Sci. Instrum.*, vol. 84, no. 6, p. 63701, Jun. 2013.

- [81] X. Chen, K. Q. Schwarz, and K. J. Parker, "Radiation pattern of a focused transducer: a numerically convergent solution," *J. Acoust. Soc. Am.*, vol. 94, no. 5, pp. 2979–2991, Nov. 1993.
- [82] X. Chen, K. Q. Schwarz, and K. J. Parker, "Acoustic coupling from a focused transducer to a flat plate and back to the transducer," *J. Acoust. Soc. Am.*, vol. 95, no. 6, pp. 3049–3054, Jun. 1994.
- [83] X. Chen, D. Phillips, K. Q. Schwarz, J. G. Mottley, and K. J. Parker, "The measurement of backscatter coefficient from a broadband pulse-echo system: a new formulation," *IEEE Trans. Ultrason. Ferroelectr. Freq. Control*, vol. 44, no. 2, pp. 515–525, 1997.
- [84] L. R. O. M. F.R.S, "VIII. On the pressure developed in a liquid during the collapse of a spherical cavity," *Philos. Mag. Ser. 6*, vol. 34, no. 200, pp. 94–98, Aug. 1917.
- [85] S. Hilgenfeldt, D. Lohse, and M. Zomack, "Response of bubbles to diagnostic ultrasound: a unifying theoretical approach," *Eur. Phys. J. B*, vol. 4, no. 2, pp. 247–255, Aug. 1998.
- [86] J. C. Bird, R. de Ruiter, L. Courbin, and H. A. Stone, "Daughter bubble cascades produced by folding of ruptured thin films," *Nature*, vol. 465, no. 7299, pp. 759–762, Jun. 2010.
- [87] N. Y. Rapoport, A. M. Kennedy, J. E. Shea, C. L. Scaife, and K.-H. Nam, "Controlled and targeted tumor chemotherapy by ultrasound-activated nanoemulsions/microbubbles," *J. Control. Release Off. J. Control. Release Soc.*, vol. 138, no. 3, pp. 268–276, Sep. 2009.
- [88] T. Windvoel, M. Mbanjwa, N. Mokone, A. Mogale, and K. Land, "Surface analysis of polydimethylsiloxane fouled with bovine serum albumin," Jan. 2010.
- [89] E. A. Neppiras, "Acoustic cavitation," *Phys. Rep.*, vol. 61, no. 3, pp. 159–251, May 1980.
- [90] O. D. Kripfgans, J. B. Fowlkes, D. L. Miller, O. P. Eldevik, and P. L. Carson, "Acoustic droplet vaporization for therapeutic and diagnostic applications," *Ultrasound Med. Biol.*, vol. 26, no. 7, pp. 1177–1189, Sep. 2000.
- [91] O. D. Kripfgans, M. L. Fabiilli, P. L. Carson, and J. B. Fowlkes, "On the acoustic vaporization of micrometer-sized droplets," *J. Acoust. Soc. Am.*, vol. 116, no. 1, pp. 272–281, Jul. 2004.
- [92] O. Shpak, L. Stricker, M. Versluis, and D. Lohse, "The role of gas in ultrasonically driven vapor bubble growth," *Phys. Med. Biol.*, vol. 58, no. 8, pp. 2523–2535, Apr. 2013.
- [93] T. Ye and J. L. Bull, "Direct numerical simulations of micro-bubble expansion in gas embolotherapy," *J. Biomech. Eng.*, vol. 126, no. 6, pp. 745–759, Dec. 2004.
- [94] A. Qamar, Z. Z. Wong, J. B. Fowlkes, and J. L. Bull, "Dynamics of acoustic droplet vaporization in gas embolotherapy," *Appl. Phys. Lett.*, vol. 96, no. 14, p. 143702, Apr. 2010.

- [95] N. Reznik *et al.*, “Optical studies of vaporization and stability of fluorescently labelled perfluorocarbon droplets,” *Phys. Med. Biol.*, vol. 57, no. 21, pp. 7205–7217, Nov. 2012.
- [96] J. D. Dove, M. A. Borden, and T. W. Murray, “Optically induced resonance of nanoparticle-loaded microbubbles,” *Opt. Lett.*, vol. 39, no. 13, p. 3732, Jul. 2014.
- [97] J. S. Lum, J. D. Dove, T. W. Murray, and M. A. Borden, “Single Microbubble Measurements of Lipid Monolayer Viscoelastic Properties for Small-Amplitude Oscillations,” *Langmuir*, vol. 32, no. 37, pp. 9410–9417, Sep. 2016.
- [98] C. I. Castro and J. C. Briceno, “Perfluorocarbon-Based Oxygen Carriers: Review of Products and Trials,” *Artif. Organs*, vol. 34, no. 8, pp. 622–634, Aug. 2010.
- [99] E. M. Strohm, M. Rui, M. C. Kolios, I. Gorelikov, and N. Matsuura, “Optical droplet vaporization (ODV): Photoacoustic characterization of perfluorocarbon droplets,” in *2010 IEEE International Ultrasonics Symposium*, 2010, pp. 495–498.
- [100] R. Williams *et al.*, “Characterization of Submicron Phase-change Perfluorocarbon Droplets for Extravascular Ultrasound Imaging of Cancer,” *Ultrasound Med. Biol.*, vol. 39, no. 3, pp. 475–489, Mar. 2013.
- [101] E. Strohm, M. Rui, I. Gorelikov, N. Matsuura, and M. Kolios, “Optical droplet vaporization of micron-sized perfluorocarbon droplets and their photoacoustic detection,” 2011, vol. 7899, p. 78993H–78993H–7.
- [102] C. Chen, Y. Gu, J. Tu, X. Guo, and D. Zhang, “Microbubble oscillating in a microvessel filled with viscous fluid: A finite element modeling study,” *Ultrasonics*, vol. 66, pp. 54–64, Mar. 2016.
- [103] D. B. Khismatullin, “Resonance frequency of microbubbles: effect of viscosity,” *J. Acoust. Soc. Am.*, vol. 116, no. 3, pp. 1463–1473, Sep. 2004.
- [104] E. Sassaroli and K. Hynynen, “Forced linear oscillations of microbubbles in blood capillaries,” *J. Acoust. Soc. Am.*, vol. 115, no. 6, pp. 3235–3243, Jun. 2004.
- [105] M. L. Fabiilli, K. J. Haworth, N. H. Fakhri, O. D. Kripfgans, P. L. Carson, and J. B. Fowlkes, “The role of inertial cavitation in acoustic droplet vaporization,” *IEEE Trans. Ultrason. Ferroelectr. Freq. Control*, vol. 56, no. 5, pp. 1006–1017, May 2009.
- [106] S.-T. Kang, Y.-L. Huang, and C.-K. Yeh, “Characterization of acoustic droplet vaporization for control of bubble generation under flow conditions,” *Ultrasound Med. Biol.*, vol. 40, no. 3, pp. 551–561, Mar. 2014.
- [107] B. Helfield, J. J. Black, B. Qin, J. Pacella, X. Chen, and F. S. Villanueva, “Fluid Viscosity Affects the Fragmentation and Inertial Cavitation Threshold of Lipid-Encapsulated Microbubbles,” *Ultrasound Med. Biol.*, vol. 42, no. 3, pp. 782–794, Mar. 2016.

- [108] L. V. Wang and S. Hu, "Photoacoustic Tomography: In Vivo Imaging from Organelles to Organs," *Science* (80-.), vol. 335, no. 6075, pp. 1458–1462, Mar. 2012.
- [109] J. F. Lovell *et al.*, "Porphysome nanovesicles generated by porphyrin bilayers for use as multimodal biophotonic contrast agents," *Nat. Mater.*, vol. 10, no. 4, pp. 324–332, Apr. 2011.
- [110] C. Kim, K. H. Song, F. Gao, and L. V. Wang, "Sentinel Lymph Nodes and Lymphatic Vessels: Noninvasive Dual-Modality in Vivo Mapping by Using Indocyanine Green in Rats—Volumetric Spectroscopic Photoacoustic Imaging and Planar Fluorescence Imaging," *Radiology*, vol. 255, no. 2, pp. 442–450, May 2010.
- [111] J. Yu, J. S. J. S. Schuman, J.-K. J.-K. Lee, S. G. S.-G. Lee, J. H. J. H. Chang, and K. Kim, "A light illumination enhancement device for photoacoustic imaging: in vivo animal study," *IEEE Trans. Ultrason. Ferroelectr. Freq. Control*, vol. 64, no. 8, pp. 1205–1211, 2017.
- [112] V. E. Kagan *et al.*, "Lung macrophages Digest carbon nanotubes using a superoxide/peroxynitrite oxidative pathway," *ACS Nano*, vol. 8, no. 6, 2014.
- [113] M. Pramanik, K. H. Song, M. Swierczewska, D. Green, B. Sitharaman, and L. V Wang, "*In vivo* carbon nanotube-enhanced non-invasive photoacoustic mapping of the sentinel lymph node," *Phys. Med. Biol.*, vol. 54, no. 11, pp. 3291–3301, Jun. 2009.
- [114] A. De La Zerda *et al.*, "Carbon nanotubes as photoacoustic molecular imaging agents in living mice," *Nat. Nanotechnol.*, vol. 3, no. 9, pp. 557–562, Sep. 2008.
- [115] J. V. Jokerst, A. J. Cole, D. Van de Sompel, and S. S. Gambhir, "Gold Nanorods for Ovarian Cancer Detection with Photoacoustic Imaging and Resection Guidance via Raman Imaging in Living Mice," *ACS Nano*, vol. 6, no. 11, pp. 10366–10377, Nov. 2012.
- [116] H. Moon *et al.*, "Amplified Photoacoustic Performance and Enhanced Photothermal Stability of Reduced Graphene Oxide Coated Gold Nanorods for Sensitive Photoacoustic Imaging," *ACS Nano*, vol. 9, no. 3, pp. 2711–2719, Mar. 2015.
- [117] S. Ha, A. Carson, A. Agarwal, N. A. Kotov, and K. Kim, "Detection and monitoring of the multiple inflammatory responses by photoacoustic molecular imaging using selectively targeted gold nanorods.," *Biomed. Opt. Express*, vol. 2, no. 3, pp. 645–57, Feb. 2011.
- [118] Y.-S. Chen, W. Frey, S. Kim, P. Kruizinga, K. Homan, and S. Emelianov, "Silica-coated gold nanorods as photoacoustic signal nanoamplifiers.," *Nano Lett.*, vol. 11, no. 2, pp. 348–54, Feb. 2011.
- [119] K. Kim *et al.*, "Photoacoustic imaging of early inflammatory response using gold nanorods," *Appl. Phys. Lett.*, vol. 90, no. 22, p. 223901, May 2007.
- [120] J. D. Dove, P. A. Mountford, T. W. Murray, and M. A. Borden, "Engineering optically triggered droplets for photoacoustic imaging and therapy.," *Biomed. Opt. Express*, vol. 5, no. 12, pp. 4417–27, Dec. 2014.

- [121] H. N. Shrivastava and J. C. Speakman, "The Crystal and Molecular Structure of Quaterylene," *Proc. R. Soc. London A Math. Phys. Eng. Sci.*, vol. 257, no. 1291, 1960.
- [122] F. Song, X. Peng, E. Lu, R. Zhang, X. Chen, and B. Song, "Syntheses, spectral properties and photostabilities of novel water-soluble near-infrared cyanine dyes," *J. Photochem. Photobiol. A Chem.*, vol. 168, no. 1, pp. 53–57, 2004.
- [123] G. Hong, A. L. Antaris, and H. Dai, "Near-infrared fluorophores for biomedical imaging," *Nat. Biomed. Eng.*, vol. 1, no. 1, p. 10, Jan. 2017.
- [124] K. Pu *et al.*, "Semiconducting polymer nanoparticles as photoacoustic molecular imaging probes in living mice," *Nat. Nanotechnol.*, vol. 9, no. 3, pp. 233–9, Mar. 2014.
- [125] A. de la Zerda *et al.*, "Family of Enhanced Photoacoustic Imaging Agents for High-Sensitivity and Multiplexing Studies in Living Mice," *ACS Nano*, vol. 6, no. 6, pp. 4694–4701, Jun. 2012.
- [126] K. K. Ng *et al.*, "Stimuli-responsive photoacoustic nanoswitch for in vivo sensing applications," *ACS Nano*, vol. 8, no. 8, pp. 8363–8373, Aug. 2014.
- [127] S. Sreejith *et al.*, "Near-Infrared Squaraine Dye Encapsulated Micelles for in Vivo Fluorescence and Photoacoustic Bimodal Imaging," *ACS Nano*, vol. 9, no. 6, pp. 5695–5704, Jun. 2015.
- [128] Y. Wang *et al.*, "Visible light-driven organic form-stable phase change materials for solar energy storage," *RSC Adv.*, vol. 2, no. 14, p. 5964, 2012.
- [129] J. M. Janjic, P. Shao, S. Zhang, X. Yang, S. K. Patel, and M. Bai, "Perfluorocarbon nanoemulsions with fluorescent, colloidal and magnetic properties," *Biomaterials*, vol. 35, no. 18, pp. 4958–4968, Jun. 2014.
- [130] K. K. Nadakavukaren and J. Nadakavukaren, "Increased Rhodamine 123 Uptake by Carcinoma Cells1," *CANCER Res.*, vol. 45, pp. 6093–6099, 1985.
- [131] Y. Shapovalov, D. Hoffman, D. Zuch, K. L. de Mesy Bentley, and R. A. Eliseev, "Mitochondrial Dysfunction in Cancer Cells Due to Aberrant Mitochondrial Replication," *J. Biol. Chem.*, vol. 286, no. 25, pp. 22331–22338, Jun. 2011.
- [132] J. H. Park and N. Oh, "Endocytosis and exocytosis of nanoparticles in mammalian cells," *Int. J. Nanomedicine*, vol. 9, no. Supplement 1, p. 51, May 2014.
- [133] F. G. Fowkes, E. Housley, E. H. Cawood, C. C. Macintyre, C. V Ruckley, and R. J. Prescott, "Edinburgh Artery Study: prevalence of asymptomatic and symptomatic peripheral arterial disease in the general population," *Int. J. Epidemiol.*, vol. 20, no. 2, pp. 384–92, Jun. 1991.

- [134] V. Fuster, Z. A. Fayad, P. R. Moreno, M. Poon, R. Corti, and J. J. Badimon, "Atherothrombosis and High-Risk Plaque: Part II: Approaches by Noninvasive Computed Tomographic/Magnetic Resonance Imaging," *J. Am. Coll. Cardiol.*, vol. 46, no. 7, pp. 1209–1218, 2005.
- [135] M. Naghavi *et al.*, "From Vulnerable Plaque to Vulnerable Patient," *Circulation*, vol. 108, no. 14, 2003.
- [136] P. R. Moreno *et al.*, "Plaque Neovascularization Is Increased in Ruptured Atherosclerotic Lesions of Human Aorta," *Circulation*, vol. 110, no. 14, 2004.
- [137] A. Taruya *et al.*, "Vasa Vasorum Restructuring in Human Atherosclerotic Plaque Vulnerability," *J. Am. Coll. Cardiol.*, vol. 65, no. 23, 2015.
- [138] D. Moguillansky *et al.*, "Quantification of plaque neovascularization using contrast ultrasound: a histologic validation," *Eur. Heart J.*, vol. 32, no. 5, pp. 646–653, Mar. 2011.
- [139] T.-G. Kwon, L. O. Lerman, and A. Lerman, "The Vasa Vasorum in Atherosclerosis," *J. Am. Coll. Cardiol.*, vol. 65, no. 23, 2015.
- [140] A. Portanova, N. Hakakian, D. J. Mikulis, R. Virmani, W. M. A. Abdalla, and B. A. Wasserman, "Intracranial Vasa Vasorum: Insights and Implications for Imaging," *Radiology*, vol. 267, no. 3, pp. 667–679, Jun. 2013.
- [141] F. D. Kolodgie *et al.*, "Intraplaque Hemorrhage and Progression of Coronary Atheroma," *N. Engl. J. Med.*, vol. 349, no. 24, pp. 2316–2325, Dec. 2003.
- [142] J. Xu, X. Lu, and G.-P. Shi, "Vasa vasorum in atherosclerosis and clinical significance.," *Int. J. Mol. Sci.*, vol. 16, no. 5, pp. 11574–608, May 2015.
- [143] R. Moritz, D. R. Eaker, A. C. Langheinrich, S. M. Jorgensen, R. M. Bohle, and E. L. Ritman, "Quantification of vasa vasorum density in multi-slice computed tomographic coronary angiograms: role of computed tomographic image voxel size.," *J. Comput. Assist. Tomogr.*, vol. 34, no. 2, pp. 273–8, 2010.
- [144] M. V. Arcidiacono *et al.*, "Left carotid adventitial vasa vasorum signal correlates directly with age and with left carotid intima-media thickness in individuals without atheromatous risk factors," *Cardiovasc. Ultrasound*, vol. 13, no. 1, p. 20, 2015.
- [145] D. Staub *et al.*, "Contrast-Enhanced Ultrasound Imaging of the Vasa Vasorum," *JACC Cardiovasc. Imaging*, vol. 3, no. 7, pp. 761–771, Jul. 2010.
- [146] X. You *et al.*, "Relationship between enhanced intensity of contrast enhanced ultrasound and microvessel density of aortic atherosclerotic plaque in rabbit model.," *PLoS One*, vol. 9, no. 4, p. e92445, 2014.
- [147] M. J. Rust, M. Bates, and X. Zhuang, "Sub-diffraction-limit imaging by stochastic optical reconstruction microscopy (STORM)," *Nat. Methods*, vol. 3, no. 10, pp. 793–796, Oct. 2006.

- [148] F. Viñals, P. Poblete, and A. Giuliano, "Spatio-temporal image correlation (STIC): a new tool for the prenatal screening of congenital heart defects," *Ultrasound Obstet. Gynecol.*, vol. 22, no. 4, pp. 388–394, Oct. 2003.
- [149] Y. M. Yoo, R. Managuli, Y. Kim, and et al., "Adaptive clutter filtering for ultrasound color flow imaging," *Ultrasound Med. Biol.*, vol. 29, no. 9, pp. 1311–20, Sep. 2003.
- [150] J. Yu, W. Lee, T.-K. Song, and Y. M. Yoo, "Evaluation of flow estimation methods for 3D color Doppler imaging," in *Proceedings - IEEE Ultrasonics Symposium*, 2010.
- [151] W. H. Richardson, "Bayesian-Based Iterative Method of Image Restoration*," *J. Opt. Soc. Am.*, vol. 62, no. 1, p. 55, Jan. 1972.
- [152] L. B. Lucy, "An iterative technique for the rectification of observed distributions," *Astron. J.*, vol. 79, p. 745, Jun. 1974.
- [153] D. S. C. Biggs and M. Andrews, "Acceleration of iterative image restoration algorithms," *Appl. Opt.*, vol. 36, no. 8, p. 1766, Mar. 1997.
- [154] C. A. Schneider, W. S. Rasband, and K. W. Eliceiri, "NIH Image to ImageJ: 25 years of image analysis," *Nat. Methods*, vol. 9, no. 7, pp. 671–675, Jun. 2012.
- [155] T. T. Rissanen *et al.*, "High-Resolution Ultrasound Perfusion Imaging of Therapeutic Angiogenesis," *JACC Cardiovasc. Imaging*, vol. 1, no. 1, pp. 83–91, Jan. 2008.
- [156] S. C. Lee *et al.*, "Temporal Characterization of the Functional Density of the Vasa Vasorum by Contrast-Enhanced Ultrasonography Maximum Intensity Projection Imaging," *JACC Cardiovasc. Imaging*, vol. 3, no. 12, pp. 1265–1272, 2010.
- [157] B. Cox and P. Beard, "Imaging techniques: Super-resolution ultrasound," *Nature*, vol. 527, no. 7579, pp. 451–452, 2015.
- [158] L. Zhao *et al.*, "Feasibility Study on Prenatal Cardiac Screening Using Four-Dimensional Ultrasound with Spatiotemporal Image Correlation: A Multicenter Study," *PLoS One*, vol. 11, no. 6, p. e0157477, Jun. 2016.
- [159] M. Gössl, N. M. Malyar, M. Rosol, P. E. Beighley, and E. L. Ritman, "Impact of coronary vasa vasorum functional structure on coronary vessel wall perfusion distribution," *Am. J. Physiol. - Hear. Circ. Physiol.*, vol. 285, no. 5, pp. H2019–H2026, Nov. 2003.
- [160] A. C. Langheinrich *et al.*, "Correlation of vasa vasorum neovascularization and plaque progression in aortas of apolipoprotein E(-/-)/low-density lipoprotein(-/-) double knockout mice," *Arterioscler. Thromb. Vasc. Biol.*, vol. 26, no. 2, pp. 347–52, Feb. 2006.